STATIONARY AND NON-STATIONARY CASCADED INTERACTIONS IN QUADRATIC NONLINEAR OPTICAL MEDIA: THEORY AND APPLICATIONS

A Dissertation

Presented to the Faculty of the Graduate School

of Cornell University

in Partial Fulfillment of the Requirements for the Degree of

Doctor of Philosophy

by

Kale Beckwitt

August 2004

STATIONARY AND NON-STATIONARY CASCADED INTERACTIONS IN QUADRATIC NONLINEAR OPTICAL MEDIA: THEORY AND APPLICATIONS

Kale Beckwitt, Ph.D.

Cornell University 2004

This thesis presents experimental and theoretical investigations of processes involving the propagation of short optical pulses in second order nonlinear materials. Since pulse propagation in these materials involves the nonlinear coupling of fields at different frequencies, the dynamics are rich, supporting a wide variety of nonlinear processes.

In the limit that an effective Kerr nonlinearity is produced, we demonstrate compensation for cubic nonlinearities in space and time with negative Kerr-like quadratic phase shifts. Self-focusing and self-phase modulation from Kerr nonlinearities typically limit the energy and beam quality from high power lasers, and their compensation allows for significant improvements in both parameters.

We next present theoretical results on the formation of optical solitons in quadratic media — fields of light that propagate stably (or "breath" periodically) due to a robust balance between linear broadening and nonlinear confinement. We are interested in multidimensional solitons in space and time, with the eventual goal of producing "light-bullets:" fields confined in all transverse dimensions. Spatiotemporal solitons provide a natural system in which to observe new effects related to soliton propagation and interactions, with direct applications to opti-

cal signal transfer and processing. Recent experiments by our group demonstrate quadratic solitons in time and one spatial dimension, but are not extendible to three-dimensions due to the material systems used. We theoretically demonstrate a quadratic system in which light-bullets are possible and point a way to their observation. This is the only currently recognized optical system where stable light-bullets are predicted.

Finally, we present a new type of cascaded interactions: nonlinear *frequency* shifting in the limit in which temporal walkoff between the nonlinearly coupled fields significantly affects their propagation dynamics. Previous applications of cascaded nonlinearities saw temporal walkoff as detrimental and found ways to mitigate its effects. We develop a theoretical model for cascaded interactions with significant walkoff and show that non-instantaneous nonlinear responses are possible, producing controllable nonlinear frequency shifts with strong analogs to Raman-scattering in cubic materials. These frequency shifts are analyzed theoretically and experimentally and their applications from low energy frequency shifting for optical communications to compression of high energy pulses are discussed and demonstrated.

BIOGRAPHICAL SKETCH

Kale Beckwitt was born in Berkeley, California in 1976 to Steven and Yahdi Beckwitt of Nevada City, California. The story of how Kale came to be born in Berkeley rather than Nevada City is complex and shall remain untold. Suffice to say it involves Kale's breech and >5-week early birth and perfectly explains his unofficial middle name: Achilles.

Homeschooled until high school by his parents (both onetime teachers), Kale developed a deep found questioning of the world around him, much to the annoyance of his older brothers Eric and Ben. Following high school Kale attended UC Berkeley where try as he might to remain in his chosen major of Chemistry, he was quickly enthralled by Physics, in which he earned a B.A. with honors in 1998.

Kale then opted for a change in climate and entered the Physics Ph.D. program at Cornell University. Following his first year and the many sleepless nights it entailed, Kale has spent his time in the Wise group fixing lasers and performing nonlinear optics experiments (in decidedly unequal proportion).

In grateful dedication to Steve, Yahdi, Eric, Ben, Kerryann,

and all those who came before.

ACKNOWLEDGEMENTS

As with all things, this work would not have been possible without the efforts of many people. First and foremost, I thank my adviser Frank Wise for his encouragement and patience over the years. The ebb and flow of science is capricious and Frank is wise at recognizing and cultivating the process. I could not have asked for better guidance. I also thank Frank's wife, Judy Kany, for her patience.

Several of the results presented herein are works of collaboration. I am grateful to Boris Malomed for his oversight and guidance and his whirlwind trips and email exchanges. I thank Liejia Qian and Heyuan Zhu for their insights into multi-color dispersive propagation in quadratic materials, and Heyuan for his OPA tweaking expertise. I thank Bill Clark, Edesly Canto-Said, and Larry Walker II of Clark-MXR, Inc. for their collaboration and for giving us access to their laser systems. John Nees, Erik Power, and many others at the University of Michigan Center for Ultrafast Optics worked for several whirlwind days and nights to provide the laser source used in Chapter 7.

My time at Cornell was enhanced by the able guidance of my committee members, past and present: Albert Sievers, Tomas Ariás, Alexandar Gaeta, David Cassel, Sol Gruner, and the late Barbara Cooper.

Without the help and camaraderie of many present and past Wise group members and friends, I would not have gotten this far. Among many others I thank: Xiang Liu, for showing me first hand how science is done and passing on his delight in the process; Sylvia Smolarz, for her confidence, whimsy, and copious candy supply; Jeff Harbold, for many, many hours spent finding and debating our paths in life (and for almost as much time spent verifying units); Ömer Ilday, for our discussions and collaboration on non-stationary cascaded quadratic processes and

discourses on life, and for leaving the lab lights on for me in the morning; Yi-Fan Chen, for his help throughout our work on multi-dimensional solitons and for his conviction and fervor which always increased our physical understanding — in the end; Peer Fischer, for his patience at REGEN tweak after REGEN tweak and his ever sanguine outlook; David Hilton, for teaching me an important lesson in life: however many laser problems you have, there is always someone with more; Jeff Moses, for his help with the high energy pulse compression experiments; and in no particular order Hyungsik Lim, Stephen Clark, Joel Buckley, Byung-Ryool Hyun, Lyuba Kouznetsova, Alexis Wynne, Shian Zhou, and those above, for making the Wise group fun and for their ongoing efforts to debug our computers and network.

At Berkeley I thank my Le Conte Hall reading-room cohorts for many late nights of stress and humor. In particular I thank Kyle McElroy for enduring Physics 221 with me and Prof. Commins for his truly excellent problem sets which confined us to Le Conte until all hours of the morning.

Finally, I thank my wife Kerryann Foley for her love and support. It is no small feat to harmoniously complete simultaneous graduate careers, and she made the process a joy.

The primary support for this work was provided by the National Science Foundation, with additional funding from the National Institutes of Health and the Binational (U.S.-Israel) Science Foundation. Research facilities were provided by the Cornell Center for Materials Research, the Cornell Center for Nanoscale Systems, the Cornell Theory Center, Clark-MXR, Inc., and the University of Michigan Center for Ultrafast Optics.

TABLE OF CONTENTS

LIST OF FIGURES

Chapter 1

Introduction

In recent years, the advent of modelocked lasers producing energetic pulses of light of order ∼100 fs in duration has enabled a host of experiments into the nonlinear behavior of optical materials. These experiments are useful not only as probes of material properties, but as a means of studying nonlinear pulse evolution in these systems, and for the applications these highly nonlinear processes enable.

For light fields of sufficiently high intensity, the induced polarization in any optical medium will have a linear and a nonlinear response to the incident field. This response can be expressed as a series

$$P = \epsilon_0 \left(\chi^{(1)} \cdot E + \chi^{(2)} \cdot E \cdot E + \chi^{(3)} \cdot E \cdot E \cdot E + \cdots \right), \tag{1.1}$$

where the susceptibility $\chi^{(n)}$ describes the n-th order response of the material to the applied field. Looking at the first terms of Eq. (1.1), the linear susceptibility ($\chi^{(1)}$) gives rise to classical optical effects like reflection and absorption, the second-order susceptibility ($\chi^{(2)}$) is responsible for second-harmonic generation and parametric mixing processes, and the third-order susceptibility ($\chi^{(3)}$) gives rise to the optical Kerr effect and Raman-scattering processes, among others.

1.1 The Nonlinear Schrödinger Equation

Starting from Maxwell's equations, the wave equation for a field propagating in a lossless, isotropic nonlinear material with polarization response $\tilde{P} = \tilde{P}^L + \tilde{P}^{NL}$ is

$$\frac{\partial^2 \tilde{E}(z,t)}{\partial z^2} - \frac{1}{c^2}\frac{\partial^2 \tilde{E}(z,t)}{\partial t^2} = \mu_0 \frac{1}{c^2}\frac{\partial^2}{\partial t^2}\left(\tilde{P}^L(z,t) + \tilde{P}^{NL}(z,t)\right). \tag{1.2}$$

When considering the propagation of short pulses in optical media, it is natural (within the slowly varying envelope approximation) to break the field into a complex envelope and a rapidly varying phase (Fig. 1.1) according to

$$E(z,t) = ca(z,t)\exp\left(i\beta_0 z - i\omega_0 t\right), \tag{1.3}$$

where c is a constant, $a(z,t)$ is the slowly varying complex amplitude of the field, and β_0 and ω_0 are its propagation constant and carrier frequency, respectively.

For a material with cubic nonlinear response [such that $P^{NL}(z,t) = \epsilon_0 \chi^{(3)} \cdot E(z,t)\cdot E(z,t)\cdot E(z,t)$] we can derive the Nonlinear Schrödinger Equation (NLSE) [1]

$$\frac{\partial a(z,t)}{\partial z} + \underbrace{i\frac{\beta^{(2)}}{2}\frac{\partial^2 a(z,t)}{\partial t^2}}_{\text{Dispersion}} = \underbrace{in_2\left|a(z,t)\right|^2 a(z,t)}_{\text{Nonlinearity}}, \tag{1.4}$$

which describes the evolution of the complex field envelope in a material with dispersion [due to the frequency dependence of the material's refractive index $n = n(\omega)$] and nonlinearity. Here $\beta^{(2)} = \partial^2 k/\partial\omega^2$ (for $k = \omega n/c$) and $n_2 \sim \mathcal{R}(\chi^{(3)})$ describe the group-velocity dispersion and cubic nonlinearity of the material, respectively.

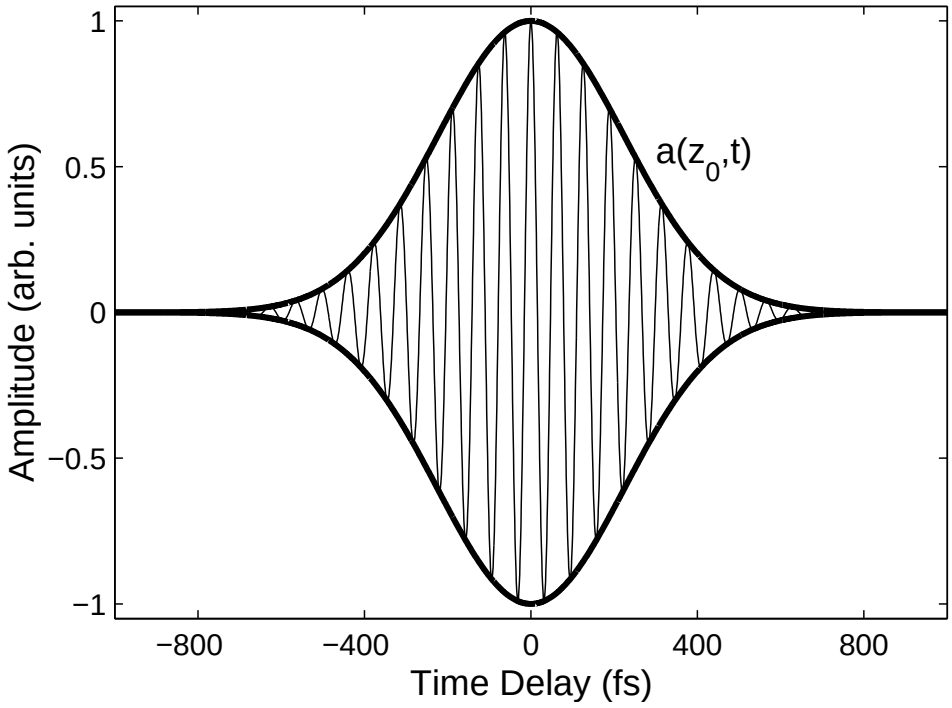

Figure 1.1: Representation of a short optical pulse consisting of a slowly varying complex amplitude $a(z,t)$ and a rapidly varying carrier field $\exp(i\beta_0 z - i\omega_0 t)$.

1.2 Solitonlike pulse shaping and soliton formation

In the NLSE [Eq. (1.4)], group-velocity dispersion and nonlinearity both act to alter the phase of the field envelope $a(z,t)$. As such, phase modulations dominate the generation and propagation of intense ultrashort (picosecond and femtosecond) optical pulses in Kerr media: the physical processes that shape a pulse or govern its propagation act on the phase of the electric field, without altering its amplitude directly. As an example, consider a simple picture of pulse-formation in a modelocked laser. The shaping of pulses in current modelocked lasers is soliton-like: the positive (or self-focusing) nonlinear phase shift induced on a pulse by the nonlinear index (n_2, part of the cubic nonlinearity $\chi^{(3)}$) of the gain medium through the process of self-phase modulation (SPM) implies that the instantaneous frequency varies across the pulse. Stable pulse formation requires that this frequency sweep or chirp is balanced by anomalous group-velocity dispersion (GVD). This is illustrated in Fig. 1.2(a). Intuitively, the nonlinearity shifts low frequencies to the front of the pulse and high frequencies to the rear. Anomalous GVD causes high frequencies to go faster than low frequencies, so the back of the pulse "catches up" with the front. All materials have cubic nonlinearities, and in the absence of (linear or nonlinear) absorption these are almost always positive. Anomalous GVD generally cannot be obtained in materials without absorption.

However, if both processes illustrated in Fig. 1.2 occur in a homogeneous medium, temporal solitons can form — the balance of nonlinearity and dispersion allows the pulse to propagate indefinitely without changing shape. If the signs of the nonlinearity and dispersion are interchanged in the NLSE [Eq. (1.4)], an identical soliton will still form [as in Figure Fig. 1.2(b)]. Therefore, in media with fast negative (self-defocusing) nonlinear refraction, soliton-like pulse shaping

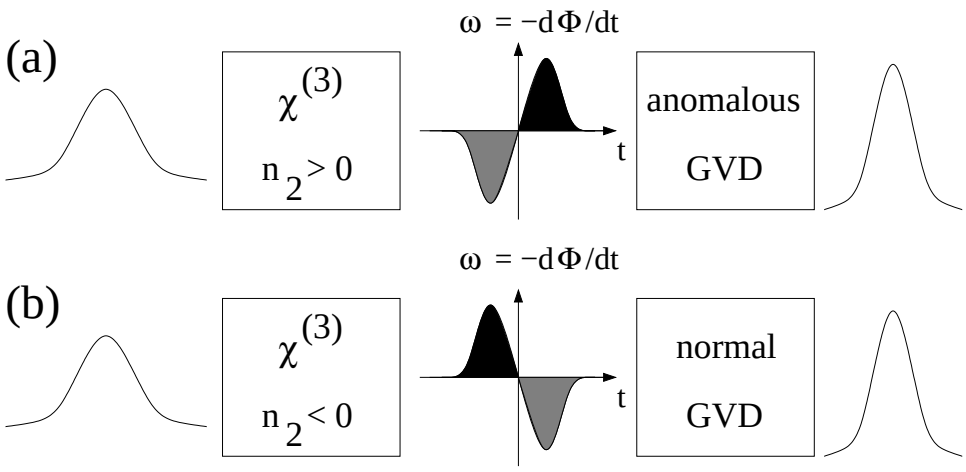

Figure 1.2: Schematic illustration of solitonlike pulse shaping. The nonlinear phase shift impressed on the pulse in a cubic nonlinear medium is balanced by dispersion of the appropriate sign: (a) self-focusing nonlinearity balances anomalous dispersion and (b) self-defocusing nonlinearity balances normal dispersion.

could be implemented with normal GVD.

The transverse spatial variation of a laser beam is governed by processes that are analogous (and mathematically equivalent) to those of Fig. 1.2. The nonlinear index of refraction produces self-focusing of the beam, while diffraction causes the beam to expand. If these processes are precisely balanced, the result is a spatial soliton — a beam that propagates indefinitely without spreading laterally (Fig. 1.3). In contrast to the temporal pulse-shaping described above, it is not sensible to talk about changing the signs of nonlinearity and diffraction; the latter always causes a beam to spread in homogeneous media, so a self-focusing nonlinearity is required to form the soliton. Another issue that arises in the spatial case is the importance of dimensionality. Spatial solitons are stable in one transverse dimension, but unstable in two or more dimensions [2]. In principle the power

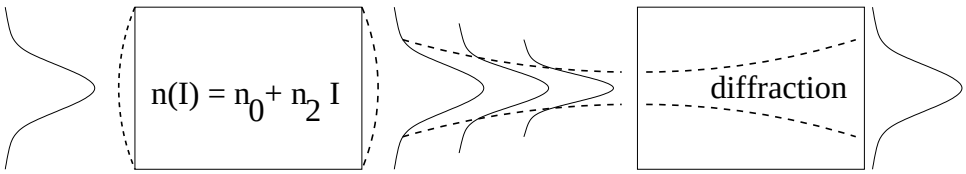

Figure 1.3: Formation of a spatial soliton through the balance of self-focusing nonlinearity and diffraction.

can be chosen so that self-focusing perfectly balances diffraction, but an infinitesimal decrease of the power will cause the beam to expand. On the other hand, an infinitesimal increase from the nominal soliton power causes the beam to focus more, which increases its intensity, which causes more focusing, ad infinitum. This process theoretically ends in "collapse" of the beam to a point (with infinite intensity). In practice other nonlinear processes (and possibly damage to the nonlinear material) occur once the intensity of the collapsing field reaches high enough values.

Ultrafast phase modulations such as those illustrated above are exploited in the following processes, among many others: modelocking of lasers, pulse compression, continuum generation, soliton formation, pulse shaping and cleaning, and optical switching. Furthermore, saturable absorbers are commonly used in pulse shaping and stabilization of modelocked lasers and these are often "effective" or "artificial" saturable absorbers — an intensity-dependent transmittance is produced not by real material absorption, but through nonlinear phase shifts that are converted to transmittance changes in some kind of interferometer or by propagation through an aperture.

Perhaps ironically, the same nonlinearity that is essential to the functions listed above also limits many short-pulse devices and applications. Excessive nonlinear

phase shifts are an ubiquitous problem in the generation of high-energy short pulses. These become significant at the picojoule level in fiber lasers and amplifiers, and at the microjoule or millijoule level in typical bulk devices. In the spatial domain these phase shifts are manifested as self-focusing and instabilities, which adversely affect the beam profile. In the temporal domain uncontrolled nonlinear phase shifts lead to excessive spectral bandwidth and phase distortions, both of which reduce pulse quality or even destroy the pulse.

1.3 Cascaded processes in quadratic nonlinear optical media

Recently, there has been a resurgence of interest in the effective cubic (Kerr) nonlinearity produced by the cascading of phase-mismatched second-harmonic generation processes in quadratic nonlinear media [3]. Since these nonlinearities originate in the coupled interaction of two fields at different frequencies, the underlying multicolor dynamics can be leveraged to control their properties in a way not possible with true third order optical nonlinearities.

Starting from Maxwell's equations and using the slowly varying envelope approximation, the equations that govern the z-propagation of the fundamental-frequency (FF) and second-harmonic (SH) field amplitudes (A_1 and A_2, respectively) in a medium with quadratic nonlinearity (and ignoring transverse effects and processes pertinent to short pulse propagation) are [4]

$$\frac{\partial A_1}{\partial z} = iA_1^* A_2 e^{i\Delta k(Z_I z)}, \tag{1.5}$$

$$\frac{\partial A_2}{\partial z} = iA_1A_1e^{-i\Delta k(Z_I z)}, \tag{1.6}$$

where A_1 and A_2 are normalized in units of the peak value of the initial fundamental field, which is related to the initial peak intensity by $I_0 = nc/(8\pi)\,|A_1(0)|^2$. In Eqs. (1.5) and (1.6) time is normalized by the initial pulse duration τ_0 and is measured in a frame moving at the group velocity of the fundamental field. The propagation length z is normalized to the quadratic interaction length $Z_I = n\lambda_1/\left(\pi\chi^{(2)}A_0\right)$ and $\Delta k = k_{2\omega} - 2k_\omega$ is the phase-mismatch between the FF and SH frequencies. The full coupled wave equations for ultra short pulses appear in Appendix A.

Historically, quadratic optical nonlinearities are usually associated with frequency conversion applications. However, the production of nonlinear phase shifts through the interactions of light beams in quadratic nonlinear media was identified, if not appreciated, in the infancy of nonlinear optics [5]. Isolated studies of the nonlinear phase shifts produced in quadratic processes appeared between 1970 and 1990 [6, 7], and in the last decade there has been a resurgence of interest in this area [8, 9, 3]. Nonlinear phase shifts can be produced in any 3-wave mixing process [for reviews see Refs. [3] and [10]]. The simplest and most pertinent case is phase-mismatched second-harmonic generation (SHG): the fundamental field acquires a nonlinear phase shift in the process of conversion to the SH field and back-conversion to the fundamental [this process is illustrated in Fig. 1.4(a)].

The generation of a nonlinear phase from phase-mismatched SHG can be understood intuitively: due to the frequency dependence of the refractive index [$n = n(\omega)$] in optical media, the SH experiences a different phase-velocity from that of the FF. Consequently light that converts to the SH accumulates a different phase than light that propagates at the FF through the medium. On back

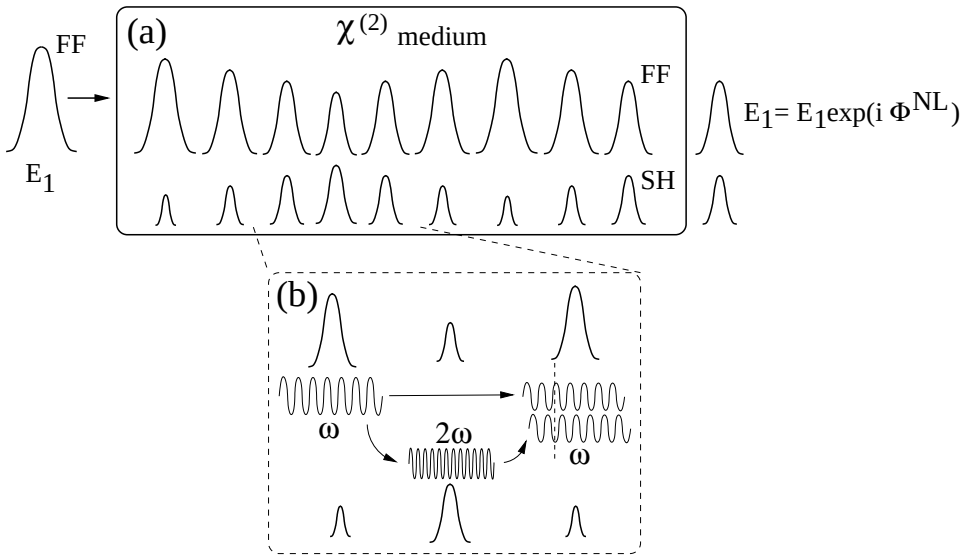

Figure 1.4: Schematic of cascaded quadratic processes under phase-mismatched conditions. (a) depicts the conversion and back-conversion cycle between the FF and SH fields with $|\Delta k| \neq 0$ and (b) shows the details of the phase-velocity mismatch between the fields which causes a nonlinear phase to be imparted on the FF field.

conversion from the SH to the FF, this difference in phase is imparted to the FF field [illustrated in Fig. 1.4(b)]. Since second-harmonic conversion depends on the intensity of the input field, the resulting phase-shift is also nonlinear in nature.

Under conditions of small pump depletion (corresponding to either large phase-mismatch, low input intensity, or both) DeSalvo *et al.* [9] solved Eqs. (1.5) and (1.6) and showed that the nonlinear phase imparted on the FF pulse under these so called "stationary" conditions is Kerr-like with the form

$$\Delta\Phi^{NL} = -\frac{(L/Z_I)^2}{\Delta kL} = n_2^{\text{eff}} I, \tag{1.7}$$

where $n_2^{\text{eff}} \sim (\chi^{(2)})^2/\Delta k$ is the effective Kerr coefficient of the cascaded process and the interaction length Z_I and phase-mismatch Δk are defined as for Eqs. (1.5) and (1.6). The dependence of the nonlinear phase-shift on phase-mismatch is illustrated in Fig. 1.5, with the asymptotic regions of $\Delta\Phi^{NL}$ to which Eq. (1.7) applies indicated by solid curves.

Generally, cascaded phase-shifts have the following properties: (1) they can be large (*i.e.*, $\gtrsim$100 times larger than the n_2's of common $\chi^{(3)}$ materials). This is easily understood: cascaded phase-shifts come about from a lower order term in the expansion for P^{NL} [Eq. (1.1)] with correspondingly larger susceptibilities than for cubic nonlinearities; (2) the magnitude and sign of these phase-shifts are controllable through the phase-mismatch, as depicted in Fig. 1.5; and (3) since cascaded phase-shifts come about through second-harmonic conversion, their magnitude saturates with increasing intensity as the FF to SH conversion process saturates with depletion of the FF.

The sequential or *cascaded* nature of these quadratic processes gives rise to

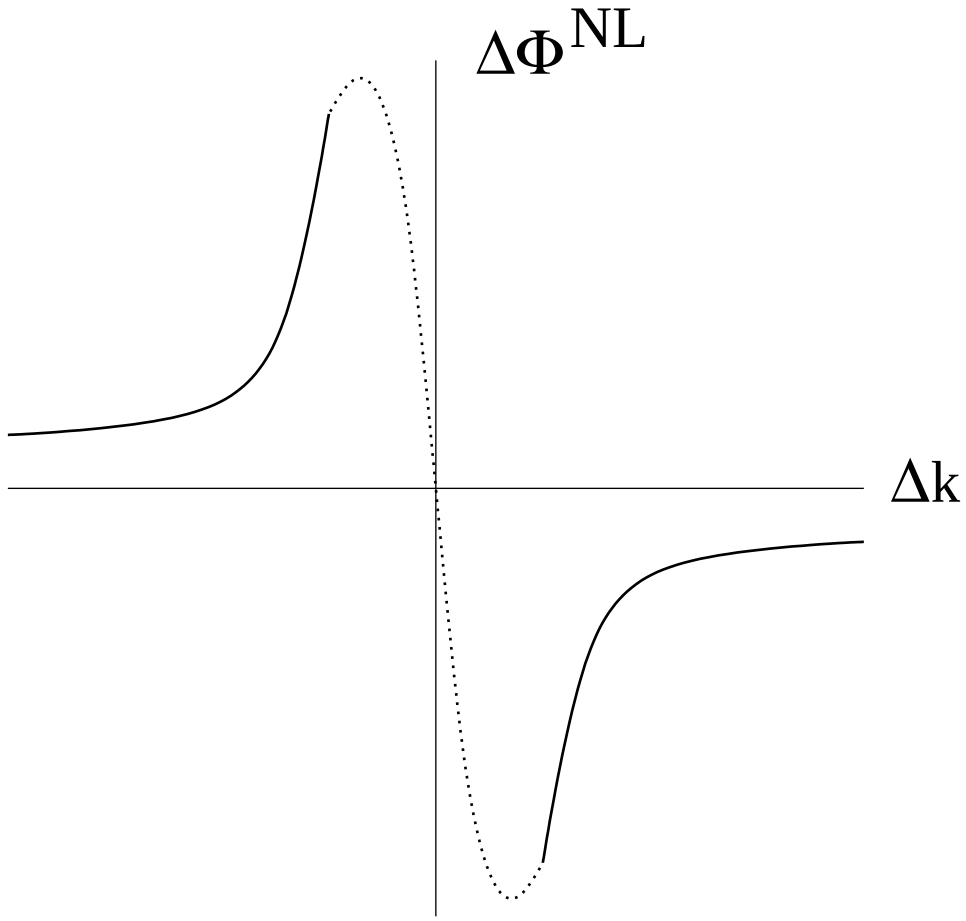

Figure 1.5: Illustration of the nonlinear phase-shift imposed on the FF field as a function of phase-mismatch. Solid curves indication the "stationary" region with dashes showing the rough dependence near phase matching.

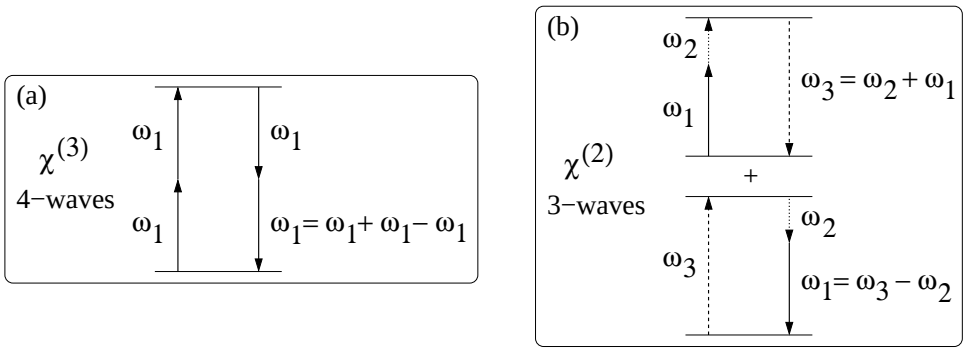

Figure 1.6: Schematic energy level diagram of cubic ($\chi^{(3)}$) (a) versus cascaded quadratic ($\chi^{(2)}$) (b) processes.

their name. A schematic energy level diagram of this processes appears in Fig. 1.6. As we can see, cubic ($\chi^{(3)}$) nonlinearities involve the interactions of four waves, allowing the processes to yield photons at the initial frequency (ω_1) and hence to impart a phase on it. Quadratic ($\chi^{(2)}$) processes involve three waves, requiring two such processes to occur sequentially (*i.e.*, to be *cascaded*) for an equivalent return to ω_1 [Fig. 1.6(b)].

For pulse-shaping applications, the ability to control the sign of the nonlinear phase shift, and specifically the ability to generate negative phase shifts without excessive loss, is of huge significance. Furthermore, cascaded phase shifts can be controlled conveniently, by simply adjusting the orientation or temperature of a nonlinear crystal. In the past decade cascaded nonlinear phase shifts in quadratic media have been used to demonstrate a myriad of applications, including: compensation of Kerr phase shifts in space and time [11]; Kerr-lens modelocking of short pulse lasers [12]; observation of spatial, temporal, and spatiotemporal solitons and their instabilities (for review see Refs. [13] and [14]); observation of spatial [15] and spatiotemporal soliton interactions [16]; ordinary [17] and solitonlike [18] pulse

compression; and many others [19].

Saturation of the nonlinear phase shift is undesirable in most pulse-shaping applications because it distorts the temporal variation of the phase shift (and frequency chirp) from the shape produced in cubic nonlinear media (where the phase shift is proportional to intensity for all intensities). However, saturation is crucial to stabilize multi-dimensional solitons against the collapse that occurs in true cubic nonlinear media.

Nonlinear phase shifts are associated with nonlinear indices of refraction, and below saturation it can be useful to define an effective nonlinear index for the cascade process [*i.e.*, n_2^{eff} in Eq. (1.7)]. Continuing the analogy to cubic nonlinear processes, the residual second-harmonic light that is generated in the phase-mismatched process can be likened to 2-photon absorption. The figure of merit for applications based on nonlinear phase shifts is proportional to the nonlinear phase shift per unit nonlinear absorption (nonlinear conversion in this case). Thus, the figure of merit for the cascade process tends to increase with increasing phase mismatch, simply because the residual conversion decreases faster than the magnitude of the nonlinear phase shift.

1.4 Group-velocity mismatch and stationary cascaded quadratic processes

Although the phase-shift from cascaded quadratic processes offers phase-shift magnitude and control not possible with Kerr nonlinearities, prospects for exploiting cascaded phase shifts for short-pulse generation initially were considered poor: Due to frequency dependence of the refractive index in nonlinear media, the fun-

damental and second-harmonic pulses inevitably have different group velocities and consequently they move away from each other in time with propagation. This reduces and distorts the nonlinear phase shift.

Historically, the deleterious effects of group-velocity mismatch were recognized, and unique and complicated material structures were constructed to combat them [20, 21, 22]. However, there is another way [19]: in phase-mismatched SHG, the phase-mismatch between the FF and SH fields has two effects. First, increasing $|\Delta k|$ causes a reduction in the maximum energy conversion from the fundamental to the SH. However, increasing $|\Delta k|$ also acts to increase the frequency of the FF-SH conversion and back-conversion cycle. These dependencies are illustrated in Fig. 1.7.

This increase in conversion cycle frequency with increasing phase-mismatch presents a way to mitigate the effects of phase-distortion from GVM. If the magnitude of the phase-mismatch is increased to the point that the FF-SH conversion cycle occurs *before* GVM causes the field to separate temporally, the phase distortion will be lessened or eliminated. This can be though of as follows: each conversion and back-conversion cycle of the FF and SH fields defines an effective interaction length over which GVM acts to separate them. Increasing the magnitude of the phase-mismatch between the fields reduces the cycle length and hence the effective interaction length for GVM.

More explicitly we require that the cycle length ($L_c = 2\pi/\Delta k$) be at most half the characteristic length over which GVM separates the fields ($L_{\mathrm{GVM}} = \tau_0/\mathrm{GVM}$) to effectively mitigate its effects, or

$$|\Delta k| \gtrsim \frac{4\pi}{L_{\mathrm{GVM}}} = 4\pi \frac{\mathrm{GVM}}{\tau_0}. \tag{1.8}$$

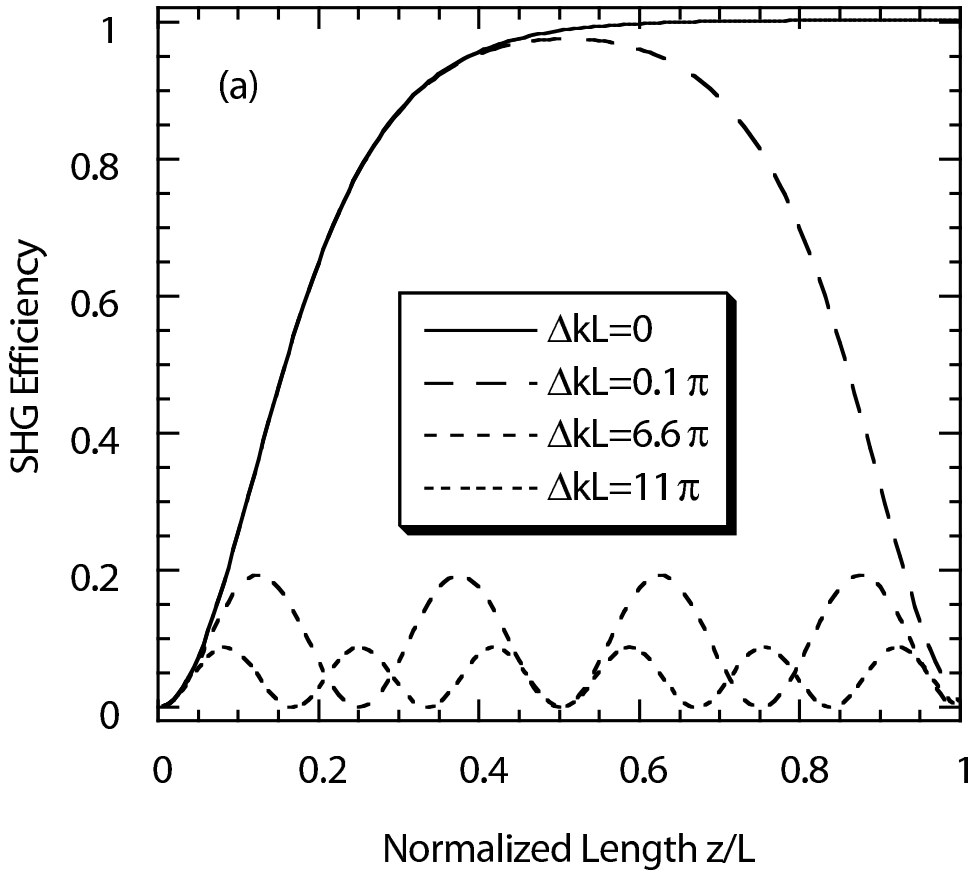

Figure 1.7: Second-harmonic conversion efficiency as a function of propagation distance for various values of ΔkL.

In this way, an effective Kerr phase is regained from the cascaded quadratic processes, even in the presence of strong GVM. Of course, this reduction in phase distortion comes at a price: as is apparent in Fig. 1.7, increasing the phase-mismatch reduces the maximum conversion efficiency to the SH; hence, increased phase-shift quality is obtained at the expense of magnitude. Thus, the utility of the cascade phase shift for a given application ultimately depends on the nonlinearity of available and appropriate SHG crystals. An elegant theoretical way to understand the improvement in phase-shift quality is the following: In the limit of large phase mismatch, the equation for the fundamental field approaches the ordinary nonlinear Schrödinger equation that governs pulse propagation in cubic nonlinear media [Eq. (1.4)] [23]. Thus, in that limit the effective nonlinearity is just a Kerr nonlinearity. A similar argument can be made in the frequency domain. The phase-matching bandwidth (which is directly proportional to L_{GVM}) is a crucial parameter in SHG, and one may wonder about the acceptance bandwidth for the cascade process. In the phase-mismatched case the acceptance bandwidth is proportional to the product $(\Delta k \times L_{\mathrm{GVM}})$. If the criterion for high-quality phase shifts is satisfied, the entire spectrum of the input pulse will be acceptably phase-mismatched.

Fig. 1.8 shows simulations of the the distortion of the nonlinear phase shift owing to saturation or to the group-velocity mismatch (GVM) between the harmonics and the recovery of a Kerr-like nonlinear phase with increased phase-mismatch amplitude [19]. In Fig. 1.8, the dashed curves show the frequency chirp resulting from a negative Kerr nonlinearity for comparison.

Fig. 1.8(a) shows the distortion that arises from saturation, while Fig. 1.8(c)

and 1.8(e) show the deleterious effects of increasing GVM. In Fig. 1.8(e), for example, the pulses separate by ∼4 times the input pulse duration, and the distortion of the cascade frequency chirp is extreme. In all three cases the distortion of the phase shift would preclude the production of high-quality pulses, perhaps even the production of any stable pulses. The conditions of Fig. 1.8(e) correspond to 120-fs pulses at 800 nm wavelength, propagating through a barium metaborate (BBO) crystal only 2.4 mm long. This situation is representative of the problems that arise in quadratic nonlinear optics with femtosecond pulses.

According to the criterion of Eq. (1.8), for $L = L_{\mathrm{GVM}}$ we require $\Delta kL > 4\pi$ for recovery of a clean nonlinear phase. The high-quality frequency chirp produced with $\Delta kL = 11\pi$ (which satisfies the criterion with ample margin) is shown in Fig. 1.8(d). For $L = 4L_{\mathrm{GVM}}$ we require $\Delta kL > 16\pi$. In this case $\Delta kL = 11\pi$ is not adequate, and the frequency chirp is still distorted [Fig. 1.8(f)]. However, it is much better than that produced with $\Delta kL = 2\pi$ [Fig. 1.8(c)]. Figs. 1.8(a) and 1.8(b) show that increased phase mismatch naturally also reduces the distortion that arises from saturation.

1.5 Group-velocity mismatch and non-stationary cascaded quadratic processes

To date all demonstrated applications of cascaded processes occur in the so-called "stationary-limit" where an effective (but controllable) Kerr-like nonlinearity is produced. As discussed, this is typically accomplished by increasing the phase-mismatch between the fundamental and second-harmonic fields to the point that the cycle of conversion from fundamental to second-harmonic and back-conversion

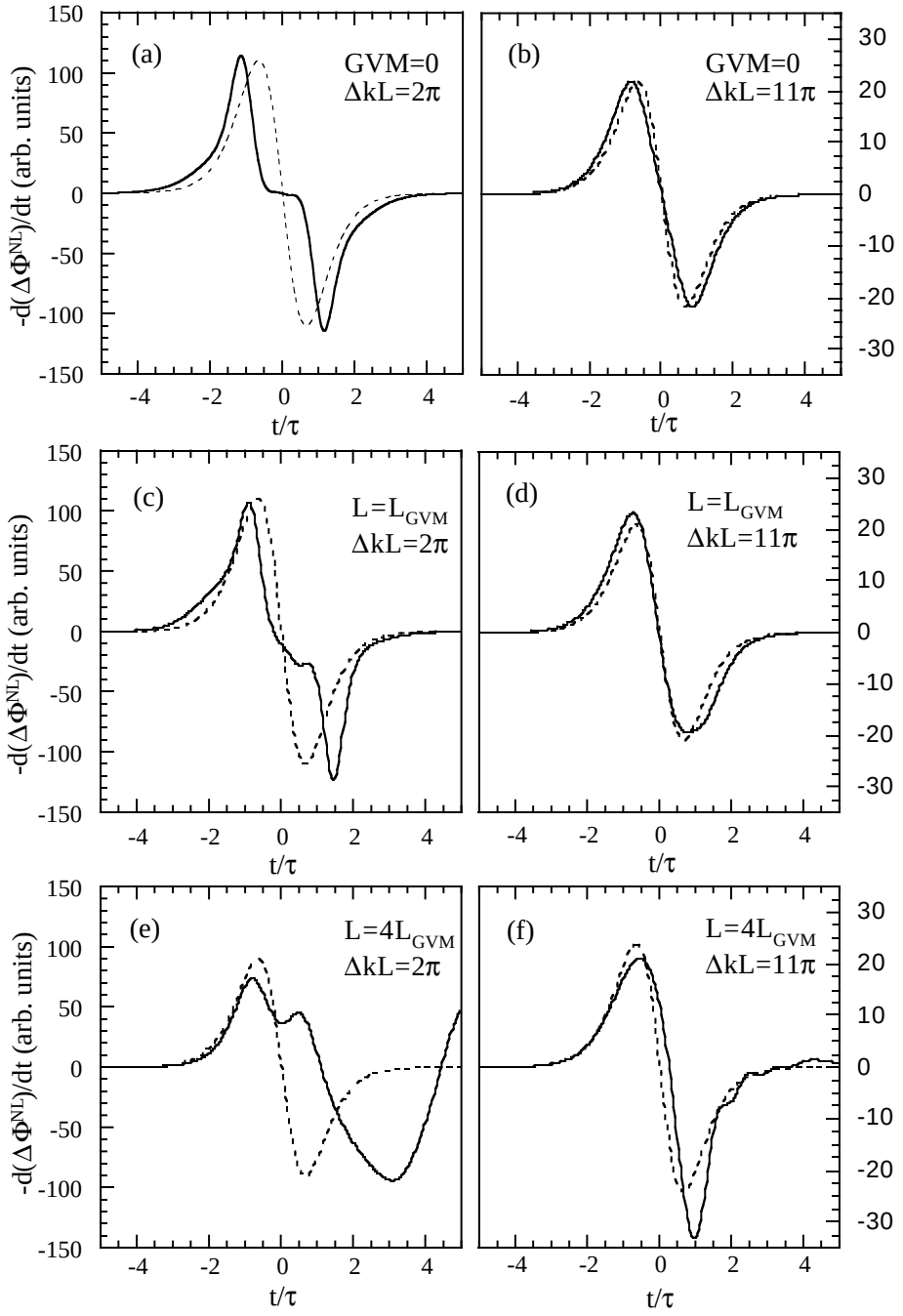

Figure 1.8: Calculated frequency chirp resulting from nonlinear phase shifts of the fundamental pulse. Left (right) column correspond to $\Delta kL = 2\pi$ (11π). Group-velocity mismatch increases from top to bottom, starting from zero. Dashed curves show the frequency chirp from a negative Kerr nonlinearity.

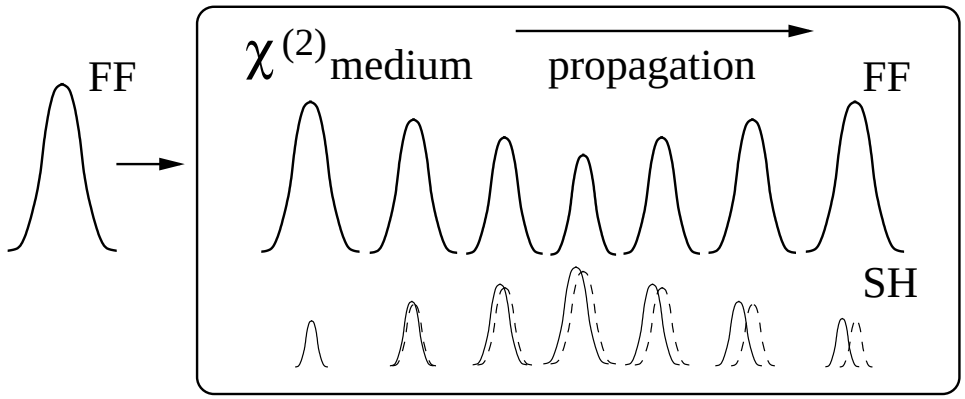

Figure 1.9: Illustration of the phase-mismatched cascaded quadratic process with group-velocity mismatch. Solid (dashed) lines are for the case of nonzero (zero) group-velocity mismatch, which causes the back-converted SH field to lag or lead the FF.

from second-harmonic to fundamental occurs before the fields separate temporally due to group-velocity mismatch between them [19]. This method produces a Kerr-like phase-shift despite the presence of material group-velocity mismatch, but at the cost of reduced nonlinear coupling and phase [19, 23].

However, it is useful to consider what happens in the case that the effects of GVM are *not* lessened by increasing the phase-mismatch beyond the stationary region defined by Eq. (1.8). Then GVM causes the SH field to walk away from the FF with propagation, which creates a temporal displacement between the fields as depicted in Fig. 1.9.

As is known, GVM causes the resulting nonlinear phase-shift to be distorted from a Kerr-like shape [as demonstrated in Fig. 1.8]. However, it also causes the nonlinear phase to be temporally displaced from the FF pulse: *i.e.*, cascaded processes can yield a *non-instantaneous* nonlinear phase, $\Delta\Phi^{\mathrm{NL}}(t) \sim I(t \pm \tau)$, where the phase is either temporally delayed or advanced with respect to the FF

by an amount τ which depends on the details of the cascaded process. However, a non-instantaneous nonlinear phase in the temporal domain generates a shift in the center frequency of the pulse spectrally. This is well know from cubic Raman-scattering processes, where Stokes-shifts correspond to delayed nonlinear processes and redshifts of the pulse spectrum; in analogy, non-stationary cascaded processes are capable of generating nonlinear frequency shifts, but with the usual advantages of cascaded quadratic processes: increased magnitude with respect to their cubic counterparts, and tunability of the sign and magnitude of the resulting nonlinearity. This thesis develops the theory of these nonlinear frequency shifts from non-stationary cascaded quadratic processes and a number of techniques and applications based on their unique advantages are discussed and demonstrated experimentally.

1.6 Organization of the thesis

The remaining sections of this thesis are organized as follows: Chapter 2 demonstrates direct compensation of nonlinear phase shifts from Kerr nonlinearities with negative Kerr-like shifts from cascaded quadratic processes [11]. Phase compensation has been demonstrated previously, but with real negative Kerr media, which are susceptible to material damage with high energy pulses and typically involve significant loss in the form of one- and two-photon absorption. We show numerically and experimentally that cascaded phase shifts provide a near ideal method to compensate for the effects of self-focusing (both whole-beam and small-scale) from Kerr nonlinearities in the spatial domain, and undo spectral broadening from self-phase modulation (B integral) temporally. The applications of this compensation process to increased energy and improved beam quality from high power lasers are

discussed.

Spatiotemporal solitons are of great interest both as a novel manifestation of highly nonlinear dynamics for questions of fundamental science and for the potential technological applications they present: optical transmission and switching at rates of many terahertz [24]. The Kerr-like but saturable nonlinearity provided by cascaded quadratic interactions provides one of the most promising systems for the observation and study of spatiotemporal solitons. However, formation of spatiotemporal solitons in these media requires anomalous group-velocity dispersion which does not occur at wavelengths corresponding to common infrared laser sources. Consequently, observations of temporal and spatiotemporal solitons in quadratic media to date have been achieved using the method of pulse-tilting [25] to externally modify the group-velocity dispersion experienced by the pulse in the nonlinear medium. Pulse-tilting allows for anomalous group-velocity dispersion at common wavelengths in the infrared and following Valiulis *et al.'s* demonstration [26] of quadratic temporal solitons using this technique, our group applied it to demonstrate quadratic soliton formation in time and one transverse spatial dimension [27, 28] (*i.e.*, two-dimensional spatiotemporal solitons), their interactions [16], and transverse instability in three-dimensions [29]. However, pulse-tilting involves angular dispersion from a diffraction grating — spatial spreading of the frequency components of the pulse — which consumes a transverse degree of spatial freedom and prevents soliton confinement along that direction [29].

In Chapter 3 we present theoretical work [30] that identifies a quadratic system where temporal and spatiotemporal solitons may form. By working at wavelengths in the infrared (3-5 μm typically) where available quadratic materials exhibit anomalous group-velocity dispersion at the fundamental wavelength, we show

that these systems can stably support solitons despite the presence of near-zero or even normal group-velocity dispersion at the second-harmonic wavelength. These systems provide a near ideal test bed for the study of temporal and spatiotemporal solitons. Experimentally, these solitons are realizable in quasi-phase-matched quadratic materials like periodically poled lithium niobate [31] and may provide the best current route to the experimental observation of "light-bullets" — multi-dimensional solitons confined in time and all transverse spatial dimensions. Indeed, light-bullets appear to be observable in these systems [32] and potential experiments are discussed.

Observation of solitons without pulse tilt (Chapter 3) requires generation of $\sim$100 fs and near-Fourier transform limited pulses with energy $\gtrsim$1 μJ in the infrared near 4 μm. Experimentally, this is not an easy wavelength region to generate pulses with these exacting parameters. Appendix C presents an overview of how these pulses are generating using optical parametric amplification, and outlines our current progress with these sources.

Since the index of refraction in optical materials depends of frequency, different colors experience different group-velocities. In quadratic materials this means that some finite group-velocity mismatch exists between the fundamental and second-harmonic fields. Previous applications utilizing effective cubic nonlinear phase shifts avoided the effects of this temporal walkoff — but at the cost of reduced magnitude of the effective nonlinearities from cascaded processes [19, 28], or via complicated material structures [20, 21, 22].

In Chapter 4 we develop a new theoretical model for cascaded interactions in the limit where the effects of group-velocity mismatch are strongly felt, and show that this opens the door to a new type of cascaded quadratic interaction: *non-*

instantaneous nonlinear phase-shifts [33]. We analytically show that for small delay or advancement in the temporal response, these shifts are qualitative similar to Raman-scattering processes in cubic materials. In particular, like Raman processes this non-instantaneous nonlinear response gives rise to a shift in the pulse spectrum. Since these spectral shifts come about from cascaded quadratic interactions, they are controllable and nonlinear frequency shifts of controllable magnitude and sign are possible. We experimentally demonstrate these shifts with millijoule pulses from an amplified laser system.

Chapters 5 and 6 discuss two exciting prospects for cascaded frequency shifts: In Chapter 5 we show that these processes can be enhanced and greatly customized by physical engineering of the material nonlinearity in certain classes of quadratic nonlinear materials [34]. In Chapter 6 we demonstrate generation of cascaded frequency shifts with low (picojoule) pulse energies in waveguided structures [35]. In waveguides strong confinement of the light field allows these highly nonlinear interactions with pulse energies directly applicable to fiber lasers and optical communications applications.

Chapter 7 goes in the other direction and demonstrates Raman-soliton like pulse compression based on cascaded frequency shifting processes, but with intense ($\gtrsim$1.3 TW/cm^2) and ultra-short ($\sim$30 fs) pulses [36]. The ability to generate Raman-like nonlinearities with negative (self-defocusing) phase-shifts prevents material damage and enables applications with these extreme field parameters.

In Chapter 8 several potential applications of frequency shifts from cascaded processes techniques are discussed.

In all cases, physical understanding of the nonlinear optical processes studied and efficient experimental design relies on fast and accurate simulations of these

problems. To this end a set of numerical simulations have been developed with enable numerical solutions of these pulse propagation problems. The coupled non-linear equations governing the system studied appear in Appendix A, and the physical and computational design of these simulations appear in Appendix B. Single and parallel processor versions of the pulse propagation code exist, along with associated Matlab visualization routines.

BIBLIOGRAPHY

[1] G. P. Agrawal. *Nonlinear Fiber Optics* (Academic Press: San Diego, 1995).

[2] V. E. Zakharov and A. M. Rubenchik, Zh. Éksp. Teor. Fiz. **65**, 997 (1973) [Sov. Phys. JETP **38**, 494 (1974)].

[3] G. I. Stegeman, R. Schiek, L. Torner, W. Torruellas, Y. Baek, D. Baboiu, Z. Wang, E. Van Stryland, D. J. Hagan, and G. Assanto, "Cascading: A Promising Approach to Nonlinear Optical Phenomena," in *Novel Optical Materials and Applications*, I.C. Khoo, F. Simoni, and C. Umeton ed. (John Wiley & Sons, New York, 1997), Ch. 2, pp. 49-76.

[4] A. A. Kanashov and A. M. Rubenchik, Physica D **4**, 122 (1981).

[5] J. A. Armstrong, N. Bloembergen, J. Ducuing, and P. S. Pershan, Phys. Rev. **127**, 1918 (1962).

[6] J.-M. R. Thomas and J.-P. E. Taran, Opt. Commun. **4**, 329 (1972)

[7] N. R. Belashenkov, S. V. Gagarskii, and M. V. Inochkin, Opt. Spectrosc. **66**, 806 (1989).

[8] H. J. Bakker, P. C. M. Planken, L. Kuipers, and A. Lagendijk, Phy. Rev. A **42**, 4085 (1990)

[9] R. DeSalvo, D. J. Hagan, M. Shiek-Bahae, G. Stegeman, E. W. Van Stryland, and H. Vanherzeele, Opt. Lett. **17**, 28 (1992).

[10] L. Torner and G. Stegeman, Opt. Photon. News, p. 36, June 2001.

[11] K. Beckwitt, F. W. Wise, L. Qian, L. A. Walker II, and E. Canto-Said, Opt. Lett. **26**, 1696 (2001).

[12] L. J. Qian, X. Liu, and F. W. Wise, Opt. Lett. **24**, 166 (1999).

[13] C. Etrich, F. Lederer, B.A. Malomed, T. Peschel, and U. Peschel, Progr. Opt. **41**, 483 (2000).

[14] A.V. Buryak, P. Di Trapani, D.V. Skryabin and S. Trillo, Physics Reports **370**, 63 (2002).

[15] C. Simos, V. Couderc, A. Barthélémy, and A. V. Buryak, J. Opt. Soc. Am. B **20**, 2133 (2003).

[16] X. Liu, K. Beckwitt, and F. W. Wise, Phys. Rev. E **61**, R4722 (2000).

[17] X. Liu, L. Qian, and F. W. Wise, Opt. Lett. **24**, 1777 (1999).

[18] S. Ashihara, J. Nishina, T. Shimura, K. Kuroda, J. Opt. Soc. Am. B **19**, 2505 (2002).

[19] F. Wise, L. Qian, and X. Liu, J. Nonlinear Opt. Phys. & Mat. **11**, 317 (2002).

[20] K. A. Stankov, V. P. Tzolov, and M. G. Mirkov, Appl. Phys. B **54**, 303 (1992).

[21] G. Cerullo, V. Magni, A. Monguzzi, Opt. Lett. **20**, 1785 (1995).

[22] R. J. Gehr, M. W. Kimmel, A. V. Smith, Opt. Lett. **23**, 1298 (1998).

[23] C. R. Menyuk, R. Schiek, and L. Torner, J. Opt. Soc. Am. B **11**, 2434 (1994).

[24] R. McLeod, K. Wagner, and S. Blair, Phys. Rev. A **52**. 3254 (1995).

[25] O. E. Martinez, IEEE J. Quantum Electron. **25**, 2464 (1989).

[26] G. Valiulis, A. Dubietis, R. Danielius, D. Caironi, A. Visconti, and P. Di Trapani, J. Opt. Soc. Am. B **16**, 722 (1999).

[27] X. Liu, L. J. Qian, and F. W. Wise, Phys. Rev. Lett. **82**, 4631 (1999).

[28] X. Liu, K. Beckwitt, and F. W. Wise, Phys. Rev. E **22**, 1328 (2000).

[29] X. Liu, K. Beckwitt, and F. W. Wise, Phys. Rev. Lett. **85**, 1871 (2000).

[30] K. Beckwitt, Y.-F. Chen, F. W. Wise, and B. A. Malomed, Phys. Rev. E **68**, 057601 (2003).

[31] M. M. Fejer, G. A. Magel, D. H. Jundt, and R. L. Byer, IEEE J. Quantum Electron. **28**, 2631 (1992).

[32] I. N. Towers, B. A. Malomed, and F. W. Wise, Phys. Rev. Lett. **90** 123902 (2003).

[33] F. Ö. Ilday, K. Beckwitt, Y.-F. Chen, H. Lim, F. W. Wise, J. Opt. Soc. Am. B **21**, 376 (2004).

[34] K. Beckwitt, F. Ö. Ilday, and F. W. Wise, Opt. Lett. **29**, 763 (2004).

[35] K. Beckwitt, F. Ö. Ilday, F. W. Wise, W. Grundkötter, and W. Sohler, Opt. Lett. (submitted for publication).

[36] K. Beckwitt, J. A. Moses, F. Ö. Ilday, F. W. Wise, J. Nees, E. Power, K. H. Hong, B. Hou, and G. Mourou, "Cascade-Raman soliton compression with 30-fs, terawatt pulses," presented at the conference on Nonlinear Guided Waves and Their Applications, Toronto, Canada, 28-31 Mar. 2004.

Chapter 2

Compensation of self-focusing using the cascade quadratic nonlinearity[1]

We demonstrate theoretically and experimentally compensation for positive Kerr phase shifts with negative phases generated by cascade quadratic processes. Experiments show correction of small-scale self-focusing and whole-beam self-focusing in the spatial domain and self-phase modulation in the temporal domain.

2.1 Introduction

When an intense beam propagates through a third-order nonlinear medium, its intensity profile generates a corresponding phase profile through the intensity-dependent refractive index: $n(I) = n_0 + n_2 I$. The phase shift resulting from the electronic Kerr nonlinearity underlies a number of physical processes, including whole-beam self-focusing (WBSF) and small-scale self-focusing (SSSF) in space [2], and self-phase modulation (SPM) in time [3]. Since self-focusing limits the peak power attainable by high energy lasers and amplifiers, and SPM underlies the need to use pulse stretching in regenerative amplifiers (RAs) [4], a means of compensating for these effects is desirable.

Self-focusing and SPM in materials with $n_2 > 0$ arise from nonlinear phase shifts, $\Phi^{NL}_{Kerr}(x,y) = (2\pi/\lambda)\int n_2(z) I(x,y,z) dz$, referred to as the B integral. One can utilize nonlinear phase shifts, $\Phi^{NL}_{comp} < 0$, from a material with real or effective $n_2 < 0$ for compensation; i.e., $\Phi^{NL}_{Kerr} + \Phi^{NL}_{comp} = 0$. One way to generate such a com-

[1]The results presented in this chapter have been published in Ref. [1].

pensating phase is through the negative nonlinear refractive index that is present in semiconductors. GaAs wafers [with $n_2 \sim -1000\, n_2$(fused silica) for wavelengths just longer than the absorption edge] were used by Roth *et al.* [5] to suppress the effects of self-focusing in Nd:glass rods and by Konoplev and Meyerhofer [6] to cancel the B integral in a chirped-pulse amplifier (CPA) system. However, this approach has the disadvantages that are inherent in semiconductors: high loss owing to two-photon absorption and a relatively low damage threshold. Additionally, the nonlinear index (n_2) of these materials is fixed, making phase cancellation difficult: To tune the value of the compensating phase at a given intensity, one must change the semiconductor wafer thickness itself.

Recently, the phase shifts generated by cascading $\chi^{(2)}$ processes in quadratic nonlinear media garnered attention because they can be large in magnitude, can have a controllable sign, and are proportional to intensity in the limit of large phase mismatch between the fundamental-harmonic (FH) and second-harmonic (SH) waves [7]:

$$\Phi^{NL} \approx -\frac{\Gamma^2 L^2}{\Delta k L}, \tag{2.1}$$

where $\Gamma = \omega d_{eff}|E_0|/c\sqrt{n_{2\omega} n_\omega}$, $\Delta k = k_{2\omega} - 2k_\omega$ is the phase mismatch, and L is the crystal length. Equ. (2.1) holds when $|\Delta k L|$ is large enough that the effects of group-velocity mismatch (GVM) between the FH and the SH can be neglected [8]. Negative cascade phase shifts were recently used for pulse compression [9] and to compensate for the B integral in a fiber amplifier [10].

In this Letter we show by numerical simulation and experiment that negative phase shifts from cascade quadratic processes can effectively compensate the ef-

fects of self-focusing. We demonstrate compensation of both SSSF and WBSF in the propagation of femtosecond pulses in bulk fused silica. In addition, we show cancellation of the B integral from a picosecond Ti:sapphire amplifier with pulse energies of ∼6 orders of magnitude greater than in the work of Alam *et al.* [10].

2.2 Numerical results

As in Ref. [8] we model the system with the coupled wave equations for the FH and the SH fields in a medium with $\chi^{(2)}$ and $\chi^{(3)}$ nonlinearity. We solve the propagation equations numerically, using a symmetric split-step beam propagation method [8]. We considered both precompensation and postcompensation schemes and for experimental convenience chose precompensation (both worked comparably in simulation). Figure 2.1 shows the results of numerical simulations performed under conditions typical of a millijoule-pulse energy RA. In the absence of compensation, a beam with transverse intensity modulation [Fig. 2.1(a)] traverses a piece of $\chi^{(3)}$ material that produces $\Phi^{NL} \sim \pi$ and increases the spatial intensity modulation [Fig. 2.1(b)]. With compensation, the intensity profile is smoothed compared to the uncompensated case [Fig. 2.1(c)]. We find optimal compensation with $\Delta kL \sim 400\pi$ using material parameters for barium metaborate (BBO), which agrees with a calculation based on Equ. (2.1). In contrast, Fig. 2.1(d)] shows the intensity profile resulting from overcompensation for the Kerr phase with $\Delta kL \sim 175\pi$.

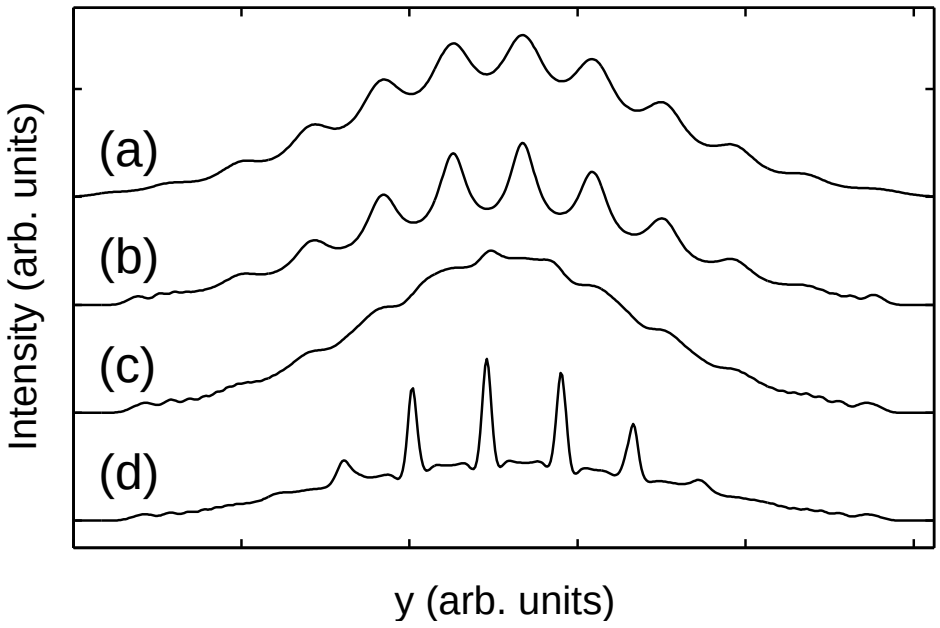

Figure 2.1: Simulated transverse intensity profile (a) at input with seeded periodic intensity modulation, (b) after propagation through 6 cm of fused silica, (c) with optimal compensation ($\Phi_{net}^{NL} \approx 0$), and (d) overcompensating Kerr phase ($\Phi_{net}^{NL} < 0$).

2.3 Experimental results

Experimentally, we observe self-focusing after propagating the output of a Ti:sapphire RA ($\lambda_0 = 800$ nm, $\tau_{\rm FWHM} = 150$ fs, E ≈ 600 μJ/pulse) through 6 cm of fused silica. Using a 2:1 telescope we down-collimate the RA output prior to the fused silica to produce a beam with full-width at half-maximum (FWHM) dimensions 2.7 mm by 1.6 mm, which allows intensities up to 70 GW/cm^2.

Fig. 2.2 shows the experimental beam profiles. At low intensity, we observe linear propagation through the fused silica [Fig. 2.2(a)]. At high intensity ($I_0 =$ 23 GW/cm^2, $\Phi^{NL} \approx 1.1\pi$) we observe both WBSF (narrowing of the beam profile) and SSSF (increased modulation depth between the noise peaks and background, shown in Fig. 2.2(b); and cuts though data appear as insets in Figs. 2.3 and 2.4). To compensate self-focusing, a 2.5 cm long BBO crystal cut for type-I second-harmonic generation (SHG) at 800 nm is inserted into the beam path immediately before the fused silica. As a control experiment, we orient the BBO so that we have access to only the Kerr nonlinearity. We measured n_2[BBO] $\approx$ n_2[fused silica], so we expect $\sim$50% more nonlinear phase than for fused silica only. Fig. 2.2(c) shows the expected additional self-focusing. Next, the BBO is oriented to produce negative phase shifts via the cascade nonlinearity. Optimal compensation ($\Phi^{NL}_{net} \approx 0$) is found near $\Delta kL \approx 550\pi$ [Fig. 2.2(e)] which is close to the predicted value (400π) considering the uncertainty in $|\Delta kL|$ ($\sim 75\pi$). Tuning to $\Delta kL \approx 900\pi$ we observe undercompensation of the Kerr phase ($\Phi^{NL}_{net} > 0$) and residual WBSF [Fig. 2.2(f)]. At $\Delta kL \approx 300\pi$, the Kerr phase overcompensates the quadratic phase ($\Phi^{NL}_{net} < 0$), and we see whole-beam self-defocusing [Fig. 2.2(d)]. In both cases as we tune away from optimal compensation, SSSF is apparent. The SSSF filaments observed in Fig. 2.2(d) have dimension $\sim$0.3 mm, close to that predicted

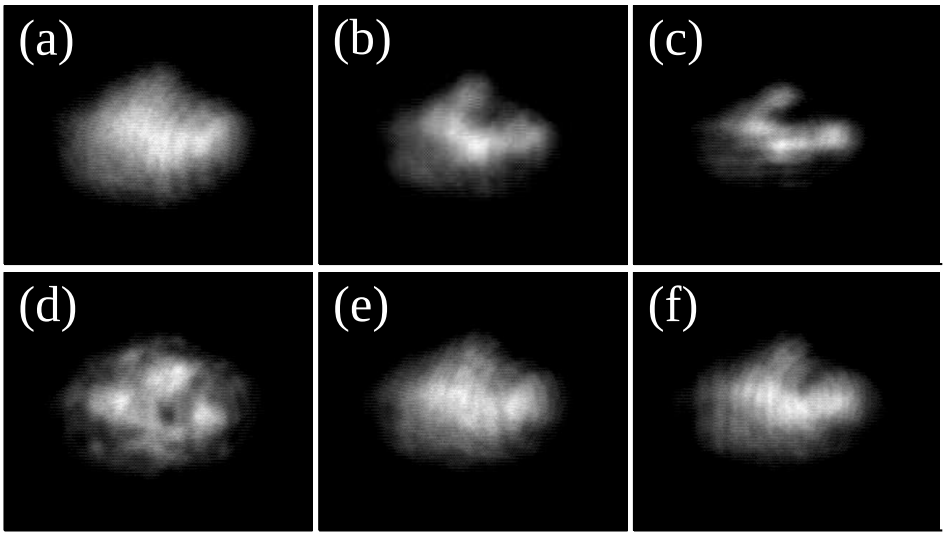

Figure 2.2: Beam profiles after the fused-silica sample (a) in the linear propagation regime, (b) at high intensity without compensation, (c) with BBO Kerr phase shift only, (d) with cascade overcompensating Kerr phase, (e) with cascade optimally compensating Kerr phase, and (f) with cascade undercompensating Kerr phase.

by the standard Bespalov-Talanov perturbation analysis [3].

To quantify the effects of compensation on WBSF we take vertical line scans through the profiles in Fig. 2.2. WBSF is isolated from SSSF by looking at scans displaced horizontally from the beam center by 25% of the beam diameter, where the peak intensity and hence the effects of SSSF are lessened. The inset of Fig. 2.3 shows these scans in the linear, uncompensated, and optimally compensated cases. Fig. 2.3 shows the measured beam waist for a range of phase-mismatch values. $\Delta kL = -75\pi$ corresponds to $\Phi^{NL}_{cascade} > 0$, which adds to the self-focusing in the fused silica, as expected.

We can characterize SSSF by taking vertical line scans through the data (Fig. 2.2), but at the beam center. The inset of Fig. 2.4 shows the beam profiles

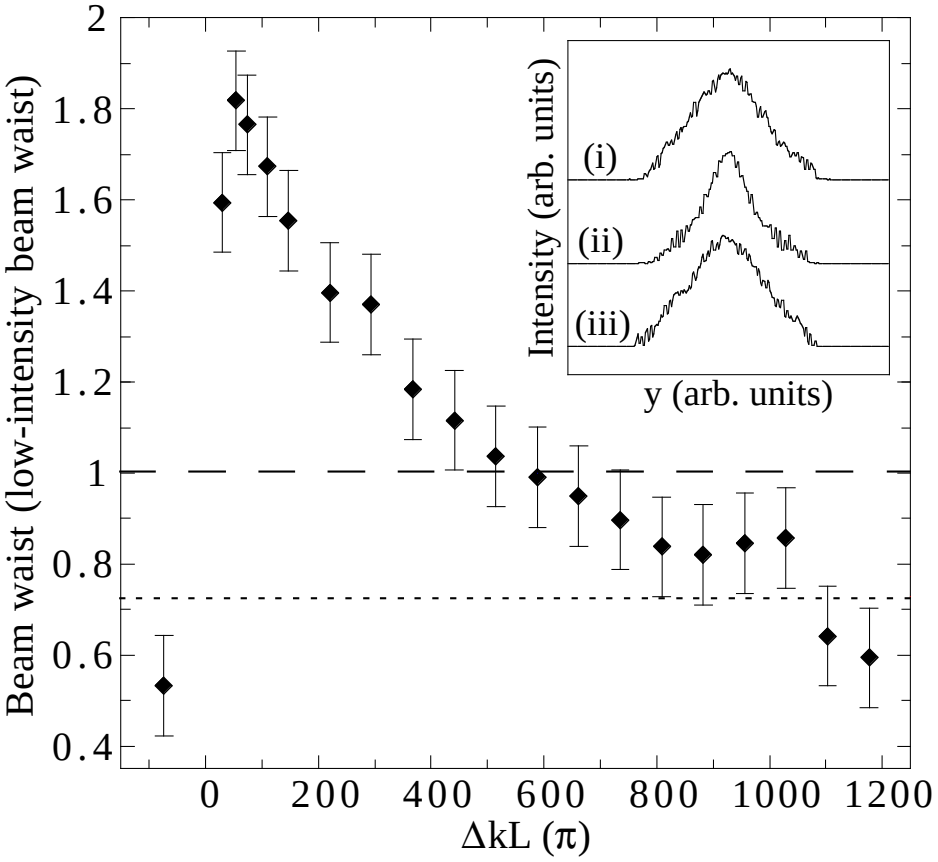

Figure 2.3: Beam waist versus ΔkL in units of the low-intensity beam waist (dashed line). The dotted line shows the beam waist without compensation. Inset shows vertical line scans of the transverse intensity profile at the horizontal beam wing for (i) linear propagation, (ii) uncompensated WBSF, and (iii) optimal compensation at $\Delta kL \approx 520\pi$.

for the linear, uncompensated, and optimally compensated cases. Compensation eliminates nearly all modulation from SSSF. The phase-mismatch for optimal SSSF compensation is slightly larger than for WBSF (580π versus 520π, respectively). This is understood: The phase accumulated in the compensation stage alters the intensity profile (through self-defocusing), so the phase accumulated in the fused silica will have slightly different spatial shape than the compensating phase. This leads to different optimal compensation values for the peak phase (related strongly to SSSF) versus the average phase (related more to WBSF) [5].

SSSF increases the contrast across the beam profile, so it can be quantified by looking at the deviation of a given line scan from an ideal Gaussian profile. Fig. 2.4 shows this deviation versus phase-mismatch. The apparent smoothing for $\Delta kL \rightarrow 0^+$ is not useful, since the FH is depleted by SHG and then an observed optical parametric generation process which happens to be phase-matched on this region. This presents itself as a slight rolloff in beam waist in the WBSF data as expected, since the gain for WBSF is less than for SSSF.

Cascade quadratic phase shifts can also be used to compensate for SPM. The narrow bandwidth of picosecond pulses makes stretching difficult, so the B integral tends to be a significant concern in picosecond amplifiers. We investigated compensation of the B integral in a single-pass amplifier. Transform-limited pulses of duration 5 ps and energy 0.5 mJ propagate through a 2-cm long Ti:sapphire crystal where they acquire $\Phi_{Kerr}^{NL} \approx \pi$ and the spectrum broadens to $\sim$3.2 times the transform limit. Equ. (2.1) predicts optimal compensation at $\Delta kL \approx 7\pi$ with L = 1.7 cm. With a 1.7-cm long piece of BBO, we observe that the spectrum is compressed to $\sim$1.5 times transform limit with $\Delta kL \approx 5\pi$ (Fig. 2.5). We believe that full compensation is possible, but the results of Fig. 2.5 are within a factor of

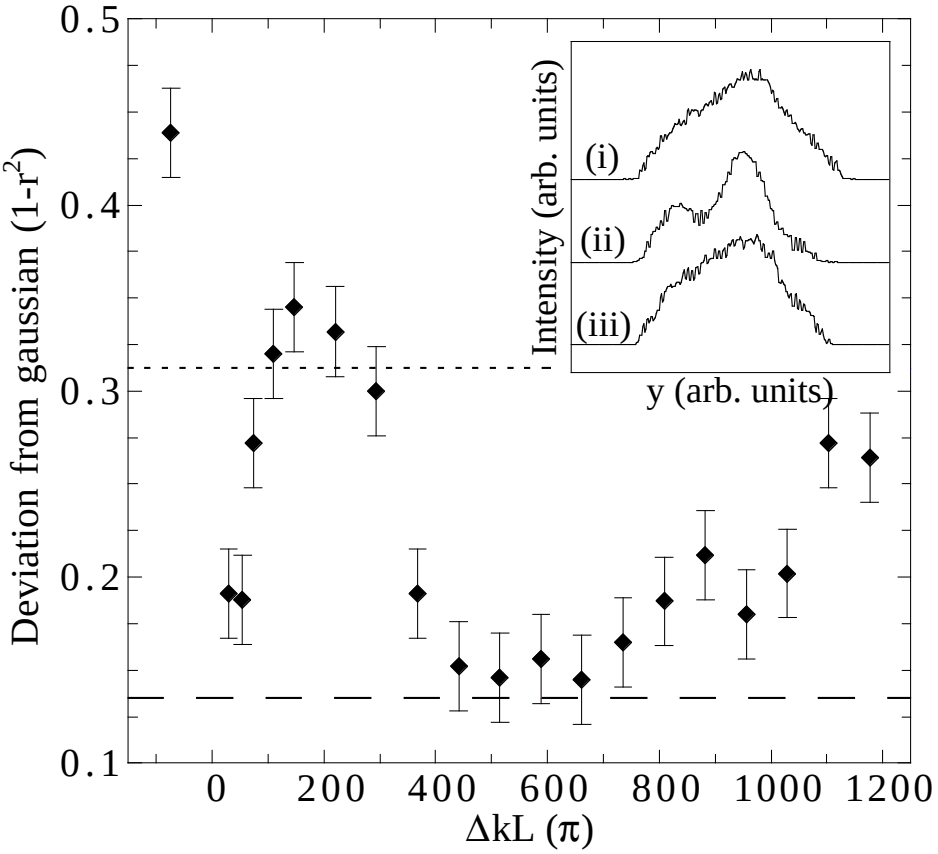

Figure 2.4: Deviation of the beam from Gaussian versus ΔkL where 0 represents a perfectly Gaussian beam and the dashed line represents the deviation in the low-intensity propagation regime. The dotted line represents deviation without compensation. The inset shows vertical line scans of the transverse intensity profile at the horizontal beam center for (i) linear propagation, (ii) uncompensated SSSF, and (iii) optimal compensation at $\Delta kL \approx 580\pi$.

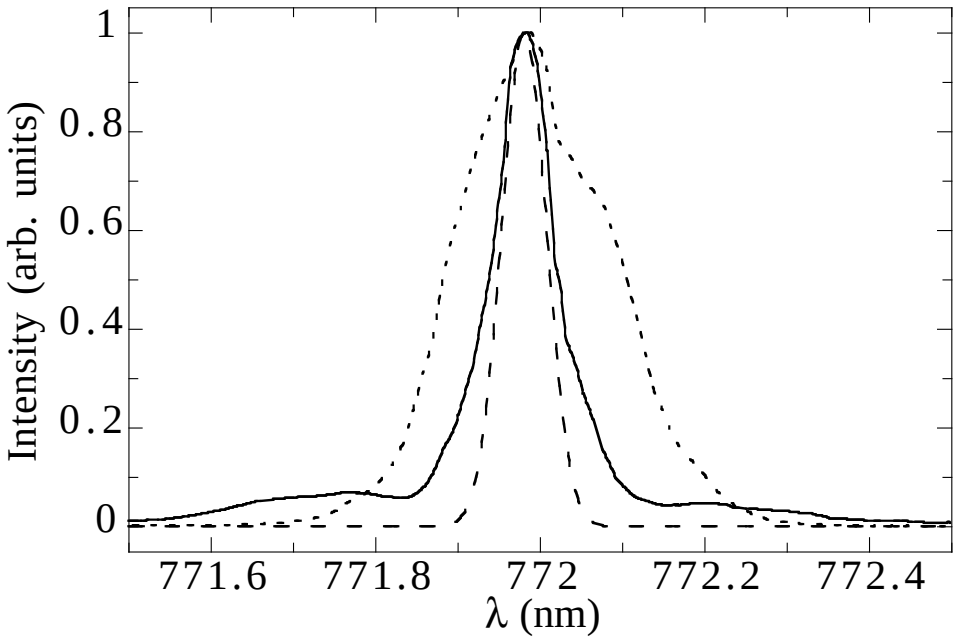

Figure 2.5: Spectrum of the uncompensated Ti:sapphire amplifier output (dotted line), after compensation (solid line), and the spectrum corresponding to transform limit (dashed line).

2 of the limits that arise from GVM and crystal damage [11]. The wings present in the compensated spectra are most likely due to spatial intensity modulation present in the output of the amplifier.

2.4 Conclusion

In conclusion, we have demonstrated the compensation of nonlinear phase shifts on the order of π by use of cascade quadratic processes. This compensation scheme is easily scalable to high peak intensity ($\sim$100 GW/cm^2 for femtosecond pulses), has low inherent loss ($\lesssim 1\%$ was observed), and is easily tunable at fixed intensity and crystal length. We demonstrate compensation with femtosecond and picosec-

ond pulses, but the process should be easier to implement with longer pulses. In particular, cascade self-focusing compensation could prove important in the construction of high-power nanosecond- and picosecond-pulse lasers, where beam distortion from SSSF limits the maximum attainable power. Also, the B integral compensation reported here raises the possiblity of pass-by-pass compensation of SPM inside the RA cavity. Thus, it should be possible to design a RA without pulse stretching and compression.

This work was supported by the National Institutes of Health under grant RR10075, and the National Science Foundation. L. Q. acknowledges support from the Natural Science Foundation in China.

BIBLIOGRAPHY

[1] K. Beckwitt, F. W. Wise, L. Qian, L. A. Walker II, and E. Canto-Said, Opt. Lett. **26**, 1696 (2001).

[2] See for example: E. S. Bliss, D. R. Speck, J. F. Holzrichter, J. H. Erkkila, and A. J. Glass, Appl. Phys. Lett. **25**, 448 (1974).

[3] See for example: G. P. Agrawal, *Nonlinear Fiber Optics*, 2nd ed., Academic Press, San Diego (1995).

[4] D. Strickland and G. Mourou, Opt. Commun. **56**, 219 (1985).

[5] U. Roth, F. Loewenthal, R. Tommasini, J. E. Balmer, and H. P. Weber, IEEE J. Quantum Electron. **36**, 687 (2000).

[6] O. A. Konoplev and D. D. Meyerhofer, IEEE J. Select. Top. Quant. Electron., **4**, 459 (1998).

[7] R. DeSalvo, D. J. Hagan, M. Sheik-Bahae, G. Stegeman, E. W. Van Stryland, and H. Vanherzeele, H., Opt. Lett. **17**, 28 (1992).

[8] X. Liu, K. Beckwitt, and F. W. Wise, Phys. Rev. E **62**, 1328 (2000).

[9] X. Liu, L. Qian, and F. W. Wise, Opt. Lett. **24**, 1777 (1999).

[10] S.-U. Alam, G. Biffi, A. B. Grudinin, and G. Burdge, Optical Fiber Conference 1999, San Diego, USA, Paper ThA2.

[11] GVM limit from the condition given in [[8]].

Chapter 3

Temporal solitons in quadratic nonlinear media with opposite group-velocity dispersions at the fundamental and second harmonics[1]

Temporal solitons in quadratic nonlinear media with *normal* second-harmonic dispersion are studied theoretically. The variational approximation and direct simulations reveal the existence of soliton solutions, and their stability region is identified. Stable solutions are found for large and normal values of the second-harmonic dispersion, and in the presence of large group-velocity mismatch between the fundamental- and second-harmonic fields. The solitons (or solitonlike pulses) are found to have tiny non-localized tails in the second-harmonic field, for which an analytic exponential estimate is obtained. The estimate and numerical calculations show that, in the parameter region of experimental relevance, the tails are completely negligible. The results open a way to the experimental observation of quadratic solitons with normal second-harmonic dispersion, and have strong implication to the experimental search for multidimensional "light bullets."

3.1 Introduction

Optical solitons are localized electromagnetic waves that propagate steadily in nonlinear media resulting from a robust balance between nonlinearity and linear

[1]The results presented in this chapter have been published in Ref. [1].

broadening due to dispersion and/or diffraction. It is well known that cubic nonlinear materials support temporal solitons [2], but that the resulting balance is unstable to collapse in higher than one dimension [3]. This collapse is arrested in materials with *saturable* nonlinearity [4, 5], allowing for the formation of solitons in two and three dimensions (2D and 3D).

Of great interest, theoretically and experimentally, are spatiotemporal solitons (STS) confined in time and both transverse spatial dimensions ("light bullets") [6]. Unlike temporal solitons, spatial solitons, and quasi-STS (STS confined only in one transverse dimension), light bullets are the only truly stable solitons in a three-dimensional geometry [7]. In addition to their fundamental significance, STS are of interest for their technological applications, as they provide for the possibility of terahertz switching rates when utilized in optical digital logic [8].

In recent years, spatial solitons have been extensively studied in systems with saturable nonlinearity resulting from the photorefractive effect in electro-optic materials [9], and in quadratic nonlinear media, with an effectively saturable nonlinearity resulting from cascaded quadratic processes [10, 9]. Theoretically, many kinds of solitons in quadratic nonlinear media have received significant attention (for review see Refs. [11] and [12]). However, quadratic temporal solitons [13] and (2+1)D STS [14, 15] have been observed only recently. The main impediment to the formation of temporal solitons (and STS) in quadratic materials is the historically perceived need for large anomalous group-velocity dispersion (GVD) at both the fundamental frequency (FF) and the second harmonic (SH). In particular, the above mentioned experiments utilized anomalous GVD that was induced by angular dispersion from a grating (pulse-tilting) to overcome the normal material GVD present at the wavelengths studied. However, pulse-tilting consumes a transverse

degree of freedom, preventing soliton confinement along that dimension. This lack of confinement was seen by Liu *et al.* who observed (3+1)D filaments resulting from the transverse instability of (2+1)D STS [16]. These filaments were similar in nature to light bullets, but did not propagate stably due to residual angular dispersion from the pulse-tilting technique. To date, all experiments observing temporal solitons and STS in quadratic media have utilized pulse tilting, so there is significant motivation to generate quadratic temporal solitons in systems without pulse tilt, where the extension to light bullets is possible.

Surveying available quadratic materials leads to the conclusion that large anomalous GVD at the FF is accessible, without significant linear absorption, if this frequency is chosen in the infrared; however, the GVD is accompanied by significant group-velocity mismatch (GVM) between the FF and SH. In addition, in this case the GVD at the SH ranges from near zero to large normal values. So, one is motivated to consider solitons with *normal* GVD at the SH. Recently, STS in the (2+1)D and (3+1)D cases were considered under these conditions [17]. It was found that, for a limited range of parameters, solitons (or solitonlike pulses with tiny nonlocalized tails which would not be experimentally accessible) do exist for normal GVD at the SH and in the presence of some GVM. However, the existence and stability of the more fundamental temporal solitons (*i.e.*, 1D rather than multidimensional pulses) under conditions of normal GVD at the SH has never been considered. This is the subject of the present work.

Temporal solitons in this system are particularly interesting from an experimental standpoint. If observed without the pulse-tilting technique, these would be the crucial step to the formation of true light bullets (either directly through modulation instability in the spatial domain or by launching STS under conditions

similar to those for temporal solitons). On the other hand, one would naturally expect the stability requirements for solitons in 1D to be less stringent than for STS, allowing formation and observation of the solitons over a broader and *more experimentally accessible* range of values of the GVM and normal GVD at the SH.

Below, we present results of both analytical [based on the variational approximation, (VA)] and direct numerical investigations of temporal solitons in quadratic media with normal GVD at the SH. We show that while the resulting solitary pulses feature the aforementioned nonlocalized tails and thus are not localized in the rigorous sense, with proper choice of the parameters they may be completely localized in any practical sense, so that the resulting waves are indistinguishable from genuine solitons over experimentally accessible propagation lengths. In addition, the pulses are shown to persist in the presence of significant GVM between the FF and SH fields, which is crucial to their experimental observation since *all* quadratic materials give rise to GVM. Solitonlike solutions are demonstrated under accessible experimental parameters, and the implications of the results to the formation of (2+1)D and (3+1)D STS in these systems are discussed.

3.2 Analytical and numerical results

Within the commonly adopted slowly varying envelope approximation, the coupled equations governing the interaction of the FF and SH field envelopes (u and v, respectively) propagating in the z direction in a medium with quadratic nonlinearity are [7, 18]

$$iu_z + u_{\tau\tau} + u^* v - u = 0, \tag{3.1}$$

$$2i(v_z + \sigma v_\tau) + \delta v_{\tau\tau} + \frac{u^2}{2} - \alpha v \;\; = \;\; 0. \tag{3.2}$$

Here u and v are related to the fields E_1 and E_2 (in units of the initial peak FF field E_0) by $E_1 = (u/2)e^{iz}$, $E_2 = ve^{i(\alpha/2)z}$, and $\alpha = 4 - 2\Delta k Z_I$; $\Delta k = k_{2\omega} - 2k_\omega$ is the wave-vector mismatch between the FF and SH fields, and $Z_I = n\lambda/\pi\chi^{(2)}E_0$ characterizes the strength of the nonlinear coupling. The GVM parameter $\sigma = \sqrt{2L_{DS,1}Z_I/L_{GVM}^2}$ is expressed in terms of the dispersion and GVM lengths $L_{DS,j} = {\tau_0}^2/|\beta_j^{(2)}|$ and $L_{GVM} = c\tau_0/(n_{1,g} - n_{2,g})$, respectively, for material dispersion $\beta_j^{(2)}$ and group-velocity index $n_{j,g}$ at frequency ω_j with $j = 1, 2$. Time τ and propagation coordinate z are normalized by $\sqrt{Z_I/2L_{DS,1}}$ and Z_I, respectively. $\delta \equiv 2\beta_2^{(2)}/\beta_1^{(2)}$ is the ratio between the GVD at the SH and FF. In Eqs. 3.1 and 3.2 the GVD at the FF is assumed to be anomalous, so that $\delta > 0$ and $\delta < 0$ correspond, respectively, to anomalous and normal GVDs at the SH. While it is true that soliton solutions are expected with normal GVD at both the FF *and* the SH (and negative nonlinearity), this case is not really different from the usual one. However, the results reported here are equally applicable to the case of normal GVD at the FF and slightly anomalous GVD at the SH, which is also physically realizable in available quadratic media. It is important to note, however, that in the multidimensional case diffraction only has one sign, and the existence of localized solutions demands that the sign of the GVD term in the FF equation [Eq. (3.1)] be the same as that of diffraction. Hence only the case of anomalous GVD at the FF can give rise to multidimensional solitons.

Our consideration is broken into three parts: analysis of solutions to Eqs. (3.1) and (3.2) using the VA in the zero-GVM limit, numerical simulation of the

propagation equations without GVM, and finally a study of the effects of GVM on the resulting solutions.

In the zero-GVM case ($\sigma = 0$), the VA is applied to Eqs. (3.1) and (3.2) with $\delta < 0$. Starting with the real Gaussian *ansatz*, $u = A \exp(-\rho\tau^2)$, $v = B \exp(-\gamma\tau^2)$, we arrive at an equation for the temporal-width parameter ρ (cf. Ref. [19]):

$$20\delta\rho^3 + (4\delta - 3\alpha)\rho^2 + 4\alpha\rho - \alpha = 0. \tag{3.3}$$

Equating the discriminant of Eq. (3.3) to zero yields the boundary

$$\alpha_0 = \text{const} \cdot \delta, \quad \text{const} \approx -13.6075\ldots, \tag{3.4}$$

above which (*i.e.*, for $\alpha > \alpha_0$) real solutions exist. Using ρ obtained from Eq. (3.3) and the underlying Gaussian *ansatz*, we construct an initial guess and employ the shooting method to obtain numerically exact stationary solutions to Eqs. (3.1) and (3.2) (see Fig. 3.3 for a typical example, to be discussed).

The stability of the stationary solutions, which is a critical issue, was tested by direct simulations of Eqs. (3.1) and (3.2) using a symmetric split-step beam-propagation method as described in Ref. [15]. Points symbolizing stable and unstable propagation are collected in Fig. 3.1, along with the soliton-existence boundary, as predicted by the VA in the form of Eq. (3.4). Gaussian profiles are launched in the numerical simulations (as is further discussed later), and absorp-

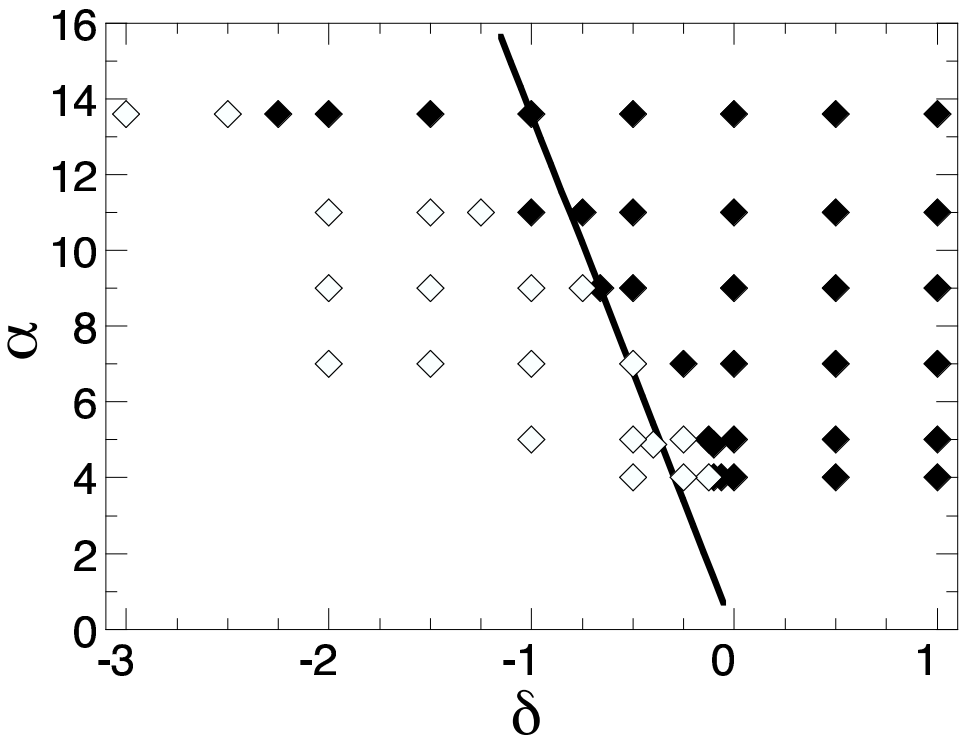

Figure 3.1: Stability region for solutions near $\delta = 0$. Filled (empty) diamonds show numerically stable (unstable) solutions. Stability is determined by examining evolution of the solutions over ~ 64 dispersion lengths. The line is the soliton-existence boundary [Eq. (3.4)], predicted by the VA (stable solutions are predicted to the right of the boundary). Results are for the case of zero GVM ($\sigma = 0$).

tive boundary conditions are employed to suppress energy radiated beyond the calculation window.

The agreement between Eq. (3.4) and the actual border of the stable solutions, as found from the simulations, is quite reasonable, and is better for small α. With increasing α (which implies approaching the known cascading limit [11, 12]), stable solutions are found for somewhat *larger* $|\delta|$ (*i.e.*, larger normal GVD at the SH) than predicted by the VA. Somewhat surprisingly, stable solutions are found for

quite large values of $|\delta|$, up to $\delta \sim -2$, with the appropriate choice of α. For instance, Fig. 3.2 displays stable propagation of the solution with $\delta = -2$ [*i.e.*, GVD(2ω) = -GVD(ω)] and $\alpha = 13.6$. This is in contrast to the results for the (2+1)D and (3+1)D cases [17], where STS are found to be stable only for much smaller values ($|\delta| \lesssim 0.15$). In Fig. 3.1, stability is defined by the requirement that less than ∼5% of the energy in the formed field is lost after propagation through ∼64 dispersion lengths; some solutions near the boundary which are characterized as unstable only decay by ∼5-20% (with the decay increasing further into the normal SH GVD regime).

Despite the robustness of the pulses in numerical simulations, their strict localization must be addressed. This issue is particularly important due to the counter-intuitive nature of stable or even quasi-stable pulses with normal GVD at the SH. If a small delocalized [continuous wave, (CW)] component is present in the SH, linearization of Eqs. (3.1) and (3.2) shows that it has the form $v = b\ \cos(\sqrt{(\alpha/|\delta|)}|\tau| + \phi_0)$ where ϕ_0 is an unknown constant, and b is the tail's amplitude. b can be estimated by solving the linearized version of Eq. (3.1) for u, and using the result to solve Eq. (3.2) with the source (driving term) $u^2/2$. The source is Fourier transformed, and then its product with the Green's function for the SH field is inverse transformed. Following these lines (cf. Ref. [17], where similar analysis was performed for the multidimensional case), it is possible to isolate a term in the solution representing the CW "tail," and arrive at an estimate for the tail's amplitude,

$$b \sim \exp(-C\sqrt{\alpha/|\delta|}), \tag{3.5}$$

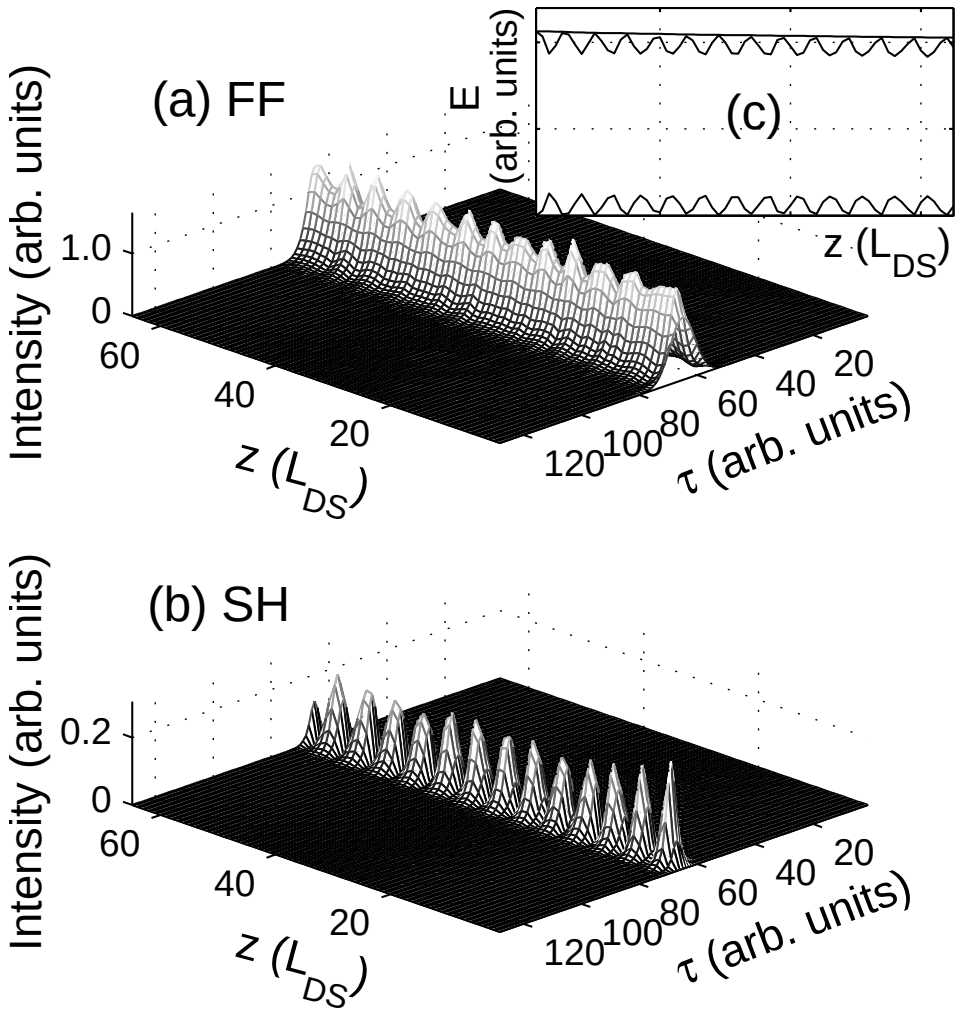

Figure 3.2: Evolution of the FF (a) and SH (b) fields for $\alpha = 13.6$ and $\delta = -2$. A Gaussian pulse was launched solely in the FF field. Propagation is over ~ 64 dispersion lengths. Inset (c) shows the time-integrated total energy (line), as well as the energy in the FF (upper), and SH (lower) components.

where C is an unknown constant.

To test Eq. (3.5) we use the shooting method as described above with $\delta = -0.15$ and various values of α (numerical error of the shooting method is estimated to be $\sim O(10^{-5})$). Fig. 3.3 shows the dependence of the resulting tail's amplitude on α, along with a fit to Eq. (3.5). Up to $\alpha \approx 20$, the decay of the tail amplitude follows Eq. (3.5) closely. For still larger α, the tail amplitude b decays slower.

The presence of the tail means that the solutions found are not strictly localized; however, for appropriate α and δ the SH peak-to-tail ratio can be easily made $\gtrsim 10^4$. This explains why no decay is observed in Fig. 3.2 (and in simulations of other stable solutions with $\delta < 0$ in Fig. 3.1). Pulses with an exponentially small CW component will appear as true solitons in any feasible experiment. The conditions under which the tails are minimized (large α) correspond precisely to the transition to an effective Kerr-like medium in the cascading limit, when the sign of the SH dispersion is not significant. Notice also the close proximity of the numerical solutions to the Gaussian *ansatz*. Based on this, Gaussian profiles are launched in numerical simulations.

It is also necessary to address the effect of GVM (σ) on the stability of the solutions. Numerically, we study the effects of GVM by direct simulations, starting from a point in the (α, δ) plane with known stable solution for $\sigma = 0$, and increasing σ. Fig. 3.4 shows the stable solution at $\alpha = 13.6$, $\delta = -0.5$, with increasing GVM. It is apparent from the figure that small GVM ($\sigma \lesssim 2$) has little effect on the stability of the solution. Remarkably, some of the soliton keeps a part of its energy for GVM up to $\sigma \sim 30$. This is unlike in higher dimensions [17], where GVM very quickly destabilizes the solitons. At conditions that correspond to realistic experimental parameters in quadratic nonlinear media, this corresponds to GVM

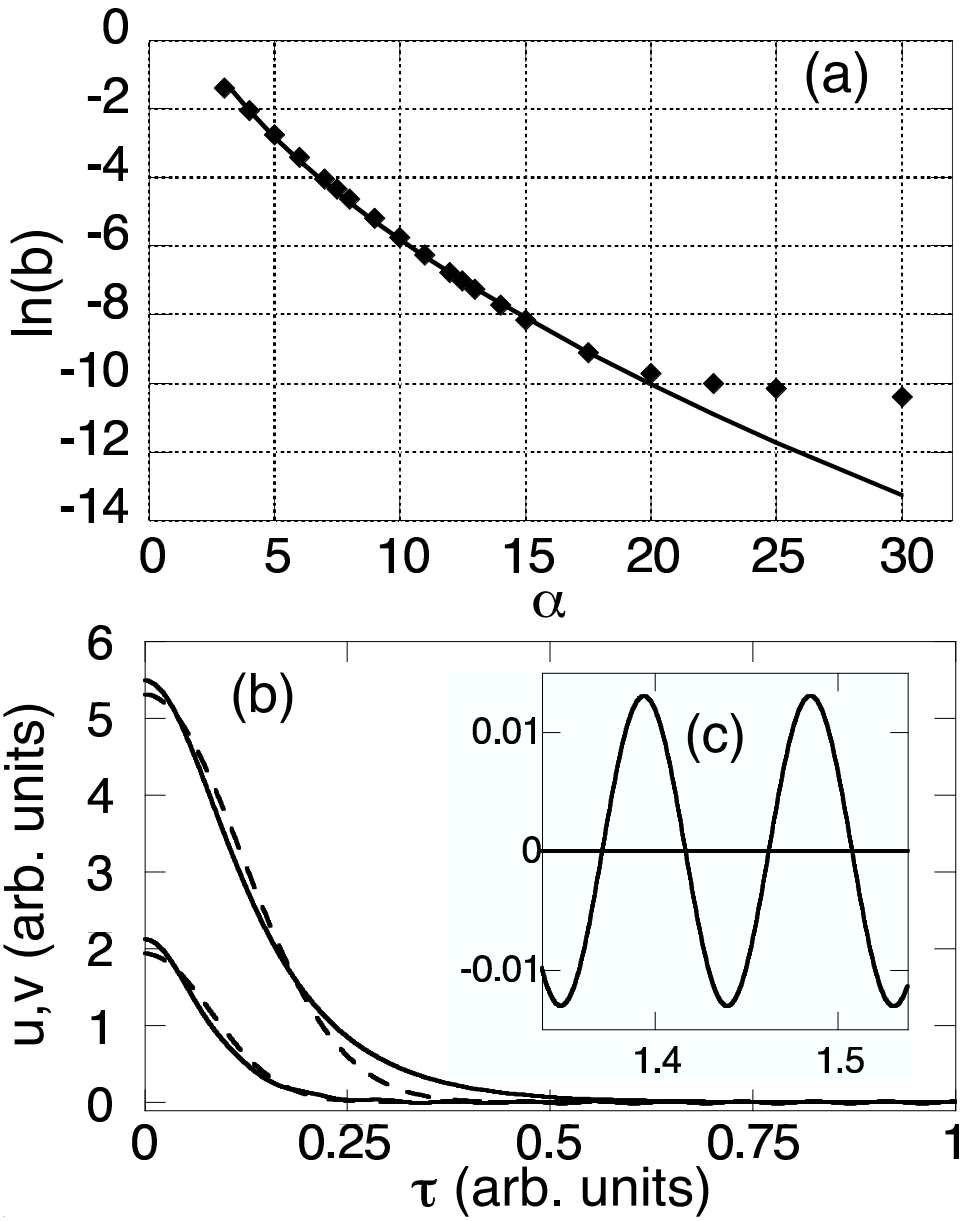

Figure 3.3: (a) The amplitude of the CW component (tail) of the SH field (diamonds), as found from the shooting solution of Eq. (3.3) with $\delta = -0.15$, vs. α. The line indicates the predicted dependence in the form of Eq. (3.5). (b) The shooting results (solid line) and the corresponding VA prediction (dashed line) for u and v (upper and lower traces, respectively) with $\alpha = 7.5$. The zoomed region in (c) shows the residual oscillatory SH tail present in (b).

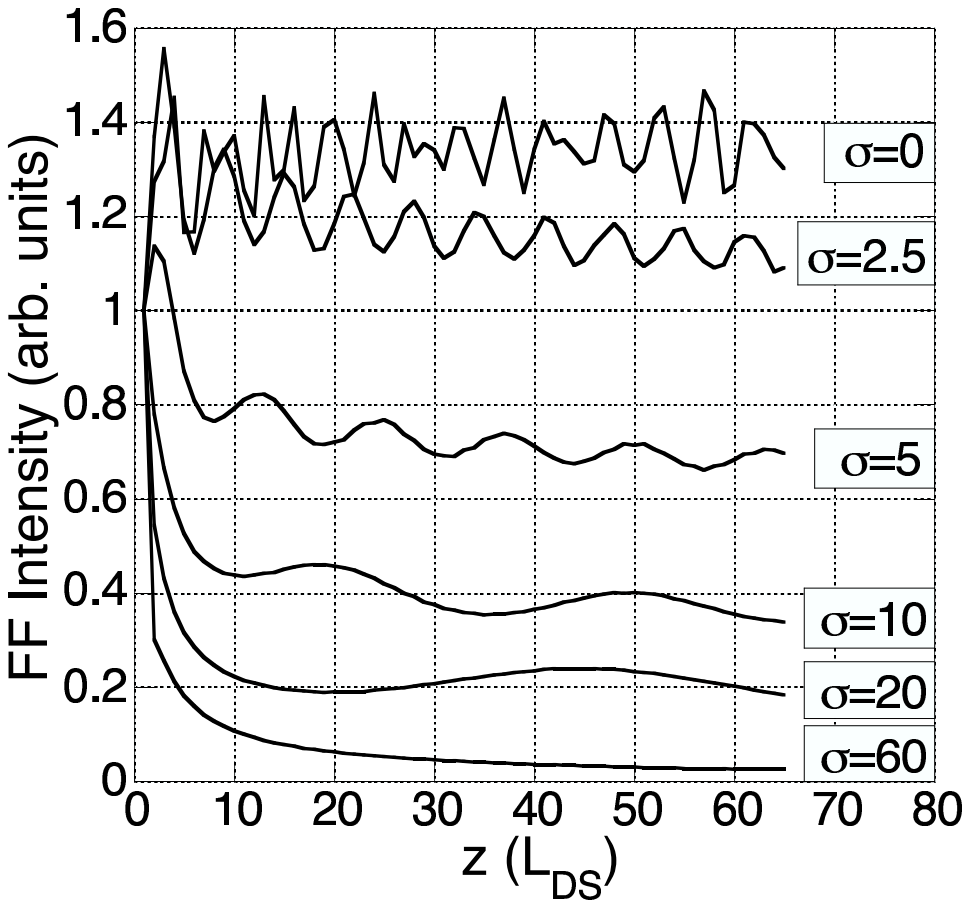

Figure 3.4: Peak FF profiles showing effects of increased GVM on soliton formation at $\alpha = 13.6$ and $\delta = -0.5$. Up to $\sigma \approx 1.2$ profile shows no decay. As in Figs. 3.1-3.2, a Gaussian FF profile is launched.

of several picosecond/millimeter.

This result greatly increases the chance of observing the solitons experimentally. Values of the normalized parameters for the commonly used quadratic material periodically poled lithium niobate in the infrared (at $\lambda \sim 3$ μm) are $\alpha \approx 12$, $\delta \approx -0.5$, and $\sigma \approx 1.3$, which are well within the effective stability range found above for the solitons. The initial point in (α, δ) used in Fig. 3.4 was picked from the stability region of Fig. 3.1. Starting closer to the boundary yields somewhat

less resilience to GVM, as expected.

While realistic material parameters most likely necessitate working with $\sigma > 0$, solitonlike solutions with normal GVD at the SH present a new degree of freedom in the space of experimental parameters. In particular, most available quadratic media have a zero GVM point in the infrared, but at wavelengths corresponding to large normal GVD at the SH. Thus, the ability to work with normal SH dispersion could allow experimental study of solitons with *zero* GVM (in addition to large values of σ). Given present materials this is unlikely to apply to STS, where the requirements on δ are much more restrictive.

3.3 Conclusion

In summary we have demonstrated that quadratic nonlinear media support temporal solitons with normal GVD at the SH. Formally, these solutions are not strictly localized; however, with appropriate choice of the parameters, the residual CW tail in the SH field can be reduced to $\lesssim 10^{-4}$ of the soliton's amplitude. Experimentally there should be no detectable difference between these and true soliton solutions over measurable propagation lengths. Numerically, the soliton solutions survive even in the presence of significant GVM. This should provide an important medium for the study of quadratic solitons in the temporal and, eventually, spatiotemporal domains.

This work was supported by the National Science Foundation under Grant No. PHY-0099564, and the Binational (U.S.-Israel) Science Foundation (Contract No. 1999459). We thank D. Mihalache, A. V. Buryak, L. Torner, I. N. Towers, L. Qian, and H. Zhu for valuable discussions. Computational facilities were provided by the Cornell Center for Materials Research and the Cornell Theory Center.

BIBLIOGRAPHY

[1] K. Beckwitt, Y.-F. Chen, F. W. Wise, and B. A. Malomed, Phys. Rev. E **68**, 057601 (2003).

[2] G. P. Agrawal. *Nonlinear Fiber Optics* (Academic Press: San Diego, 1995).

[3] V. E. Zakharov and A. M. Rubenchik, Zh. Éksp. Teor. Fiz. **65**, 997 (1973) [Sov. Phys. JETP **38**, 494 (1974)].

[4] A. B. Blagoeva, S. G. Dinev, A. A. Dreischuh, and A. Naidenov, IEEE J. Quantum Electron. **QE-27**, 2060 (1991).

[5] D. E. Edmundson and R. H. Enns, Opt. Lett. **17**, 586 (1992).

[6] Y. Silberberg, Opt. Lett. **15**, 1282 (1990).

[7] A. A. Kanashov and A. M. Rubenchik, Physica D **4**, 122 (1981).

[8] R. McLeod, K. Wagner, and S. Blair, Phys. Rev. A **52**. 3254 (1995).

[9] G. I. Stegeman and M. Segev, Science **286**, 1518 (1999).

[10] R. DeSalvo, D. J. Hagan, M. Sheik-Bahae, G. Stegeman, E. W. Van Stryland, and H. Vanherzeele, Opt. Lett. **17**, 28 (1992).

[11] C. Etrich, F. Lederer, B.A. Malomed, T. Peschel, and U. Peschel, Progr. Opt. **41**, 483 (2000).

[12] A.V. Buryak, P. Di Trapani, D.V. Skryabin and S. Trillo, Physics Reports **370**, 63 (2002).

[13] G. Valiulis, A. Dubietis, R. Danielius, D. Caironi, A. Visconti, and P. Di Trapani, J. Opt. Soc. Am. B **16**, 722 (1999).

[14] X. Liu, L. J. Qian, and F. W. Wise, Phys. Rev. Lett. **82**, 4631 (1999).

[15] X. Liu, K. Beckwitt, and F. W. Wise, Phys. Rev. E **22**, 1328 (2000)

[16] X. Liu, K. Beckwitt, and F. W. Wise, Phys. Rev. Lett. **85**, 1871 (2000).

[17] I. N. Towers, B. A. Malomed, and F. W. Wise, Phys. Rev. Lett. **90** 123902 (2003).

[18] B. A. Malomed, P. Drummond, H. He, A. Berntson, D. Anderson and M. Lisak, Phys. Rev. E **56**, 4725 (1997).

[19] V. Steblina, Yu.S. Kivshar, M. Lisak, and B.A. Malomed. Opt. Comm. **118**, 345 (1995).

Chapter 4

Controllable Raman-like nonlinearities from nonstationary, cascaded quadratic processes[1]

We show that useful non-instantaneous, nonlinear phase shifts can be obtained from cascaded quadratic processes in the presence of group-velocity mismatch. The two-field nature of the process permits responses that can be effectively advanced or retarded in time with respect to one of the fields. There is an analogy to a generalized Raman-scattering effect, permitting both redshifts and blueshifts of short pulses. We expect this capability to have many applications in short-pulse generation and propagation, such as the compensation of Raman-induced effects and high-quality pulse compression, which we discuss.

4.1 Introduction

In the past decade, there has been much interest in the nonlinear phase shifts produced by the cascaded interactions of two or three waves in quadratic ($\chi^{(2)}$) nonlinear media. Large nonlinear phase shifts of controllable sign can be generated, and numerous applications of such a capability can be envisioned [2]. The prototypical quadratic process is second-harmonic generation (SHG). During the propagation of a fundamental-frequency (FF) field along with its second-harmonic (SH), the FF accumulates a nonlinear phase shift (Φ^{NL}) if the process is not phase-matched. With long pulses (nanosecond duration in practice) the FF and SH fields over-

[1]The results presented in this chapter have been published in Ref. [1].

lap temporally despite their different group velocities. In this so-called stationary limit, an effective Kerr nonlinearity is obtained (except at high intensity, when the fundamental field is depleted), and this can be a surrogate for the bound electronic cubic ($\chi^{(3)}$) nonlinearity [3]. The cascade nonlinear phase shift can be thought of as arising from an effective nonlinear refractive index, *i.e.*, the real part of an effective susceptibility. The residual SHG that occurs in the phase-mismatch process can similarly be considered the analog of two-photon absorption (the corresponding imaginary part of the effective susceptibility).

The use of cascaded quadratic processes with ultrashort pulses is complicated substantially by the group-velocity mismatch (GVM) between the FF and SH fields [5, 4]. GVM causes the fields to move apart in time, which reduces their coupling, and thus the magnitude of the cascade effects. In addition, the temporal profile of the nonlinear phase shift becomes distorted. Deviations of $\Phi^{NL}(t)$ from the pulse intensity profile hamper or preclude applications that involve solitonlike pulse shaping. The solution to this problem amounts to recovery of the stationary regime: For a given value of the GVM, the phase mismatch is increased so that the cycles of conversion and backconversion that generate the nonlinear phase shift occur before the pulses move apart from each other in time. Liu *et al.* and Wise *et al.* showed that acceptable phase-shift quality can be obtained if at least two conversion cycles occur per characteristic GVM length $L_{\mathrm{GVM}} = 0.6c\tau_0/(n_{g,1}-n_{g,2})$, which implies $\Delta k > 4\pi/L_{\mathrm{GVM}}$ [6, 7]. Here, c is the speed of light in vacuum, τ_0 is the full-width at half-maximum (FWHM) of the pulse, and $n_{g,1}$ and $n_{g,2}$ are the group refractive indices for the FF and SH, respectively. In the limit of large phase mismatch an exact replica of a cubic nonlinearity is asymptotically obtained [3]. The disadvantage of working with large phase mismatch is reduced magnitude of

the nonlinear phase shift. GVM thus places a strong constraint on applications of cascade phase shifts. As one example, increasing GVM reduces the fraction of launched pulse energy that evolves into a soliton eventually to zero [8]. To date, applications of cascade phase shifts with femtosecond pulses [9, 6, 10, 11] have all been demonstrated under stationary conditions. Approaching the stationary boundary, GVM coupled with self-phase modulation has been observed to broaden asymmetrically the pulse spectrum [6, 12]

The nonlinear refraction experienced by an ultrashort pulse in a cubic nonlinear medium arises predominantly from bound-electronic and nuclear (*i.e.*, Raman) contributions to the nonlinear response. Here, we show that cascade phase shifts produced under nonstationary conditions mimic the Raman response with some remarkable properties. Frequency shifts of controllable sign and magnitude can be impressed on short pulses. These effective Stokes and anti-Stokes Raman processes complete the analogy between cascade nonlinearities and true cubic nonlinearities while maintaining the new degree of freedom provided by the quadratic interaction — control of the process through the phase mismatch. An interesting feature of the nonstationary cascade process is that it provides a controllable, noninstantaneous (and therefore nonlocal) nonlinearity. That the GVM alters the quadratic processes and produces deviations from a Kerr nonlinearity is well-known [5]. However, to date these effects have been perceived as distortions to be avoided. Just as the ability to control the sign and magnitude of an effective nonlinear index has enabled a new class of applications [2, 7], controllable Raman-like processes can be expected to create substantial new opportunities. We can think of cascade nonlinear processes with short pulses as dividing naturally into two classes separated by the criterion for obtaining nonlinear phase shifts that mimic those of purely

electronic origin. In this view, half of the possibilities of cascaded quadratic phase shifts have yet to be explored. Some examples of these processes will be discussed.

4.2 Analytical approach

The Kerr-like nonlinearity that arises from the $\chi^{(2)} : \chi^{(2)}$ process in the stationary limit can be understood qualitatively as follows. A small fraction of the FF is converted to the SH, which accumulates a phase difference before it is backconverted. The nonlinear phase shift impressed on the FF is delayed by one full cycle of conversion and backconversion. However, as long as the SH is not displaced temporally from the FF, the phase shift on the FF will be proportional to its intensity profile (Fig. 4.1). With short pulses, the GVM becomes important if the fields separate by approximately the pulse duration before a cycle of conversion and backconversion is complete. (We assume that the effect of the difference between the group-velocity dispersions (GVD) of the FF and the SH is negligible; in practice, it typically is much weaker than the interpulse GVM. This will be discussed quantitatively below.) Thus, after one cycle of conversion and backconversion, the intensity profile of the SH field is retarded or advanced with respect to that of the FF, depending on the sign of the GVM. The corresponding delay of the nonlinear phase is slightly smaller or larger than one full conversion cycle. As a result, an effectively advanced or retarded phase shift is accumulated by the FF. The corresponding effect in the spectral domain is a frequency shift toward the blue or the red. Such frequency shifts have been predicted through numerical calculations [5, 8].

The propagation of the FF and the SH are governed by coupled equations within the slowly varying envelope approximation (SVEA) [13]. We neglect self-

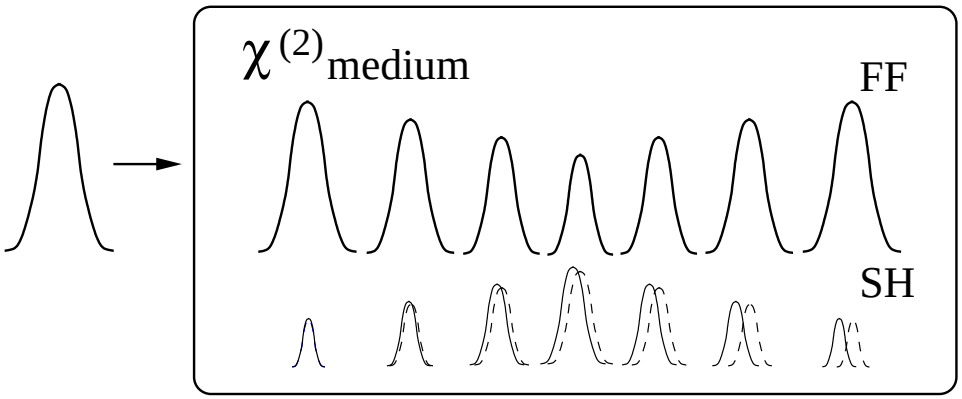

Figure 4.1: Illustration of the cascaded quadratic processes under phase-mismatch conditions. The FF is partially converted to the SH and then backconverted. Dashed (solid) curves are for the case of zero (nonzero) GVM.

and cross-phase modulation due to $\chi^{(3)}$, consider only the temporal dimension, and assume conditions for type I second harmonic generation, but the results can easily be generalized:

$$i\frac{\partial a_1}{\partial \xi} - \frac{\delta_1}{2}\frac{\partial^2 a_1}{\partial \tau^2} + a_1^* a_2 \exp(i\beta\xi) = 0, \tag{4.1}$$

$$i\frac{\partial a_2}{\partial \xi} - \frac{\delta_2}{2}\frac{\partial^2 a_2}{\partial \tau^2} - i\frac{\partial a_2}{\partial \tau} + a_1^2 \exp(-i\beta\xi) = 0. \tag{4.2}$$

Here a_1 and a_2 are the normalized FF and SH field amplitudes. Time is normalized to the initial pulse duration $\tau = t/\tau_0$ and the scaled propagation coordinate is $\xi = z/L_{\mathrm{GVM}}$. Here, $\delta_j = L_{\mathrm{GVM}}/L_{DS,j}$, where $L_{DS,j} = 0.322{\tau_0}^2/\mathrm{GVD}(\omega_j)$ are the dispersion lengths with $j = 1, 2$. The parameter $\beta = \Delta k L_{\mathrm{GVM}}$ where $\Delta k = k_{2\omega} - 2k_{\omega}$ is the normalized FF-SH wave-vector mismatch.

Consider the simple but common case when only FF light is incident on the

quadratic medium. In the limit of large phase-mismatch, conversion and backconversion occur rapidly and most of the energy resides in the FF at all times. A relation between the FF and the SH amplitudes can be derived as an expansion in powers of $1/\beta$ [3, 14]. By eliminating a_2 in Eq. (4.2) and keeping terms up to order $(1/\beta^3)$, an equation of motion for the FF field can be derived:

$$i\frac{\partial a_1}{\partial \xi} - \frac{\delta_1}{2}\frac{\partial^2 a_1}{\partial \tau^2} - \frac{1}{\beta}|a_1|^2 a_1 - 2i\frac{1}{\beta^2}|a_1|^2\frac{\partial a_1}{\partial \tau}$$

$$+\frac{1}{\beta^2}(\delta_1 - \delta_2)|a_1|^2\frac{\partial^2 a_1}{\partial \tau^2} - \frac{\delta_2}{\beta^2}a_1^*(\frac{\partial a_1}{\partial \tau})^2 + O(\frac{1}{|\beta|^3}) = 0. \tag{4.3}$$

The first three terms constitute a nonlinear Schrödinger equation (NLSE), which is generalized by the fourth and the fifth terms that describe the effects of the GVM, and the mismatch of the GVD of the FF and SH, respectively. The final term is negligible (at order $1/\beta^2$) since it is proportional to the square of the first derivative of the field envelope (a small quantity in the SVEA). In addition, it is even in time for well-behaved fields ($a_1(t)$) and hence cannot contribute to the frequency-shifting process. We neglect the GVD mismatch since its effect is much smaller than interpulse GVM for typical nonlinear media under the assumed conditions of small conversion to the SH. In that case, Eq. (4.3) reduces to:

$$i\frac{\partial a_1}{\partial \xi} - \frac{\delta_1}{2}\frac{\partial^2 a_1}{\partial \tau^2} - \frac{1}{\beta}|a_1|^2 a_1 - 2i\frac{1}{\beta^2}|a_1|^2\frac{\partial a_1}{\partial \tau} = 0. \tag{4.4}$$

We note that Eq. (4.4) resembles the Chen-Liu-Lee equation (CLLE), which is

integrable [15]. The difference is the presence of a cubic nonlinear term. It can be shown that Eq. (4.4) reduces to the CLLE:

$$i\frac{\partial q(Z,T)}{\partial Z} - \frac{\partial^2 q(Z,T)}{\partial T^2} + i|q(Z,T)|^2\frac{\partial q(Z,T)}{\partial T} = 0, \tag{4.5}$$

with the substitution

$$a_1(\xi,\tau) = c_0 \exp[i(c_1\xi + c_2 t)]q(\xi,\tau), \tag{4.6}$$

where $|c_0|^2 = \beta^2\sqrt{\delta_1/8}$, $c_1 = \delta_1\beta^2/8$, and $c_2 = \beta/2$, followed by the coordinate transformation

$$T = -\sqrt{2/\delta_1}\,\tau - \beta\sqrt{\delta_1/2}\,\xi, \tag{4.7}$$

$$Z = \xi. \tag{4.8}$$

Hence, Eq. (4.4) is integrable as well. We note that the CLLE is further related to the well-known, integrable derivative nonlinear Schrödinger equation through a gauge-invariant transformation [16].

To further understand the effects of the lowest-order correction from GVM in Eq. (4.4), we can compare it to the equation governing the propagation of a single field envelope a_1 under similar approximations to Eqs. (4.1) and (4.2), but for a Kerr-nonlinear material with finite Raman-response time T_R [17]:

$$\underbrace{i\frac{\partial a_1}{\partial \xi} - \frac{\delta_1}{2}\frac{\partial^2 a_1}{\partial \tau^2} + \gamma[|a_1|^2 a_1}_{\text{NLSE}} - \underbrace{T_R a_1 \frac{\partial |a_1|^2}{\partial \tau}}_{\text{Raman}}] = 0. \tag{4.9}$$

Here $\gamma = n_2\omega_0/(c\pi w^2)$ for a Gaussian beam with of frequency ω_0 and waist w. Comparing Eq. (4.9) with Eq. (4.4), we see that they are similar but with the Raman term of Eq. (4.9) replaced by $T_R^{\text{eff}}|a_1|^2\partial a_1/\partial\tau$ where $T_R^{\text{eff}} \equiv -2i/\beta$. While the correspondence is not exact since the functional dependence is different ($\sim a_1\partial|a_1|^2/\partial\tau$ for Raman-scattering versus $\sim |a_1|^2\partial a_1/\partial\tau$ for the cascaded process), some qualitative understanding can be gained from considering the effective cascaded response with $T_R^{\text{eff}} \sim i/\beta$: First, the cascaded correction is imaginary and hence does not contribute directly to the phase (unlike the Raman response). Rather, it alters the field envelope. The envelope change subsequently couples to the phase profile through the remaining terms of Eq. (4.4), so the frequency shift occurs through a higher-order process. Second, T_R^{eff} saturates with $1/\beta \sim 1/\Delta k(\lambda)$, unlike the Raman response which does not depend strongly on wavelength. This saturation will be explored in greater detail in Section 4.3. Note that the effective response for the cascaded process can be approximately two orders of magnitude or more greater than that of Raman-scattering, so that significant frequency shifting is possible in centimeters of quadratic material (versus meters of fiber with Raman).

For a qualitative understanding of the effect of the GVM term, we decompose the field $a_1(\xi,\tau)$ in Eq. (4.4) into its amplitude and phase with the substitution $a_1(\xi,\tau) = u(\xi,\tau)\exp(i\phi(\xi,\tau))$, where $u(\xi,\tau)$ and $\phi(\xi,\tau)$ are real functions. The evolution of the amplitude and the phase is then given by

$$\frac{\partial u}{\partial \xi} = \delta_1 \frac{\partial u}{\partial \tau}\frac{\partial \phi}{\partial \tau} + \frac{\delta_1}{2} u \frac{\partial^2 \phi}{\partial \tau^2} + \frac{2}{\beta^2} u^2 \frac{\partial u}{\partial \tau}, \tag{4.10}$$

$$u\frac{\partial \phi}{\partial \xi} = -\frac{\delta_1}{2}\frac{\partial^2 u}{\partial \tau^2} + \frac{\delta_1}{2}(\frac{\partial \phi}{\partial \tau})^2 u - \frac{1}{\beta}u^3 + \frac{2}{\beta^2}u^3 \frac{\partial \phi}{\partial \tau}. \tag{4.11}$$

For the sake of simplicity, we concentrate on the nonlinear terms and ignore the dispersion, which amounts to neglecting the terms with higher-order time derivatives. With this simplification, we obtain

$$\frac{\partial u}{\partial \xi} = \frac{2}{\beta^2} u^2 \frac{\partial u}{\partial \tau}, \tag{4.12}$$

$$u\frac{\partial \phi}{\partial \xi} = -\frac{1}{\beta}u^3 + \frac{2}{\beta^2}u^3 \frac{\partial \phi}{\partial \tau}. \tag{4.13}$$

If we assume β is large, $u(\xi, \tau)$ and $\phi(\xi, \tau)$ can be calculated by expanding in powers of $1/\beta$, similar to the procedure used to obtain Eq. (4.4). Keeping terms up to order $1/\beta^2$, Eq. (4.12) shows that $u(\xi, \tau) = u(\tau) + O(1/\beta^2)$, *i.e.*, that the field amplitude is approximately unchanged. Thus, integration of Eq. (4.13) yields

$$\phi(\xi, \tau) = -\frac{1}{\beta}u^2(\tau)\xi + O(\frac{1}{\beta^2}). \tag{4.14}$$

Substitution of this relation back into Eq. (4.13) gives

$$\frac{\partial \phi}{\partial \xi} \approx -\frac{1}{\beta} u^2 - \frac{4}{\beta^3} u^3 \frac{\partial u}{\partial \tau}. \tag{4.15}$$

The first term on the right represents the Kerr-like nonlinear phase shift and the second term corresponds to the noninstantaneous nonlinear response due to large GVM.

The relation in Eq. (4.15) provides a valid description of the phase evolution only in its early stages before the field amplitude is modified significantly, and in the absence of dispersion. Within these approximations, the effect of the GVM on the nonlinear phase shift can be illustrated for a given pulse shape: $a_1(0, \tau) = \mathrm{sech}(\tau)$. Integration of Eq. (4.15) yields

$$\phi(\xi, \tau) \approx -\frac{1}{\beta} \mathrm{sech}^2(\tau)(1 + \xi \frac{2}{\beta^2} \mathrm{sech}(\tau) \tanh(\tau))\xi + \phi_0, \tag{4.16}$$

where ϕ_0 is an integration constant. The temporal asymmetry of the GVM contribution shifts the peak of the nonlinear phase shift.

Likewise, by Fourier transforming to the frequency domain, the contributions of the Kerr-like and the GVM terms in Eq. (4.4) can be calculated for the pulse shape to be

$$\frac{1}{\beta} |a_1|^2 a_1 + 2i \frac{1}{\beta^2} |a_1|^2 \frac{\partial a_1}{\partial \tau} =$$

$$\frac{\sqrt{\pi/2}}{\beta} (1 + \omega^2)(3 + 2\omega/\beta) \mathrm{sech}(\pi\omega/2), \tag{4.17}$$

which has a bipolar shape. Positive frequency components are attenuated and negative frequencies are amplified, or vice versa, depending on the sign of the phase-mismatch-to-GVM ratio. This result is expected to hold in general for any smooth, single-peaked pulse shape for which $a_1(0,\tau) \to 0$ for $|\tau| \to \infty$. Such a frequency shift is expected from the GVM term, which has an odd-order time derivative.

4.3 Numerical analysis

Although the approximate one-field equation [Eq. (4.4)] is useful for a qualitative understanding, it is necessary to consider the coupled equations [Eqs. (4.1) and (4.2)] for a quantitative description. To this end, we numerically solve a version of Eqs. (4.1) and (4.2) that has been generalized to include the self- and cross-phase modulation terms that are due to the cubic nonlinearity. We use a different field normalization here to facilitate comparison with experimental parameters.

$$
\begin{aligned}
& i\frac{\partial A_1}{\partial z} - \frac{Z_I}{2L_{DS,1}}\frac{\partial^2 A_1}{\partial \tau^2} \\
& \quad + A_1^* A_2 \exp(i\Delta k (Z_I z)) \\
& \quad + \frac{Z_I}{L_{NL,1}}(|A_1|^2 + 2|A_2|^2)A_1 = 0, \qquad (4.18) \\
& i\frac{\partial A_2}{\partial z} - \frac{Z_I}{2L_{DS,2}}\frac{\partial^2 A_2}{\partial \tau^2} - i\frac{Z_I}{L_{\mathrm{GVM}}}\frac{\partial A_2}{\partial \tau}
\end{aligned}
$$

$$+\frac{n(\omega_1)}{n(\omega_2)}A_1^2\exp(-i\Delta k(Z_I z))$$

$$+\frac{n(\omega_1)}{n(\omega_2)}\frac{Z_I}{L_{NL,2}}(2|A_1|^2+|A_2|^2)A_2=0. \tag{4.19}$$

Here the FF and SH envelopes (A_1 and A_2, respectively) are in units of the initial peak FF field A_0 (related to the initial peak FF intensity by $I_0=\sqrt{\varepsilon/\mu}|A_0|^2/2$), and n_2 is the Kerr nonlinear index. The cubic nonlinear length characterizing the pulse propagation is $L_{NL,j}=c/\omega_j n_2 I_0$ (the length over which the accumulated nonlinear phase shift is 1) for frequency ω_j with $j=1,2$. The propagation coordinate z is normalized to the quadratic nonlinear length $Z_I=n\lambda_1/2\pi d_{\text{eff}}A_0$ which characterizes the strength of the nonlinear coupling. Variable d_{eff} is the effective quadratic nonlinear coefficient. Time τ, $L_{DS,j}$, and L_{GVM} are defined as for Eqs. (4.1) and (4.2).

Eqs. (4.18) and (4.19) are solved using a symmetric split-step beam propagation method [18]. The simulations assume typical conditions for femtosecond pulses in quadratic nonlinear crystals. As an example, we calculate the propagation of 120-fs pulses with a peak intensity of 50 GW/cm^2 in a 10 cm-long quadratic medium. The launched pulse shape is chosen to be Gaussian with center wavelength 790 nm. The quadratic medium used is barium metaborate (Ba_2BO_4 or BBO), for which the material parameters are n = 1.63, d_{eff} = 1.82 pm/V, $n_2=3.2\times10^{-16}$ cm^2/W, GVM = -186 fs/mm, the FF (SH) GVD = 70 (190) fs^2/mm, and the FF (SH) third-order dispersion 50 (81) fs^3/mm. Note that the true cubic nonlinearity (n_2) is included in the calculations. Two-photon absorption is neglected since it is small for BBO at 790 nm. The phase mismatch is set to be $\Delta k=5\pi$/mm, corresponding

to a self-defocusing nonlinearity and a magnitude that is about half the minimum value to obtain a Kerr-like phase shift. This particular set of conditions, except for the crystal length, is chosen to correspond to experiments that are described below. As expected, the spectrum of the pulse shifts to higher frequencies as it propagates through the quadratic medium. The evolution of the spectrum is shown in Fig. 4.2(a). Initially, the frequency-shift increases linearly with propagation distance, but eventually the process saturates [Fig. 4.2(b)]. The spectrum of the SH field shifts opposite from that of the FF (*i.e.*, to lower frequencies), prior to saturation. This saturation is expected, since the effective response of the cascaded process decreases (or is distorted) with increasing frequency shift. For this choice of pulse parameters and phase-mismatch, the saturation begins beyond 3 cm, which is close to the maximum length of available BBO crystals. The cubic electronic nonlinearity of the quadratic material is included here for complete correspondence with experimental parameters, however the close agreement in Fig. 4.2(b) between the saturation trend with and without n_2 indicates the dominance of the quadratic process in the frequency shifting dynamics. In Fig. 4.2(b), the presence of cubic nonlinearity slightly reduces the resulting frequency shift, as expected as a result of its self-focusing phase. One might expect the material's Raman response to be relevant to the frequency-shifting dynamics studied here, however the Raman response of BBO with ∼100-fs pulses is small compared with the cascaded response. In comparison to Raman, the cubic electronic nonlinearity included in Fig. 4.2(b) is a larger effect, even though it alters the frequency shifting process indirectly through the nonlinear phase.

The pulse propagation is dominated by an interplay of GVD and the effective nonlinearity from the cascaded process in the form of solitonlike dynamics. In

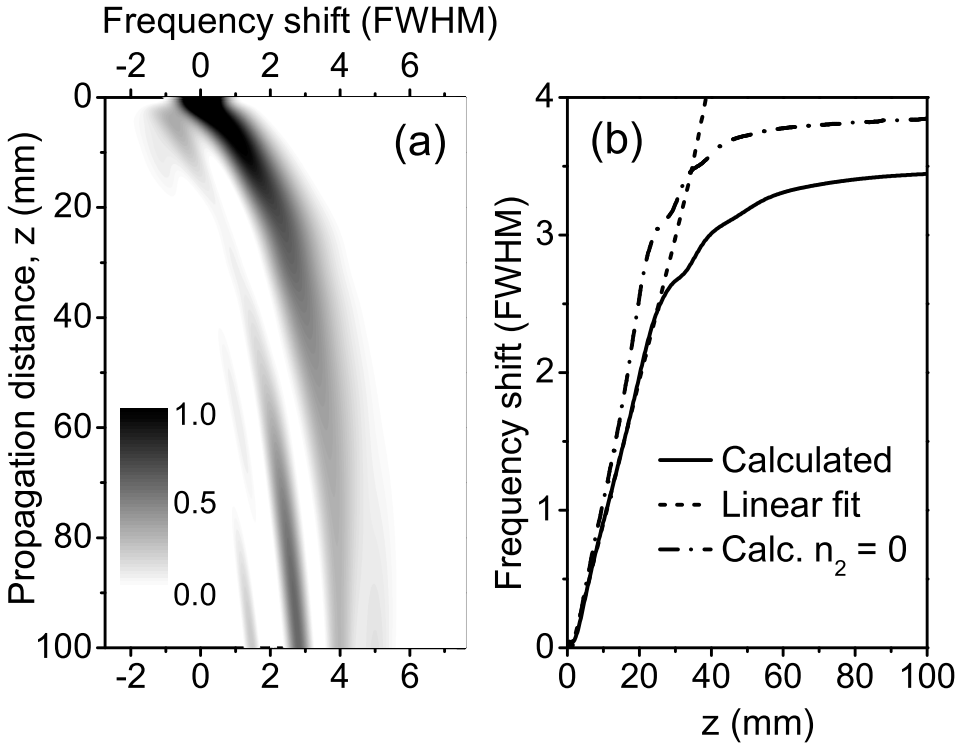

Figure 4.2: (a) Evolution of the spectrum along the propagation direction. Shift is in units of the initial spectral FWHM, ~ 3.7 THz. The scale bar shows spectral intensity in arbitrary units. (b) Weighted average frequency shift as a function of propagation distance. The dashed curve indicates a fit to the region of linear shift. The dashed-dotted curve shows similar results in the absence of $\chi^{(3)}$ ($n_2 = 0$).

the time domain, the pulse undergoes compression since the energy is more than the amount needed to balance the dispersive effects. The intensity profiles before the onset of saturation and at the exit face of the crystal are plotted in Fig. 4.3 along with those of the launched pulse. The FF undergoes a steady compression accompanied by energy loss to the SH: At $z = 12$ mm, its FWHM is 110 fs with 64% of the pulse energy remaining in the FF. With propagation, the pulse shape becomes slightly asymmetrical. The asymmetrical structure develops into a secondary pulse in the final stages of propagation that corresponds to the secondary structure of the spectrum [Fig. 4.2(a)]. At $z = 100$ mm, the FWHM of the main peak is reduced to 40 fs while $\sim$ 36% of the launched energy is retained in the FF. The temporal profiles are displaced since the pulse experiences different group velocities as its central frequency changes.

A similar picture emerges for the total frequency shift for fixed propagation distance and varying phase mismatch. The magnitude of the nonlinear phase, and hence the frequency shift, is proportional to $1/\Delta k$ before it saturates. Loss to SH conversion increases with decreasing $|\Delta k|$, so there exists a trade-off between the magnitude of the frequency shift and loss. We define a figure-of-merit (FOM) for the shifting process as the ratio of frequency-shift to energy content in the SH field, which attains a maximum for phase mismatch values slightly below those of the minimum for obtaining Kerr-like nonlinear phase shifts (Fig. 4.4). This is demonstrated in Fig. 4.4, which shows simulations of 100-fs, 200-pJ pulses with center wavelength 1550 nm (and peak intensity $\sim$ 5 GW/cm^2). The material parameters used correspond to those of the quadratic material periodically poled lithium niobate (PPLN): n = 2.14, $d_{\text{eff}} = 16.5$ pm/V, $n_2 = 3.2 \times 10^{-15}$ cm^2/W, GVM = -370 fs/mm, and the FF (SH) GVD = 100 (400) fs^2/mm. Under these conditions,

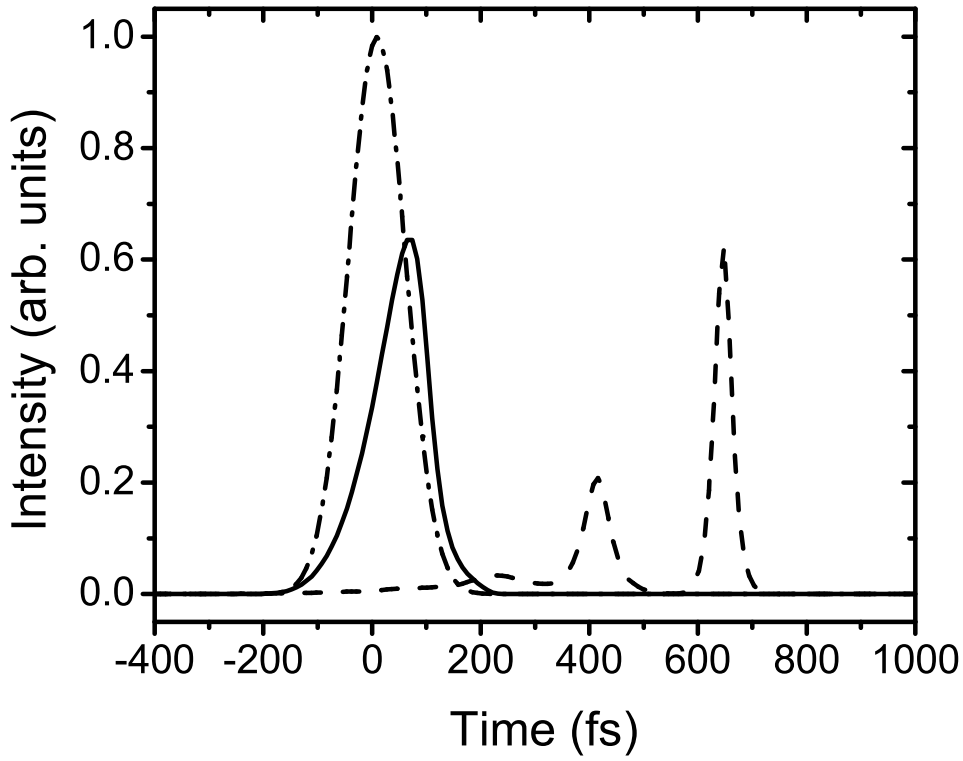

Figure 4.3: Intensity profiles of the FF at $z = 0$ mm (dashed-dotted curve), $z = 12$ mm (solid curve), $z = 100$ mm (dashed-curve). For the launched pulse $L_{\mathrm{DS},1} = 74$ mm.

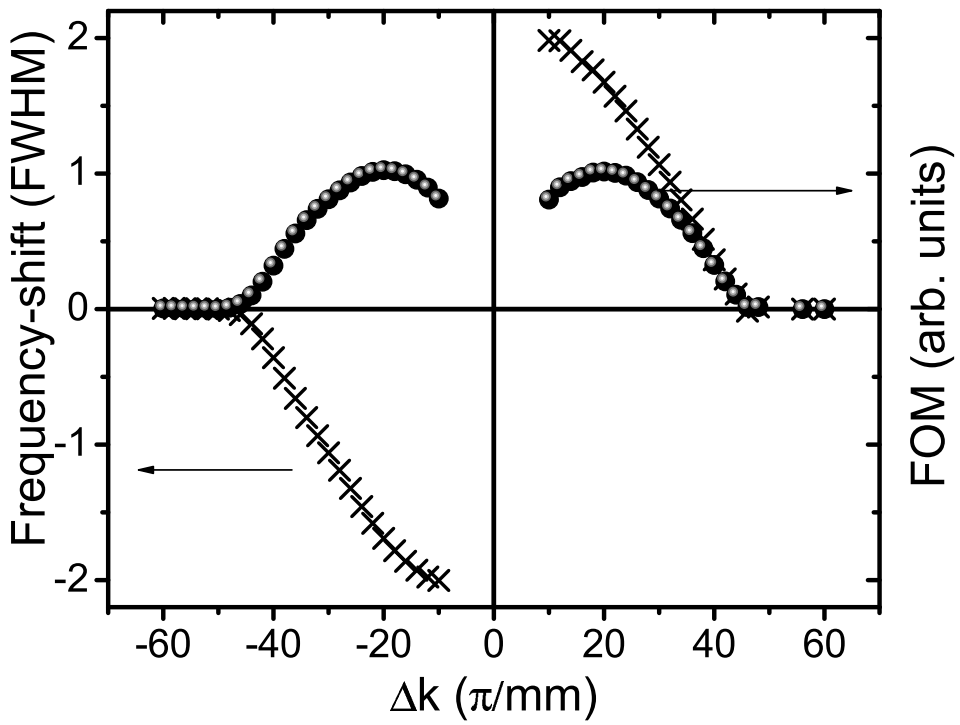

Figure 4.4: Frequency shift (crosses) and figure-of-merit (circles) as a function of phase mismatch. Similarly to Fig. 4.2, frequency shift is measured in units of the initial FWHM (here $\sim$ 4.4 THz). Note that GVD is chosen to be normal (anomalous) for $\Delta k > 0$ ($\Delta k < 0$) to support solitonlike pulses.

the stationary boundary for Kerr-like phase shifts corresponds to $|\Delta k| \gtrsim 25\pi$/mm. Notice that much larger frequency shifts can be generated closer to phase matching, but with larger SH conversion.

The noninstantaneous nature of the cascaded quadratic process with significant walk-off between the FF and the SH is demonstrated by the nonlinear phase shift imposed on the FF. Simulations confirm the aforementioned expectations: Effectively retarded or advanced phase shifts are imposed on the FF depending on the sign of the GVM (Fig. 4.5).

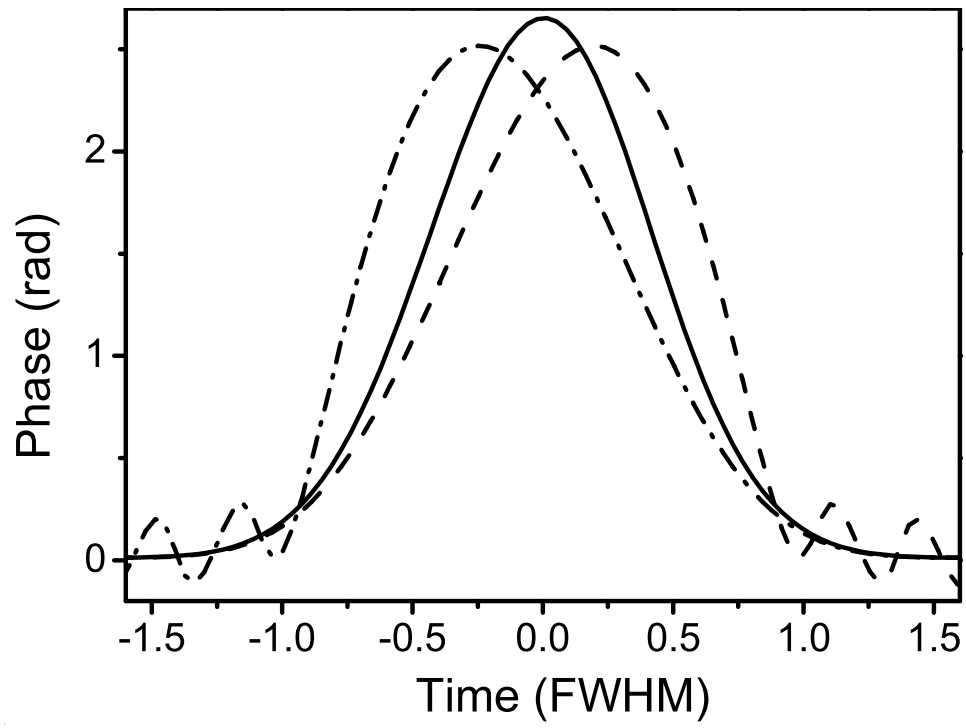

Figure 4.5: Phase impressed on the FF for zero (solid curve), positive (dashed curve), and negative (dashed-dotted curve) GVM.

4.4 Experimental observation of the frequency shift

Experiments were performed with 120-fs, 0.6-mJ pulses centered at 790 nm and generated by a Ti:sapphire regenerative amplifier. The launched pulse shape was approximately Gaussian with a clean spatial profile and the peak intensity was estimated to be 50 GW/cm^2. A 17 mm-long piece of BBO served as the quadratic medium. The GVM length was $L_{\mathrm{GVM}} = 0.38$ mm, for which the criterion for a Kerr-like phase shift implies $\Delta k > 10.4\pi$/mm. Both blue and redshifts are experimentally available through positive and negative phase mismatch, respectively. However, redshifts occur with self-focusing nonlinearity, which limits the peak intensity available without continuum generation and crystal damage. Consequently, we focus here on blue-shifts.

Increasing frequency shift of the FF was observed with decreasing phase mismatch (Fig. 4.6). The inset of Fig. 4.6 shows the spectral shift versus phase mismatch for self-defocusing phase shifts, and the main figure shows example spectra. The data presented for $\Delta k = 36\pi$/mm serve as a control experiment: At such a large phase mismatch, the cascade nonlinear phase and the Kerr nonlinearity are negligible and the spectrum is indistinguishable from the spectrum of the launched pulses (not shown). The temporal profile of the pulse did not change significantly in these experiments. The experimental results are compared with the results of numerical simulations which contained no free parameters and were based on experimental conditions. In Fig. 4.6, the calculated spectrum of the unshifted pulse (36π/mm) is normalized so that it contains the same power as the measured unshifted spectrum and all other traces have the same relative scaling, so that the units of all the given spectra are the same. With this in mind, there is excellent agreement between the measured spectra and the simulations. In particular, the

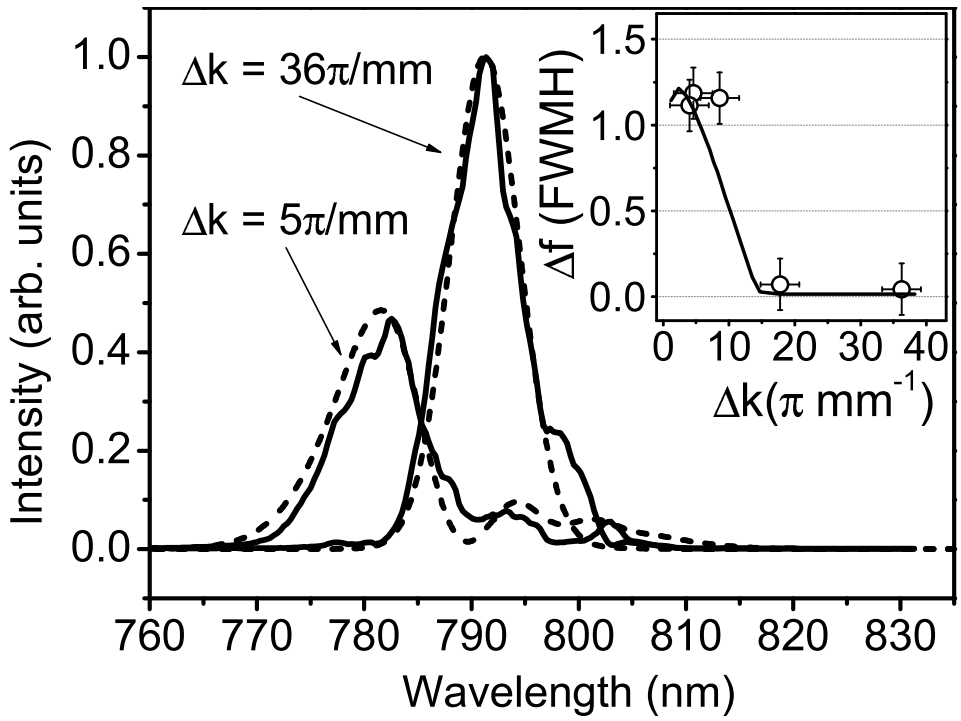

Figure 4.6: Experimental (solid curves) and simulated (dashed curves) spectra for phase mismatches of 5π/mm and 36π/mm. The latter serves as control. Inset: experimental (symbols) and calculated (solid curve) frequency shift for different values of phase mismatch. As in Fig. 4.2, frequency shift is measured in units of the initial FWHM, ~ 3.7 THz.

shift increases greatly from $\Delta k = 19\pi$/mm to $\Delta k = 5\pi$/mm. The latter is the phase mismatch for which the ratio of the spectral shift to SH conversion should peak. The dependence of the frequency shift on the phase mismatch, as summarized by the inset of Fig. 4.6, agrees qualitatively with the results of Fig. 4.4; however, the phase mismatch corresponding to maximum ratio of spectral-shift to SH conversion is different from that in Fig. 4.4 as a consequence of different physical parameters in the experiment.

4.5 Applications

We have shown that cascaded quadratic processes under phase mismatch conditions and in the presence of significant GVM (typical conditions with femtosecond-duration pulses) result in an effectively noninstantaneous cubic nonlinearity. The response time is controllable by appropriate choice of the phase mismatch. In addition to providing an intuitive picture for the effect of phase mismatch on the propagation of femtosecond pulses, this nonlinear process offers some unique features. The nonlocal nature of the Raman-like cascade nonlinearity is interesting in its own right. Nonlocality of the cubic nonlinearity has been shown to arrest self-focusing collapse and to stabilize solitons, for example [19, 20]. The nonlocal nature of the cascade process under nonstationary conditions can be controlled or tailored to specific situations through the phase mismatch.

Many applications of a controllablem effective Raman process can be envisioned. Perhaps the most obvious one is the cancellation of the Raman shift that a short pulse accumulates as it propagates in optical fiber. For example, in telecommunication systems with bit rates above ~ 20 Gbit/s, the pulse duration is short enough that timing jitter is dominated by jitter arising from Raman-induced frequency shifts [21].

In high-energy short-pulse fiber amplifiers, the nonlinear phase shift can be controlled reasonably well by the technique of chirped-pulse amplification, and as a result an equally important limitation to pulse energy is stimulated Raman scattering [22]. The redshifts produced by Raman scattering can be compensated for by blueshifting the pulses prior to, or following, propagation in fiber. As an example, we calculate the precompensation of the Raman-induced redshift of a 100-fs, transform-limited pulse centered at 1550 nm in standard single-mode fiber

(modal area of 80 μm^2 and GVD of -23 ps^2/km). The pulse energy is 1 nJ. The quadratic medium is a 4-cm-long waveguide written in PPLN. The modal area of the waveguide is 40 μm^2 and the GVD for the FF is 100 ps^2/km [23]. The phase mismatch is set to $\Delta k = 20\pi$/mm. The pulse is first blueshifted in the PPLN waveguide and then propagates in the fiber. These calculations indicate that the central wavelength can be kept at 1550 nm, following propagation in up to 50 cm of fiber. If no precompensation is utilized, the pulse is redshifted to 1800 nm (Fig. 4.7). This result nicely complements the previously established conclusion that the cascade nonlinearity can be used to compensate the nonlinear phase shift produced by the electronic Kerr nonlinearity under similar conditions [24].

Other potential applications include devices that convert peak power to frequency-shift, which can be used to switch wavelength channels or intensity discrimination with the addition of a frequency filter [25].

We consider the application to pulse compression in some detail. For pulse energies in excess of 1 mJ, methods based on cubic nonlinearity for the generation of extra bandwidth cannot be used because of the limitations of excessive nonlinearity in single-mode waveguides and material damage through self-focusing for unguided geometries. Self-defocusing nonlinearities in quadratic media address these difficulties [6, 26]. The generalization of this approach to include frequency shifts as described here enables us to implement an analog of Raman-soliton compression [27]: High-order solitons are formed, producing a compressed primary pulse that undergoes a continuous self-frequency shift. An advantage of this approach is that the pedestal commonly produced by Raman-soliton compression consists mainly of unshifted frequency components. These components can be eliminated with a frequency filter to yield a pedestal-free pulse.

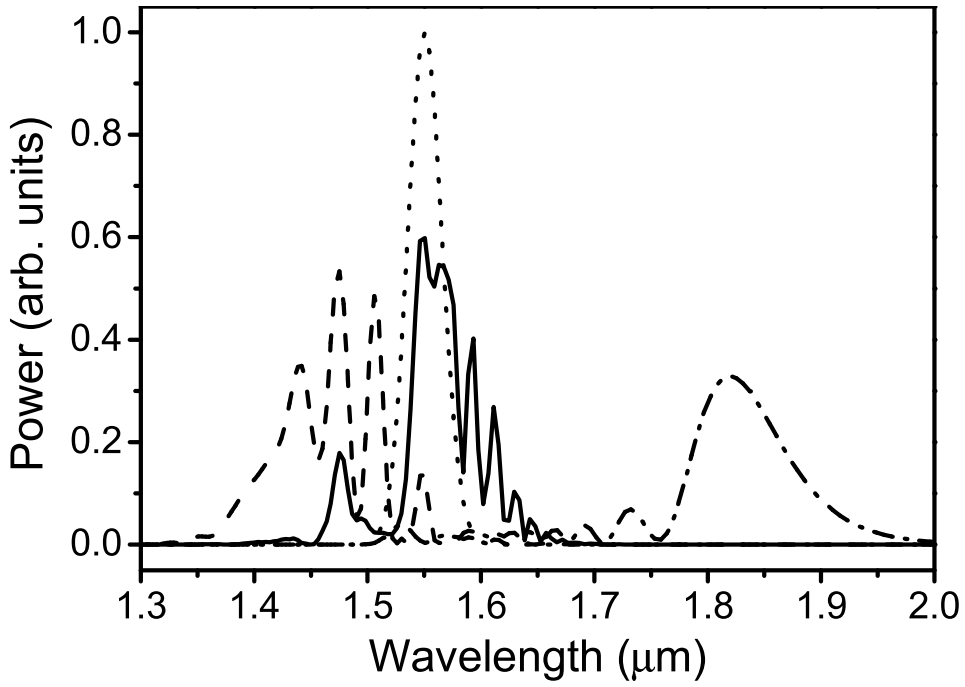

Figure 4.7: Pulse spectrum after propagation in fiber without pre-compensation (dash-dotted curve) and after cascade precompensation stage (dashed curve) and subsequent propagation through fiber (solid curve). Dots indicate the launched pulse spectrum.

Numerical simulations for realistic parameters demonstrate the utility of this approach: 100-fs, 0.6-nJ pulses with $\Delta k = 50\pi/\text{mm}$ compress to 20-fs upon propagation through a 6 cm-long waveguide in PPLN (Fig. 4.8). The pulse quality (Q_c), defined as the ratio of energy contained within the FWHM of the pulse to that of the initial pulse, is calculated to be 0.65. The unshifted components can be filtered out to produce a longer (38 fs) but much cleaner $Q_c = 0.91$ pulse. Compression in a second 2.5-cm-long PPLN crystal generates a 15 fs pulse with virtually no additional degradation in pulse quality ($Q_c = 0.90$). The resulting pulse after two stages of compression contains $\sim$50% of the launched pulse energy. Similarly, calculations indicate that compression factors of up to 3 should be attainable with 1-mJ pulses in a bulk BBO crystal at 800 nm, and experiments are underway to verify this compression. In addition to the high pulse quality, a practical advantage of this approach is that larger nonlinear phase shifts can be produced at the smaller phase mismatches needed in comparison with compression in quadratic media under nearly stationary conditions.

4.6 Conclusion

In summary, we have demonstrated a new capability of cascaded quadratic processes under phase mismatched conditions: Effectively retarded or advanced nonlinear phase shifts can be impressed on a pulse in the presence of significant GVM between the FF and SH frequencies. The frequency-domain manifestation of this noninstantaneous nonlinear response is redshifts or blueshifts of the pulse spectrum. The direction and the magnitude of the frequency shift is controllable by the choice of the phase mismatch. Just as effectively instantaneous phase shifts from cascaded processes are analogous to bounded-electronic ($\chi^{(3)}$) nonlinearities

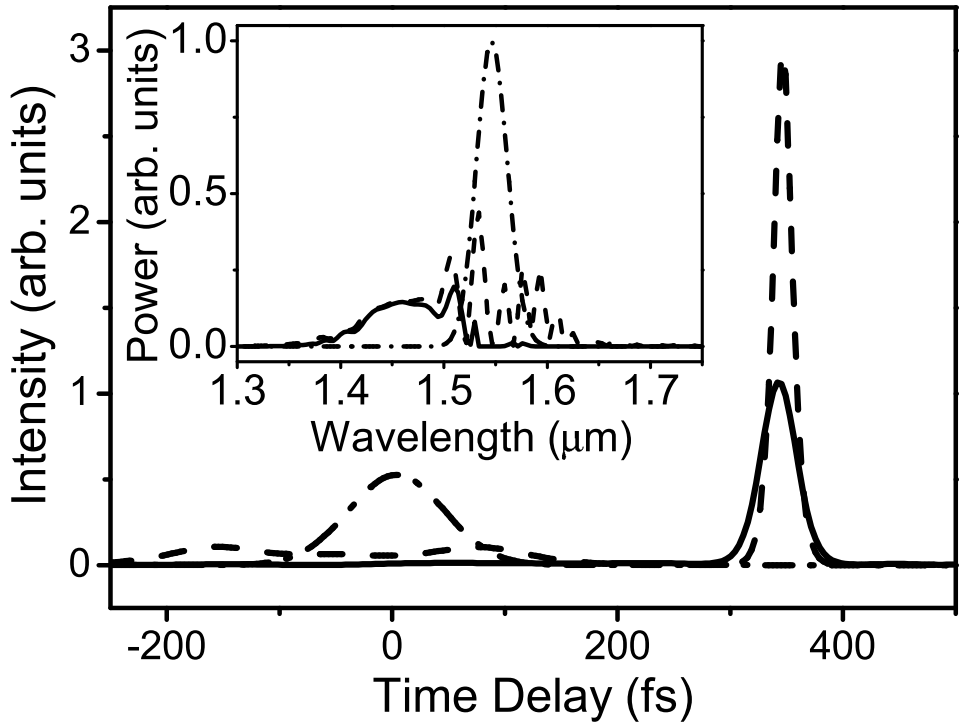

Figure 4.8: Temporal profile of compressed pulses before (dashed curve) and after spectral filtering (solid curve) of the unshifted frequencies. Inset: compressed pulse spectrum before (dashed curve) and after filtering (solid curve). Dash-dotted curves indicate the launched temporal profile and spectrum.

for negligible GVM, these noninstantaneous phase shifts in the presence of strong GVM are analogous to nuclear (Raman-induced) nonlinearities.

We expect the unique features of these processes to find many applications. Here, we numerically demonstrated compensation of Raman-induced frequency shifts and high-quality pulse compression assuming typical conditions for femtosecond pulses in common quadratic nonlinear media. More generally, however, spectral shifts from cascaded quadratic processes should be applicable to all processes involving Raman-induced frequency shifts, but with the added freedom of sign and magnitude control.

4.7 Acknowledgments

This work was supported by the National Science Foundation under grants PHY-0099564 and ECS-0217958, and by the National Institutes of Health under grant EB002019. We acknowledge valuable discussions with B. A. Malomed and L. Torner, and we thank E. Kavousanaki for help with the numerical simulations.

BIBLIOGRAPHY

[1] F. Ö. Ilday, K. Beckwitt, Y.-F. Chen, H. Lim, F. W. Wise, J. Opt. Soc. Am. B **21**, 376 (2004).

[2] G. I. Stegeman, R. Schiek, L. Torner, W. Torruellas, Y. Baek, D. Baboiu, Z. Wang, E. Van Stryland, D. J. Hagan, and G. Assanto, "Cascading: A Promising Approach to Nonlinear Optical Phenomena," in *Novel Optical Materials and Applications*, I.C. Khoo, F. Simoni, and C. Umeton ed. (John Wiley & Sons, New York, 1997), Ch. 2, pp.49-76.

[3] C. R. Menyuk, R. Schiek, and L. Torner, J. Opt. Soc. Am. B **11**, 2434 (1994).

[4] A. Kobyakov, E. Schmidt, and F. Lederer, J. Opt. Soc. Am. B **14**, 3242 (1997).

[5] H. J. Bakker, P. C. M. Planken, L. Kuipers, and A. Lagendijk, Phys. Rev. A **42**, 4085 (1990).

[6] X. Liu, L. J. Qian, and F. W. Wise, Opt. Lett. **24**, 1777 (1999).

[7] F. Wise, L. Qian, and X. Liu, J. Nonlinear Opt. Phys. & Mat. **11**, 317 (2002).

[8] S. Carrasco, J. P. Torres, L. Torner, and F. W. Wise, Opt. Commun. **191**, 363 (2001).

[9] L. J. Qian, X. Liu, and F. W. Wise, Opt. Lett. **24**, 166 (1999).

[10] K. Beckwitt, F. W. Wise, L. Qian, L. A. Walker, and E. Canto-Said, Opt. Lett. **26**, 1696 (2001).

[11] P. Di Trapani, W. Chinaglia, S. Minardi, A. Piskarskas, and G. Valiulis, Phys. Rev. Lett. **84**, 3843 (2000).

[12] P. Pioger, V. Couderc, L. Lefort, A. Barthelemy, F. Baronio, C. De Angelis, Y. Min, V. Quiring, W. Sohler, Opt. Lett. **27**, 2182 (2002).

[13] A. A. Kanashov and A. M. Rubenchik, Physica D **4**, 122 (1981).

[14] J. P. Torres and L. Torner, Opt. Quant. Electron. **29**, 757 (1997).

[15] H. H. Chen, Y. C. Lee, and C. S. Liu, Phys. Scr. **20**, 490 (1979).

[16] A. Kundu, J. Math. Phys. **25**, 3433 (1984).

[17] G. P. Agrawal. *Nonlinear Fiber Optics* (Academic Press, San Diego, 1995).

[18] X. Liu, K. Beckwitt, and F. W. Wise, Phys. Rev. E **62**, 1328 (2000).

[19] O. Bang, W. Krolikowski, J. Wyller, and J. Rasmussen, Phys. Rev. E **66**, 046619 (2002).

[20] W. Krlikowski, O. Bang, J. Wyller, and J. J. Rasmussen, Acta Phys. Pol. A **103**, 133 (2003).

[21] P. T. Dinda, K. Nakkeean, and A. Labruyere, Opt. Lett. **27**, 382 (2002).

[22] A. Galvanauskas, J. Sel. Top. Quan. Elec. **7**, 504 (2001).

[23] M.M. Fejer, G.A. Magel, D.H. Jundt, and R.L. Byer, IEEE J. Quantum Electron. **28**, 2631 (1992).

[24] F. Ö. Ilday and F. W. Wise, J. Opt. Soc. Am. B **19**, 470 (2002), and references therein.

[25] C. Xu and X. Liu, Opt. Lett. **28**, 986 (2003).

[26] S. Ashihara, J. Nishina, T. Shimura, and K. Kuroda, J. Opt. Soc. Am. B **19**, 2505 (2002).

[27] P. Beaud, W. Hodel, B. Zysset, and H. P. Weber, IEEE. J. Quantum Electron. **QE-23**, 1938 (1987).

Chapter 5

Frequency shifting with local nonlinearity management in nonuniformly poled quadratic nonlinear materials[1]

We show theoretically that the frequency shifts which result from phase-mismatched cascaded processes under conditions of strong group-velocity mismatch can be significantly enhanced by local control of the nonlinearity with propagation. This control is possible with continuous variation of the poling period of quasi-phase matched structures, and can allow one to avoid saturation of the frequency shift. We theoretically demonstrate its applicability to high-quality, efficient frequency shifting of infrared pulses.

5.1 Introduction

In recent years, the nonlinear phase shifts which result from cascaded interactions in quadratic ($\chi^{(2)}$) nonlinear media have received much attention as a route to large nonlinear phase-shifts of controllable magnitude and sign [2]. In particular, they have been shown to support the generation of solitons [3], compensate for Kerr phase shifts [4], and prove useful for applications such as modelocking of short-pulse lasers, pulse compression [5], and nonlinearity management for high pulse energies from fiber lasers [6].

[1]The results presented in this chapter have been published in Ref. [1].

However, to date, applications of cascaded quadratic phase shifts to femtosecond pulses have been in the stationary limit, where the fundamental (FF) and second-harmonic (SH) fields overlap temporally despite group-velocity mismatch (GVM) between them, producing an effective Kerr nonlinearity in the limit of large phase-mismatch [7]: *i.e.*, providing a surrogate for the bound-electronic cubic ($\chi^{(3)}$) nonlinearity.

Recently *non-stationary* cascaded phase shifts were demonstrated [8]. GVM retards or advances (depending on its sign) the SH propagation with respect to the FF. Consequently, the resulting nonlinear phase shift imparted on the FF is advanced or delayed with respect to the stationary phase by an amount depending on the ratio of GVM to phase-mismatch. This non-instantaneous nonlinear response manifests spectrally as redshifts or blueshifts of the pulse spectrum, which produces an analog of nuclear (Raman) nonlinearities from the quadratic process [8].

In this Letter we propose a significant new degree of freedom for non-stationary cascaded frequency shifts: enhancement and control through local nonlinearity management in quasi phase-matched (QPM) quadratic structures. Local nonlinearity control is achieved by aperiodically varying the QPM domain reversal period (to be discussed further). This added level of control greatly increases the applications of cascaded frequency shifts to frequency shifting processes in the infrared.

5.2 Analytical results

We begin by reviewing the origin of cascaded frequency shifts [8]. Within the slowly varying envelope approximation, the coupled equations governing the interaction of the FF (a_1) and SH (a_2) field envelopes propagating in the z direction in a

medium with quadratic nonlinearity under conditions of type I second-harmonic generation (SHG) are [9]

$$i\frac{\partial a_1}{\partial \xi} - \frac{\delta_1}{2}\frac{\partial^2 a_1}{\partial \tau^2} + a_1^* a_2 \exp(i\beta\xi) = 0, \tag{5.1}$$

$$i\frac{\partial a_2}{\partial \xi} - \frac{\delta_2}{2}\frac{\partial^2 a_2}{\partial \tau^2} - i\frac{\partial a_2}{\partial \tau} + a_1^2 \exp(-i\beta\xi) = 0. \tag{5.2}$$

Here, time is normalized to the initial pulse duration, $\tau = t/\tau_0$, the propagation coordinate is $\xi = z/L_{\mathrm{GVM}}$, and $\delta_j = L_{\mathrm{GVM}}/L_{DS,j}$ with dispersion lengths $L_{DS,j} = {\tau_0}^2/\mathrm{GVD}(\omega_j)$ (where GVD is the grou-velocity dispersion). $\beta = \Delta k L_{\mathrm{GVM}}$ for $\Delta k = k_{2\omega} - 2k_\omega$ (the FF-SH wave-vector mismatch) and $L_{\mathrm{GVM}} = \tau_0/(n_{1,g} - n_{2,g})$ for material group velocity index $n_{j,g}$ with $j = 1, 2$.

In Refs. [8] and [10] it was shown that reducing Eqs. (5.1) and (5.2) to a single field equation for the FF through expansion in powers of $1/\beta$ and keeping the lowest order correction from GVM yields

$$\underbrace{i\frac{\partial a_1}{\partial \xi} - \frac{\delta_1}{2}\frac{\partial^2 a_1}{\partial \tau^2} - \frac{1}{\beta}[|a_1|^2 a_1}_{\text{NLSE}} + \underbrace{2i\frac{1}{\beta}|a_1|^2\frac{\partial a_1}{\partial \tau}}_{\text{Correction}}] = 0, \tag{5.3}$$

which consists of two parts: a standard nonlinear Schrödinger equation (NLSE), and the next higher order correction which is responsible for the non-instantaneous phase shift which results from GVM in the non-stationary limit. In Ref. [8] it is shown that the correction qualitatively acts similarly to a Raman-scattering term (of the form [11] $[T_R\, a_1\, \partial|a_1|^2/\partial\tau]$). In analogy to the Raman-scattering response time T_R, we define an effective response $T_R^{\mathrm{eff}} \sim i/\beta$ for the cascaded process.

This effective cascaded response has two effects: first, it is imaginary (unlike the Raman response) so it alters the field envelope instead of contributing directly to the phase. The envelope change couples to the phase profile through the remaining terms of Eq. (5.3), generating a Raman like frequency shift through a higher order process. Second, the frequency shifting saturates with $1/\beta \sim 1/\Delta k(\lambda)$: as the pulse's frequency shifts, Δk changes, eventually saturating the shift. In bulk materials with birefringent phase matching, where the dependence of Δk on λ is fixed, this saturation is unavoidable, and limits the maximum achievable frequency shift.

Consider instead QPM materials in which phase matching is achieved through periodic reversal of the nonlinear tensor element along the direction of propagation. This allows precise control of Δk, through control of the local nonlinear domain reversal period Λ. To date researchers have used QPM structures with constant Λ to achieve highly efficient SHG in the visible and infrared frequencies [12] and structures with varying $\Lambda(z)$ (so-called *chirped* structures) to control the effects of dispersion in quadratic materials [13], resulting in compressed SHG output. In these works the effects of grating chirp have been utilized for *linear* effects in propagation and in the context of phase-matched SHG.

We propose the use of continuously chirped QPM structures for phase-mismatched SHG as a way to alter the effective *nonlinearity* experienced by the pulse as it propagates. This can be achieved with z-dependent Λ, designed to control the effective Δk between the FF and SH, and hence the local nonlinearity. Nonlinearity control is a new degree of freedom in the design and optimization of nonlinear processes in quadratic materials and has been considered for switching applications [14] and soliton formation [15, 16]. Here we show that continuous nonlinearity control with

chirped QPM gratings, combined with the effective Raman-like response described above, allows highly accurate optimization and control of cascaded frequency shifts. In QPM, the net phase-mismatch is given by $\Delta k_{\rm net}(\lambda, z) = \Delta k_{\rm mat}(\lambda) - 2\pi/\Lambda(z)$, where $\Delta k_{\rm mat}$ is the wavelength-dependent material phase-mismatch. Hence, a pulse propagating in a structure with $\Lambda(z)$ designed to keep $\Delta k_{\rm net}$ constant with shifting FF wavelength will experience continued frequency shift (analogous to real Raman-frequency shift), avoiding saturation from the cascaded process.

5.3 Numerical results

Simulations of 100-fs, 0.6-μJ (15 GW/cm^2) pulses at 1550 nm propagating in chirped periodically poled lithium niobate (C-PPLN, $d_{\rm eff} \simeq 30$ pm/V; see Ref. [17]), with and without chirp to optimize the nonlinear frequency shift appear in Fig. 5.1. Eqs. (5.1) and (5.2) are solved numerically with a symmetric split-step beam propagation method [4]. Λ is assumed to vary linearly: *i.e.*, linearly chirped QPM is assumed.

Fig. 5.1 shows enhanced effective Raman shifts with period chirping. The resulting fields, which undergo continued shift with chirped poling, are the qualitative analog of Raman solitons. These cascaded Raman-like solitons provide a means of self-frequency shifting fixed frequency sources by many times their bandwidth. Additionally, the process provides a way to shift to *lower* wavelengths (*i.e.*, the analog of anti-Stokes Raman shifts). High spectral and temporal quality can be achieved by removing the unwanted frequencies with an edge filter. Fig. 5.2 shows a 100-fs, 0.12-μJ (15 GW/cm^2) pulse at 1550 nm shifted by >200 nm in a C-PPLN structure (from $\Lambda = 38$ μm to 22 μm) with output quality factor 0.96 (Q, the ratio of energy within the full-width at half-maximum of the pulse to that of the ini-

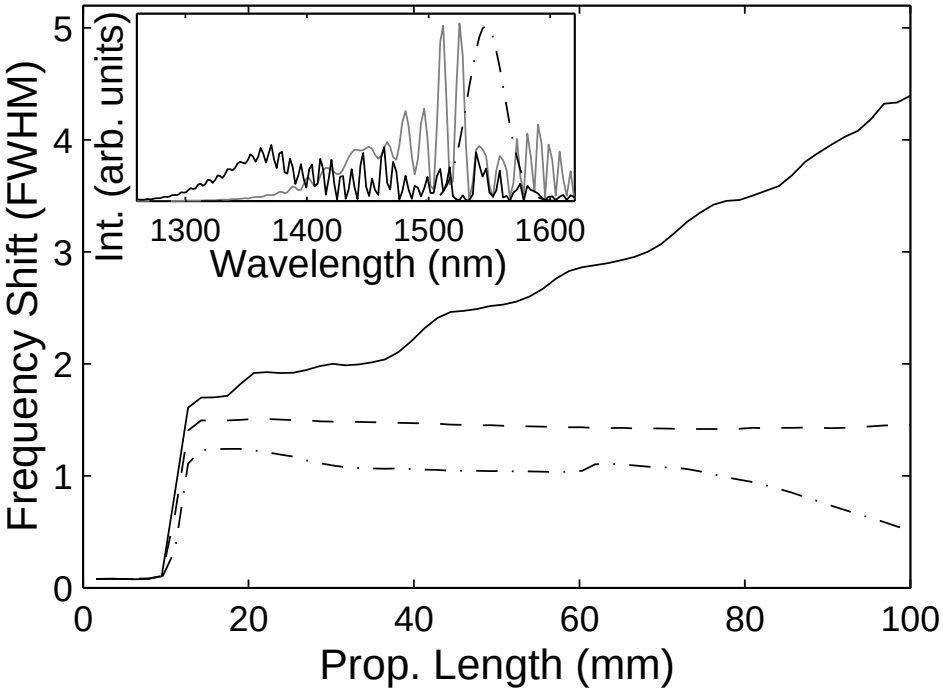

Figure 5.1: Average spectral shift (in units of the initial FWHM, ∼4.4 THz) with propagation. The dashed curve shows the linear shift followed by saturation with constant Λ. The solid (dash-dotted) curve shows shift with chirped structure to optimize (hinder) the spectral shift. Inset, input spectrum (rescaled, dash-dotted curve) and shifted spectra with (black) and without (grey) period chirp.

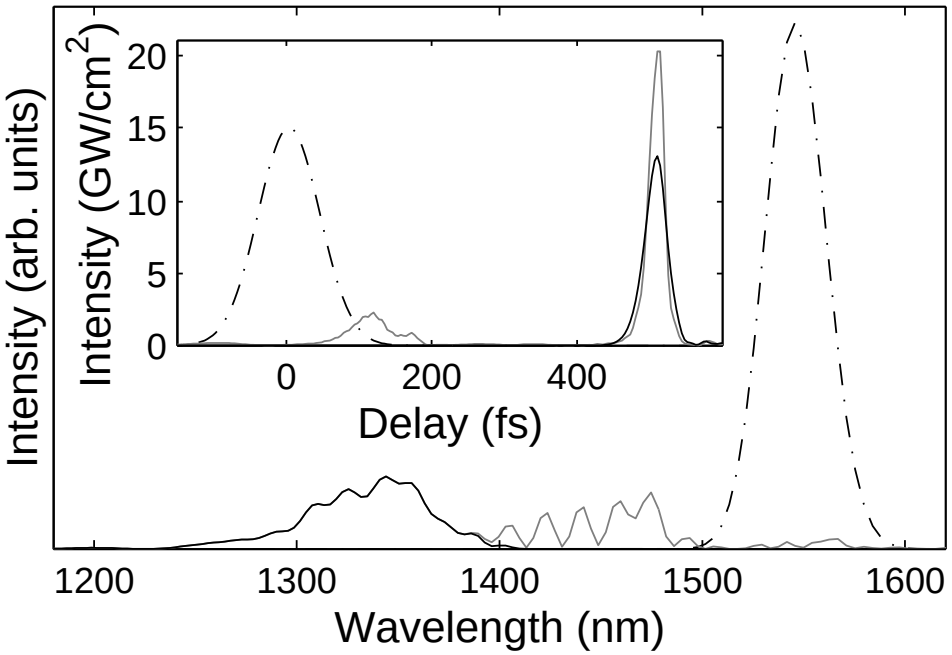

Figure 5.2: Spectra and (inset) temporal profile of input pulse (dash-dotted) and shifted pulse before (grey curve) and after (black curve) filtering. Filtering reduces the output pulse energy from 48% to 33% of that launched, but yields a pulse with Q = 0.96. C-PPLN sample length is 4.6 cm.

tial pulse). As with ordinary Raman solitons, the cascaded soliton is temporally compressed, so its peak power is similar to that of the launched pulse.

This processes should be applicable to other wavelengths in the infrared, in particular, the technologically important 1030-1060 nm band where high energy sources exist. The only practical limits are that the wavelength must be suitable for material poling, and the material parameters must support the shifting process (*i.e.* with short pulses, the sign of GVD determines the direction of shift, and the GVM cannot be too large). The ability to generate large and efficient frequency shifts with clean pulse output is of great interest, since it presents an al-

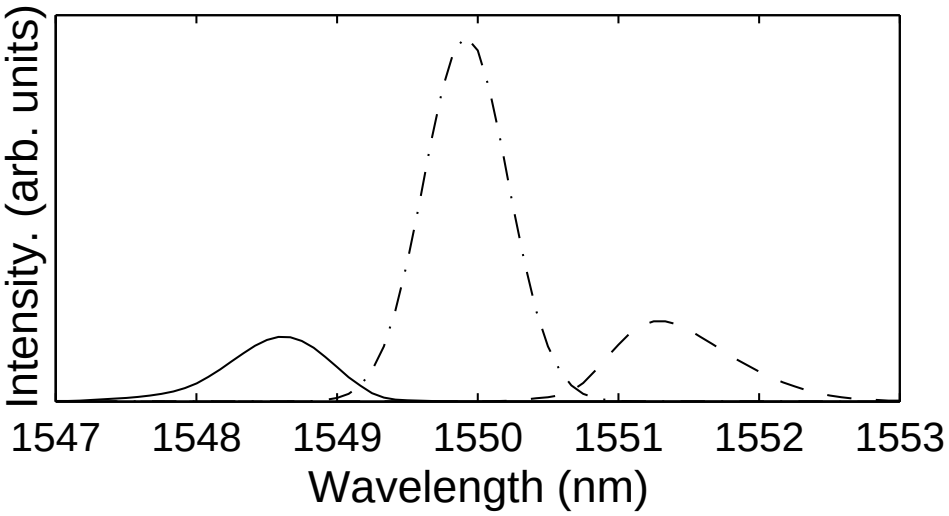

Figure 5.3: Frequency shift of 5 ps, 50 pJ pulses in waveguided C-PPLN. Dash-dots show the input spectrum. The solid (dashed) line shows down- (up-) shift with grating chirp 18.425 μm to 18.405 μm (18.36 μm to 18.38 μm), after filtering out the unshifted frequency components. Waveguide dimensions are 3 μm by 7 μm.

ternative to common optical frequency conversion schemes like optical parametric amplification, but in a more compact and simple implementation.

For C-PPLN in the infrared, the sign of GVD is normal, preventing shifts to longer wavelengths with short pulses ($<\sim$picoseconds). However, with longer pulses (so dispersion is negligible) this restriction is lifted. This applies to high bit rate telecommunications applications, where the small modal area (and resulting high effective nonlinearity) available in waveguided PPLN can be used to generate frequency shifts useful for wavelength-devision multiplexing (WDM) applications. Fig. 5.3 shows shifting of 5 ps, 50 pJ pulses at 1550 nm in C-PPLN optimized for $\sim$1.5 nm up- and down-shift (one WDM channel). The resulting up- (down-) shifted pulse contains 29% (19%) of the launched energy with Q of 0.94 (0.92).

Although the applications discussed above all all pertain to tailoring $\Lambda(z)$ for

optimized frequency shift, it should also be possible to modify the grating structure to affect the temporal profile of the output pulse. This could for example be used to maximize compression of the frequency shifted FF, yielding output with higher peak power. While it has not been investigated, one could consider algorithms for local pulse optimization, so that at any point in propagation, the local structure is that needed to compress the field *at that point* (*i.e.*, with more advanced functional forms of $\Lambda(z)$ than the linear case considered here). Although it is beyond the scope of this Letter, this prospect warrants further study.

5.4 Conclusion

In conclusion, we have theoretically demonstrated the use of local nonlinearity control via poling period variation in QPM quadratic interactions to optimize frequency shifting. This new degree of freedom increases the efficiency and quality of frequency shifts from cascaded processes, and completes the analogy of cascaded frequency shifts to Raman induced shifts by allowing an effectively constant response time for the cascaded process. As an example, we theoretically show clean and efficient frequency shifting of submicrojoule, $\sim$100 fs pulses by hundreds of nanometers, and we show its applicability to wavelength-division multiplexing channel switching with pulse parameters representative of telecommunications systems in waveguided C-PPLN structures. We expect quadratic frequency shifting, enhanced with nonlinearity management, to have broad applications. Furthermore, this new capability is easily customizable and can be implemented with existing fabrication techniques.

This work was supported by the National Science Foundation (awards PHY-0099564 and ECS-0217958), and the National Institutes of Health (grant EB002019).

BIBLIOGRAPHY

[1] K. Beckwitt, F. Ö. Ilday, and F. W. Wise, Opt. Lett. **29**, 763 (2004).

[2] G. I. Stegeman, R. Schiek, L. Torner, W. Torruellas, Y. Baek, D. Baboiu, Z. Wang, E. Van Stryland, D. J. Hagan, and G. Assanto, "Cascading: A Promising Approach to Nonlinear Optical Phenomena," in *Novel Optical Materials and Applications*, I.C. Khoo, F. Simoni, and C. Umeton ed. (John Wiley & Sons, New York, 1997), Ch. 2, pp.49-76.

[3] A.V. Buryak, P. Di Trapani, D.V. Skryabin and S. Trillo, Physics Reports **370**, 63 (2002).

[4] K. Beckwitt, F. W. Wise, L. Qian, L. A. Walker, and E. Canto-Said, Opt. Lett. **26**, 1696 (2001).

[5] F. Wise, L. Qian, and X. Liu, J. Nonlinear Opt. Phys. & Mat. **11**, 317 (2002).

[6] F. Ö. Ilday and F. W. Wise, J. Opt. Soc. Am. B **19**, 470 (2002).

[7] C. R. Menyuk, R. Schiek, and L. Torner, J. Opt. Soc. Am. B **11**, 2434 (1994).

[8] F. Ö. Ilday, K. Beckwitt, Y.-F. Chen, H. Lim, and F. W. Wise, J. Opt. Soc. Am. B **21**, 376 (2004).

[9] A. A. Kanashov and A. M. Rubenchik, Physica D **4**, 122 (1981).

[10] J. P. Torres and L. Torner, Opt. Quant. Electron. **29**, 757 (1997).

[11] G. P. Agrawal. *Nonlinear Fiber Optics* (Academic Press: San Diego, 1995).

[12] M. M. Fejer, G. A. Magel, D. H. Jundt, and R. L. Byer, IEEE J. Quantum Electron. **28**, 2631 (1992).

[13] A. M. Schober, G. Imeshev, and M. M. Fejer, Opt. Lett. **27**, 1129 (2002).

[14] M. Cha, Opt. Lett. **23**, 250 (1998).

[15] S. Carrasco, J. P. Torres, L. Torner, and R. Schiek, Opt. Lett. **25**, 1273 (2000).

[16] S. C. Rodriguez, J. P. Torres, L. Torner, and M. M. Fejer, J. Opt. Soc. Am. B **19**, 1396 (2002).

[17] G. Imeshev, M. A. Arbore, M. M. Fejer, A. Galvanauskas, M. Fermann, and D. Harter, J. Opt. Soc. Am. B **17**, 304 (2000).

Chapter 6

Frequency shifting of 50 pJ pulses with cascaded quadratic processes in periodically poled lithium niobate waveguides[1]

We experimentally show nonlinear frequency shifting of infrared pulses in periodically poled lithium niobate waveguides using phase-mismatched quadratic processes with strong group-velocity mismatch. These experiments demonstrate cascaded frequency shifts with picojoule pulse energies, corroborating recent predictions of these effects. Low energy frequency shifts enable applications including tunable infrared sources for medical and frequency metrology applications and nonlinear frequency conversion devices for optical communications.

6.1 Introduction

In recent years, cascaded interactions in quadratic ($\chi^{(2)}$) nonlinear media have received significant attention as a route to large nonlinear phase-shifts of controllable magnitude and sign [2]. Cascaded phase-shifts have been shown to support solitons [3], compensate for Kerr phase-shifts [4], and prove useful for applications including modelocking of short-pulse lasers, pulse compression [5], and nonlinearity management for high energy fiber lasers [6].

[1]The results presented in this chapter have been submitted for publication (Ref. [1]).

To date, applications of cascaded quadratic phase shifts to femtosecond pulses have been in the stationary limit, where the fundamental (FF) and second-harmonic (SH) fields overlap temporally despite group-velocity mismatch (GVM) between them, producing an effective Kerr nonlinearity in the limit of large phase-mismatch [7]: *i.e.*, providing a surrogate for the bound-electronic cubic ($\chi^{(3)}$) nonlinearity.

Recently *non-stationary* cascaded phase shifts were demonstrated: GVM retards or advances (depending on its sign) the SH propagation with respect to the FF and the resulting nonlinear phase shift imparted on the FF is advanced or delayed with respect to the stationary phase by an amount depending on the ratio of GVM to phase-mismatch. This non-instantaneous nonlinear response manifests spectrally as redshifts or blueshifts of the pulse spectrum, which produces an analog of Raman nonlinearities from the quadratic process [8]. Cascaded frequency shifts were recently demonstrated, but in birefringently phase-matched materials with high energy (100 μJ - 1 mJ) pulses [8, 9]. In addition, it was theoretically predicted that cascaded frequency shifts are possible with significantly lower energies (picojoules to nanojoules) in waveguides in quasi-phase-matched [(QPM), *i.e.*, periodically poled] structures [8], and that the resulting shifts can be significantly enhanced and tailored in aperiodically poled (*chirped*) materials [10].

In this Letter we report observation of cascaded frequency shifts with picojoule energy pulses. These shifts are observed in periodically poled lithium niobate (PPLN) waveguides, where the small modal confinement gives strong nonlinear interactions with low pulse energies. Controllable nonlinear frequency shifts with picojoule energies enables a host of nonlinear frequency shifting processes in the infrared with pulse parameters applicable to existing fiber sources and optical communications applications.

6.2 Analytical and numerical results

We begin by reviewing the origin of non-stationary nonlinear frequency shifts from cascaded processes. The full coupled wave equations for the FF (a_1) and SH field envelopes within the slowly-varying envelope approximation are reduced to a single field equation for the FF through expansion in powers of the normalized phase-mismatch, $1/\beta$. Keeping only the lowest order correction from GVM yields [8, 10, 11]

$$\underbrace{i\frac{\partial a_1}{\partial \xi} - \frac{\delta_1}{2}\frac{\partial^2 a_1}{\partial \tau^2} - \frac{1}{\beta}[|a_1|^2 a_1}_{\text{NLSE}} + \underbrace{2i\frac{1}{\beta}|a_1|^2\frac{\partial a_1}{\partial \tau}}_{\text{Correction}}] = 0. \tag{6.1}$$

Here, time is normalized to the initial pulse duration, $\tau = t/\tau_0$, the propagation coordinate is $\xi = z/L_{\text{GVM}}$, and $\delta_j = L_{\text{GVM}}/L_{DS,j}$ with dispersion lengths $L_{DS,j} = {\tau_0}^2/\beta^{(2)}(\omega_j)$. $\beta = \Delta k L_{\text{GVM}}$ for $\Delta k = k_{2\omega} - 2k_\omega$ (the FF-SH wave-vector mismatch) and $L_{\text{GVM}} = \tau_0/(n_{1,g} - n_{2,g})$ for material group index $n_{j,g}$ with $j = 1, 2$.

The first part of Eq. (6.1) describes the standard nonlinear Schrödinger equation (NLSE) limit of the cascaded process [7]. The correction term results from GVM in the non-stationary limit and is responsible for the initial non-instantaneous phase shift. It can be shown [8] that this correction is qualitatively similar to a Raman-scattering term (of the form [12] $[T_R\, a_1\, \partial|a_1|^2/\partial\tau]$). In analogy to the Raman-scattering response time T_R, we define an effective response $T_R^{\text{eff}} \sim i/\beta$ for the cascaded process with two key differences: first, this effective response is imaginary (unlike the Raman response) so it alters the field envelope instead of contributing directly to the phase. The envelope change couples to the phase profile through the remaining terms of Eq. (6.1) to generate a Raman like frequency

shift. Second, the frequency shifting saturates with $1/\beta \sim 1/\Delta k(\lambda)$: as the pulse's frequency evolves during the shifting process, Δk changes, eventually saturating the shift.

In birefringently phase-matched and periodically poled QPM materials, saturation is unavoidable and practically limits the maximum achievable frequency shift to a few times the spectral bandwidth of the input pulse (however, saturation is avoidable in *chirped* QPM structures [10]). In QPM, the net phase-mismatch is given by

$$\Delta k_{\mathrm{net}}(\lambda) = \Delta k_{\mathrm{mat}}(\lambda) - \frac{2\pi}{\Lambda}, \tag{6.2}$$

where Δk_{mat} is the wavelength-dependent material phase-mismatch and Λ is the poling period of the nonlinear tensor element (d_{33} in PPLN).

As in refs. [8] and [10] we solve the coupled wave equations for the FF and SH numerically with a standard split-step beam propagation method. The simulated pulse evolution appears in Fig. 6.1, under conditions corresponding to the experiments described below. Fig. 6.1(a) and (c) show the output spectrum for input wavelengths below and above phase-matching [(PM), as determined by Eq. (6.2) with the proper material parameters]. Here wavelengths below (above) PM correspond to self-defocusing (self-focusing) nonlinearity and blueshifts (redshifts) of the pulse spectrum. With propagation, the spectrum evolves in analogy to Raman soliton dynamics, but only with the proper signs of effective nonlinearity and group-velocity dispersion for soliton formation (which in turn restricts the frequency shifting to either higher or lower frequencies). The corresponding temporal intensity profile of the fields appear in Fig. 6.1(b) and (d). For 1550 nm [Fig. 6.1(b),

below PM], the frequency shift is to the blue which supports soliton formation and a clean temporal field evolves. In contrast, redshifts [Fig. 6.1(d), above PM] distort the pulse shape, limiting the maximum achievable shift with short pulses. For this combination of GVM and Δk, blueshifting yields a temporal delay [(Fig. 6.1(b)]. As expected from the effective-Raman analogy, initially the frequency shift is linear followed by saturation from the cascaded process [Fig. 6.1(e)].

6.3 Experimental results

Experiments (schematic in Fig. 6.2) were performed with infrared pulses from an optical-parametric oscillator (OPO) (synchronously pumped by a Ti:sapphire oscillator) producing >1-nJ, near-Gaussian transform limited <200-fs pulses tunable from 1200-1700 nm. The measurements were carried out in a 4.7 cm long PPLN waveguide fabricated by in-diffusion of a 7 μm $\times$ 98 nm Ti-stripe for 8 hours at 1060 °C in an argon inert gas atmosphere and 1 hour post-diffusion at the same temperature in oxygen [13]. The resulting channel guide is single mode with dimensions 3.4 μm $\times$ 4.7 μm. The PPLN is poled with $\Lambda \sim 17$ μm and the waveguide was heated in an oven to 160 °C, both to prevent photorefractive damage and to control the PM conditions: for the operating temperature chosen, PM occurs at $\lambda_{\mathrm{PM}} = 1590$ nm.

Measured coupling loss into the waveguide was high. Typical energy throughput was ∼15% from the input to output objectives, and only ∼30% of this was guided in the waveguide core: *i.e.*, ∼50 pJ guided energy (900 MW/cm^2) required ∼1 nJ at the input objective. We attribute the high loss and unguided background energy to poor spatial coupling due to a non-Gaussian OPO mode. In the data, the presence of unguided light gives higher spectral background (wings) than is

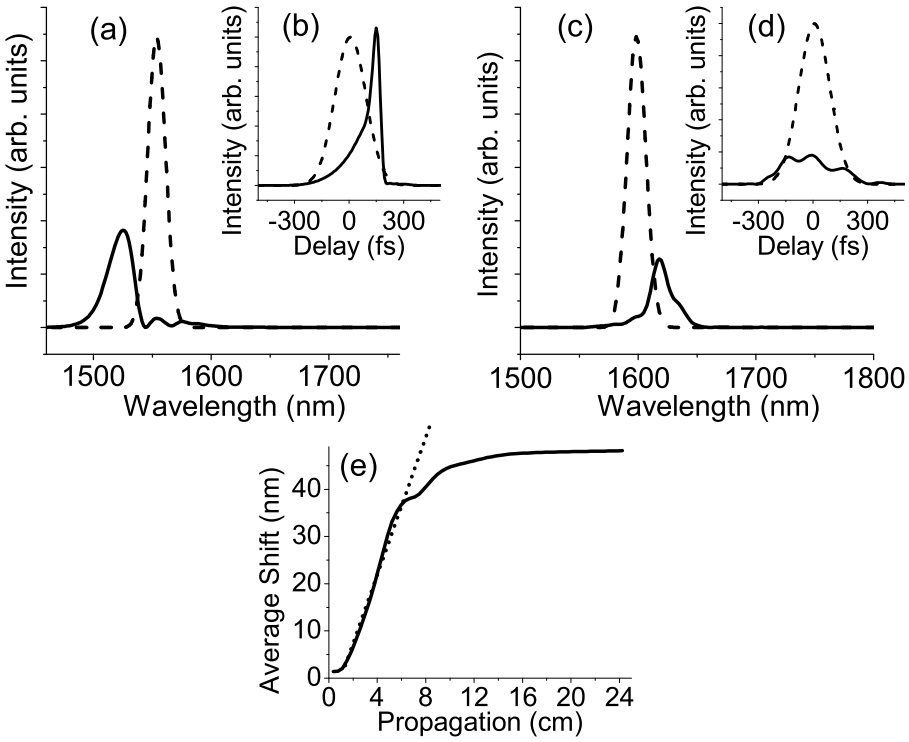

Figure 6.1: Simulated pulse evolution with parameters corresponding the experiment. (a) and (c) show the output spectra for propagation through 4.7 cm of material with input profiles centered at 1555 nm and 1600 nm, corresponding to phase-matching conditions for blueshifts and redshifts, respectively. Insets (b) and (d) show the corresponding temporal intensity profiles. (e) shows the average spectral shift with 5× longer propagation length. Dots indicate the linear region of shift that is followed by saturation. In all cases dashes indicate the input profiles.

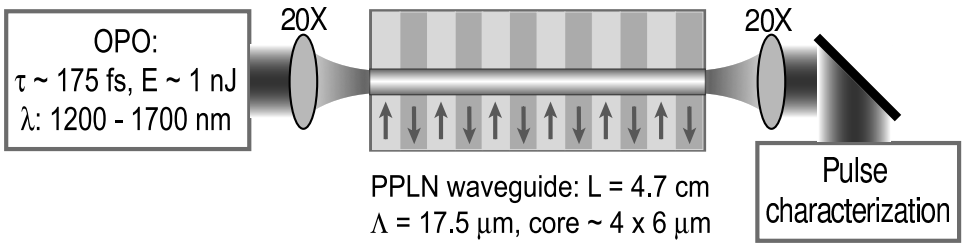

Figure 6.2: Schematic of the experiment. 20X indicate polarization-maintaining (20X) microscope objectives.

otherwise expected.

Fig. 6.3 shows spectral output from the PPLN waveguide with input spectra centered at 1410 nm [Fig. 6.3(a)] and 1575 nm [Fig. 6.3(b)]. These wavelengths correspond to net Δk [from Eq. (6.2)] of 37 π/mm and 3 π/mm, respectively. The stationary conditions at 1410 nm yield no spectral shift (the slight modulation is most likely due to spatial coupling). At 1575 nm, GVM = -315 fs/mm, which corresponds to a boundary for stationary phase-shifts of $\Delta k > 6$ π/mm (defined as $|\Delta k| \geq 2\pi \mathrm{GVM}/\tau$) [8]. Hence these conditions are well into the non-stationary regime and a significant blueshift in the spectral peak is observed [Fig. 6.3(b)]. The background in Fig. 6.3(b) is likely due to a combination of higher order soliton structure and spectral modulation from waveguide coupling.

Fig. 6.3(c) shows the expected saturation of the frequency shift with increasing energy in the waveguide. We observe the shift to saturate at ∼2 times the input pulse bandwidth, in good agreement with the ∼2.5 times predicted from simulations [Fig. 6.1(c)].

The saturated shift as a function of input wavelength [and Δk_{net} through Eq. (6.2)] appears in Fig. 6.4. Apparent are both the expected reversal in sign of the frequency shift at PM and reduced magnitude of the shift away from PM (mov-

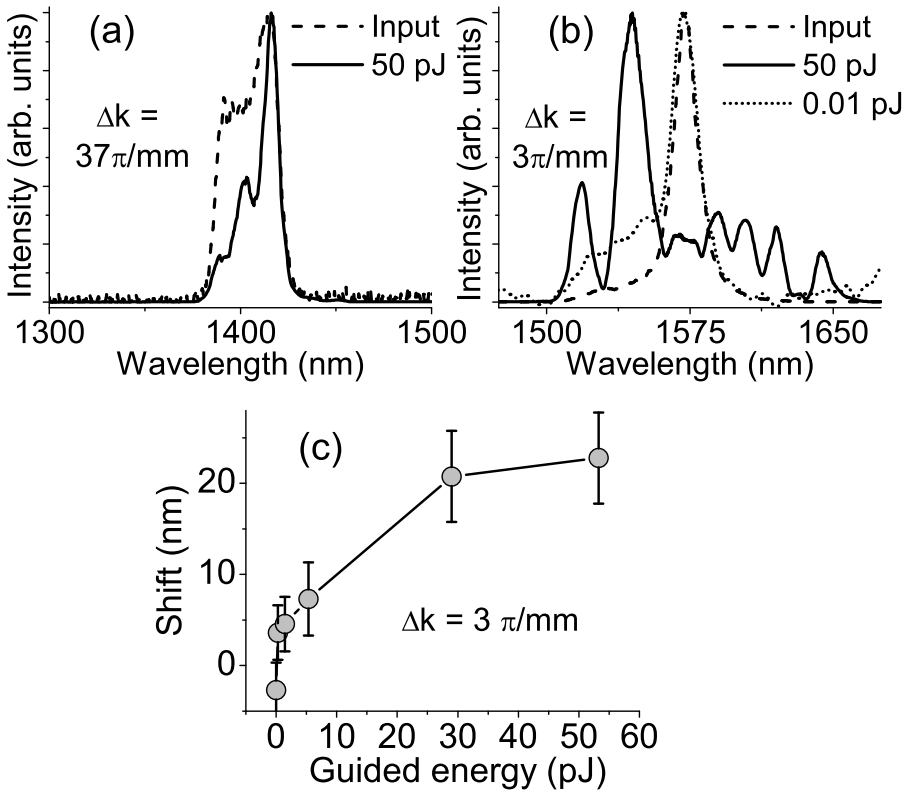

Figure 6.3: Output spectra from the waveguide with input spectra centered at (a) 1410 nm and (b) 1575 nm. Dots in (b) show low power data, with no spectral shift. Dashes show the input spectra. Saturation of the average spectral shift with guided energy at 1575 nm appears in (c).

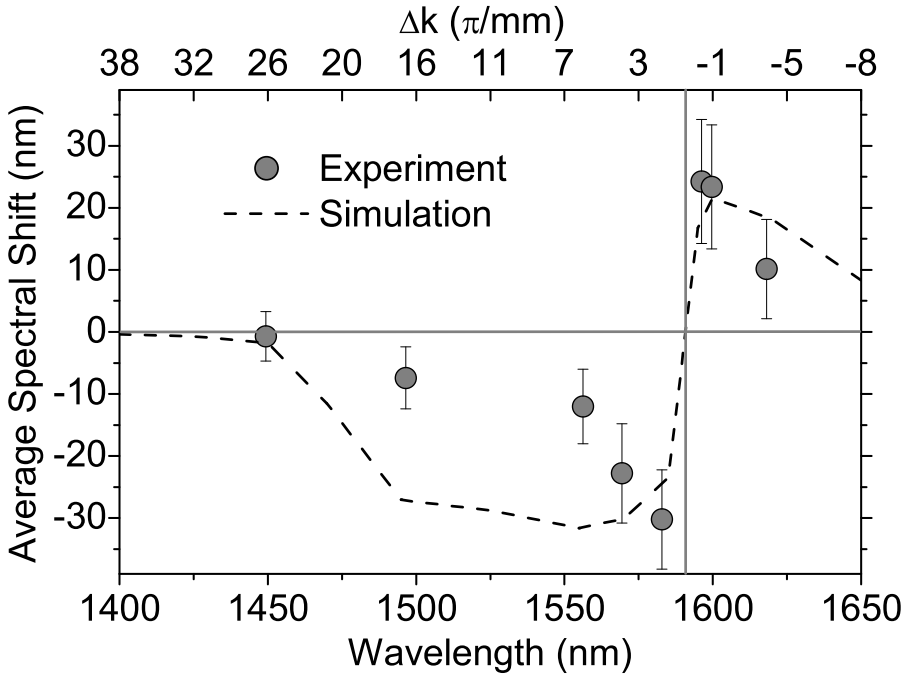

Figure 6.4: Saturated spectral shift versus input wavelength (bottom) and phase-mismatch (top). Dashes show simulations with parameters corresponding to the experiment. Phase-matching corresponds to 1590 nm.

ing into the stationary limit). These data are in good agreement with numerical simulations.

6.4 Conclusion

In summary, we demonstrate nonlinear frequency shifting of ∼50 pJ pulses with non-stationary cascaded quadratic processes in waveguided PPLN. The small modal area of the waveguide allows shifts with low pulse energies. Combined with an infrared fiber laser one can envision compact, robust, and tunable short-pulse sources based on the low energy cascaded frequency shifts demonstrated here. Furthermore, these shifts should be extendible to 100's of nm in chirped PPLN waveguides. Such sources have immediate implications for medical and frequency metrology applications. In addition, cascaded frequency shifts with picojoule energies in chirped waveguides allow numerous devices for communications applications including wavelength devision multiplexing, channel switching, and high extinction discrimination.

This work was supported by the National Science Foundation (awards PHY-0099564 and ECS-0217958), and the National Institutes of Health (grant EB002019). The authors thank H. Lim and S. W. Clark for valuable discussions.

BIBLIOGRAPHY

[1] K. Beckwitt, F. Ö. Ilday, W. Grundkötter, W. Sohler, and F. W. Wise, Opt. Lett. (submitted for publication).

[2] G. I. Stegeman, R. Schiek, L. Torner, W. Torruellas, Y. Baek, D. Baboiu, Z. Wang, E. Van Stryland, D. J. Hagan, and G. Assanto, "Cascading: A Promising Approach to Nonlinear Optical Phenomena," in *Novel Optical Materials and Applications*, I.C. Khoo, F. Simoni, and C. Umeton ed. (John Wiley & Sons, New York, 1997), Ch. 2, pp.49-76.

[3] A.V. Buryak, P. Di Trapani, D.V. Skryabin and S. Trillo, Physics Reports **370**, 63 (2002).

[4] K. Beckwitt, F. W. Wise, L. Qian, L. A. Walker, and E. Canto-Said, Opt. Lett. **26**, 1696 (2001).

[5] F. Wise, L. Qian, and X. Liu, J. Nonlinear Opt. Phys. & Mat. **11**, 317 (2002).

[6] F. Ö. Ilday and F. W. Wise, J. Opt. Soc. Am. B **19**, 470 (2002).

[7] C. R. Menyuk, R. Schiek, and L. Torner, J. Opt. Soc. Am. B **11**, 2434 (1994).

[8] F. Ö. Ilday, K. Beckwitt, Y.-F. Chen, H. Lim, and F. W. Wise, J. Opt. Soc. Am. B **21**, 376 (2004).

[9] K. Beckwitt, J. A. Moses, F. Ö. Ilday, F. W. Wise, J. Nees, E. Power, K. H. Hong, B. Hou, and G. Mourou, "Cascade-Raman soliton compression with 30-fs, terawatt pulses," presented at the conference on Nonlinear Guided Waves and Their Applications, Toronto, Canada, 28-31 Mar. 2004.

[10] K. Beckwitt, F. Ö. Ilday, and F. W. Wise, Opt. Lett. **29** 763 (2004).

[11] J. P. Torres and L. Torner, Opt. Quant. Electron. **29**, 757 (1997).

[12] G. P. Agrawal. *Nonlinear Fiber Optics* (Academic Press: San Diego, 1995).

[13] G. Schreiber, H. Suche, Y.L. Lee, W. Grundkötter, V. Quiring, R. Ricken, and W. Sohler, Appl. Phys. B **73**, 501 (2001).

Chapter 7

"Cascade-Raman" soliton compression with 30-fs, terawatt pulses[1]

Theoretically, Raman-like soliton compression of mJ, 30-fs pulses is predicted. Initial experiments demonstrate 2 times compression of 1.3 TW/cm^2 pulses under non-optimal conditions. The results agree closely with numerical simulations.

7.1 Introduction

In recent years, there has been much interest in the large nonlinear phase shifts of controllable sign and magnitude resulting from cascaded processes in quadratic materials [2]. In the limit of large phase-mismatch between the fundamental (FF) and second-harmonic (SH) fields (the so-called stationary limit in which the FF and SH continue to overlap temporally despite the presence of group-velocity mismatch (GVM) between them), this process asymptotically produces a Kerr-like nonlinear phase [3]. This phase has successfully been used to generate solitons [4], compensate for temporal and transverse nonlinear effects in propagation [5], and provide a means of high energy pulse compression [6], among other applications [7].

Cascaded quadratic phase shifts are particularly advantageous for compression of high energy pulses (fractions of a millijoule and higher), since pulse-compression methods based on cubic nonlinearity cannot be used, owing to the limitations of excessive nonlinearity in single-mode waveguides and material damage through self-

[1]The results presented in this chapter have been published in Ref. [1].

focusing in unguided geometries. Self-defocusing nonlinearities in quadratic media bypass these difficulties, and have been used for 3-4X compression of ∼120fs pulses [6]. In addition, single-stage (soliton-like) compression under similar conditions has recently been demonstrated [8].

However, both of these applications rely on stationary or near-stationary phase shifts from the quadratic process, and are consequently limited to compression of longer (∼100-fs) pulses. This can be understood as follows: all quadratic materials exhibit GVM. In order to overcome this effect and regain a near-stationary quadratic phase, a phase-mismatch $|\Delta k| \gtrsim 4\pi/L_{\mathrm{GVM}} = 4\pi\mathrm{GVM}/\tau_0$ is necessary [7], where τ_0 is the FF pulse-width. Hence shorter pulses require working at larger $|\Delta k|$. However, for net negative phase, the quadratic phase must be large enough to overcome the cubic phase present in quadratic materials. Since the quadratic phase $\sim 1/\Delta k$, it is not possible to produce a large enough net nonlinear phase for significant compression in the stationary regime with input pulse-widths significantly below 100-fs.

Recently it was demonstrated that under such non-stationary conditions, the cascade process yields a non-instantaneous phase shift. This non-instantaneous phase produces an effective frequency shift on the FF, in analogy to a controllable Raman-scattering process [9]. Under these conditions, it is possible to implement an analog of Raman-soliton compression using the non-instantaneous quadratic response: high-order solitons are formed, producing a compressed primary pulse that undergoes a continuous self-frequency shift. An advantage of this approach over soliton-like compression in the stationary limit is that the pedestal commonly produced by Raman-soliton compression consists mainly of unshifted frequency components. These components may be eliminated with a frequency filter to yield

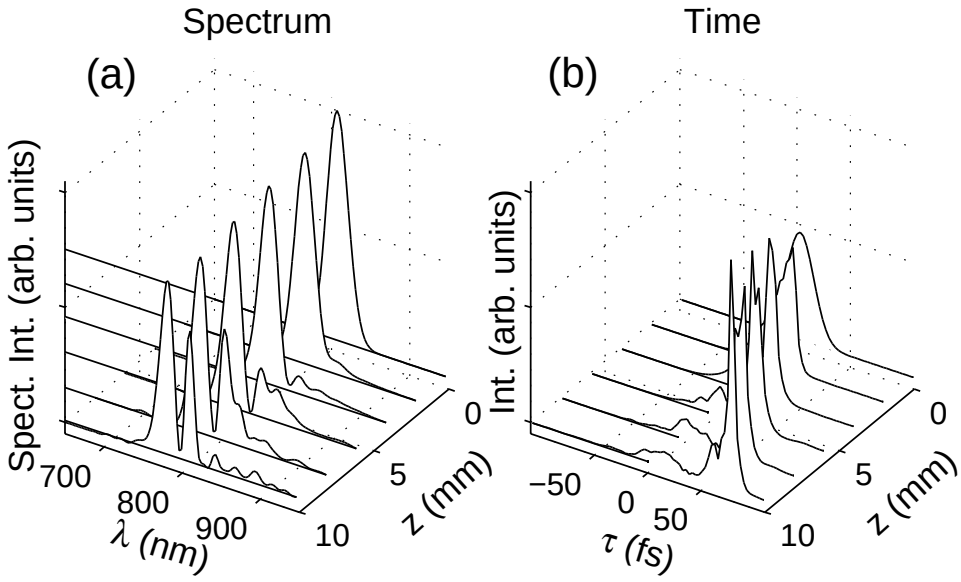

Figure 7.1: Simulated evolution of the pulse spectrum (a) and temporal profile (b) under conditions similar to experiments in Fig. 7.2.

a cleaner pulse.

7.2 Numerical results

Numerically we solve the coupled wave equations for the FF and SH using a symmetric split-step beam propagation method [5] for conditions corresponding to the experimental parameters listed below. The numerical evolution is shown in Fig. 7.1. The launched pulse compresses and undergoes frequency shifting to shorter wavelengths with propagation. The separation between the uncompressed and compressed parts of the pulse increases with increasing spectral shift (as with ordinary Raman-soliton evolution), which should aid recovery of a clean, compressed pulse after spectral filtering.

7.3 Experimental results

Experiments (Fig. 7.2) were performed with ∼30-fs, 0.62-mJ pulses, centered at 810-nm, generated by a Ti:sapphire amplifier. The launched beam shape was approximately Gaussian (but elliptical) with waists 0.8 mm and 0.55 mm, corresponding to a peak intensity of ∼1.3 TW/cm^2. Pulse evolution was studied in 2.5-mm of the quadratic material β-barium metaborate (BBO). Conditions of optimal compression are found between (10-20)π/mm, corresponding to self-defocusing phase below the stationary boundary (∼40π/mm).

Compared to the simulated evolution, the measured spectrum and autocorrelation (Fig. 7.2(a)-(b)) are quite similar, except that the measured temporal wings are larger than expected; however the width of the compressed center spike (∼15-fs) is in very good agreement with calculation. The experimental results in Fig. 7.2 closely match the numerical results shown in Fig. 7.1 for the corresponding propagation length. In simulation (Fig. 7.1), the pulse undergoes further compression at propagation lengths beyond the 2.5-mm used in these initial experiments, indicating that this crystal length was less than optimal.

To further study the frequency shifting dynamics, we examine the pulse spectrum over a range of Δk (Fig. 7.3). As expected, shifts to lower (higher) wavelengths are observed for net negative (positive) nonlinear phase. The exact agreement in Δk values differ somewhat but the trends match closely.

In Fig. 7.3, both the stationary boundary and the point where the cascade and Kerr phases are equal in magnitude occur near $|\Delta k| = 40\pi$/mm. The trend in Fig. 7.3 can be understood as follows: for large positive Δk, the cascade phase shift is nearly stationary, and nearly equal and opposite in magnitude to the Kerr phase, so the spectrum is unchanged. Closer to phase matching, the net phase is

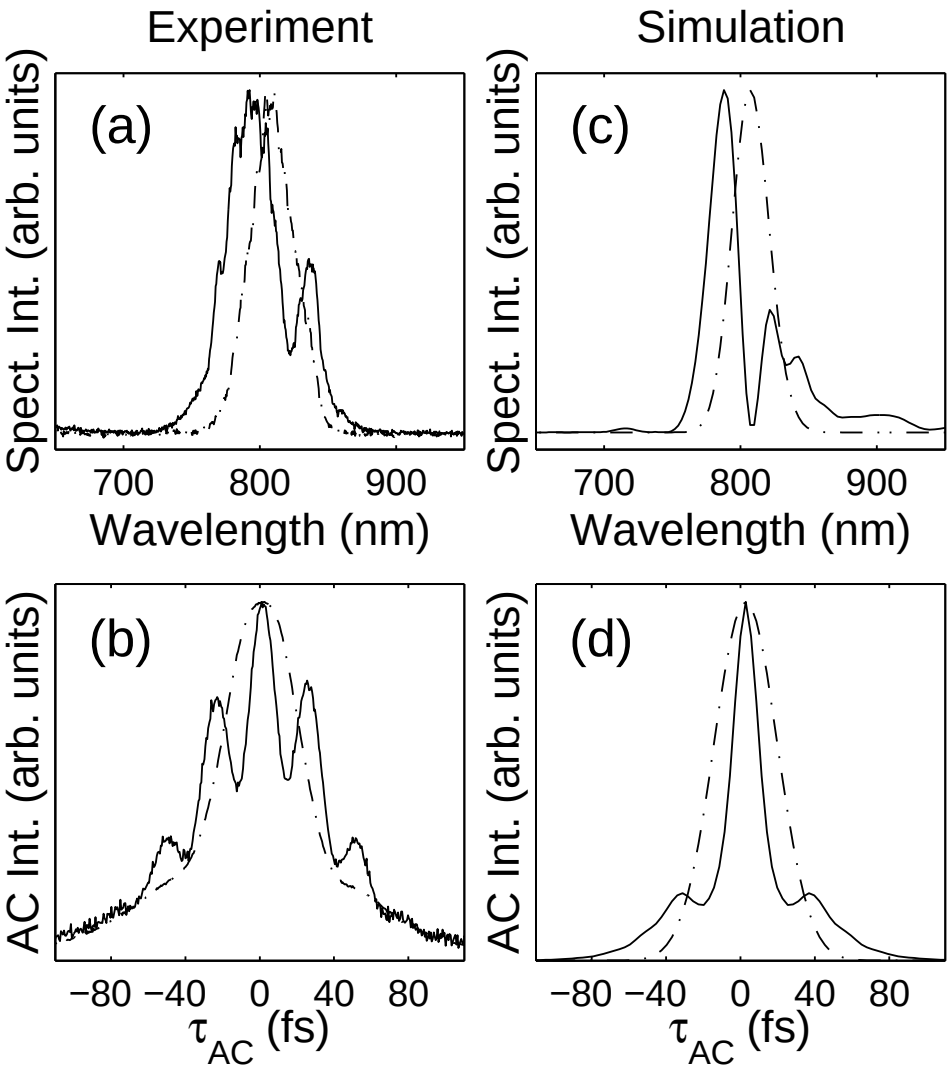

Figure 7.2: Measured spectrum (a) and auto-correlation (b) under conditions of optimal compression. Dash-dots show input profiles. The launched pulse in (b) corresponds to a deconvolved width of ∼35-fs, and the compressed center spike is ∼15-fs. Simulations ((c)-(d)) correspond to propagation under similar conditions.

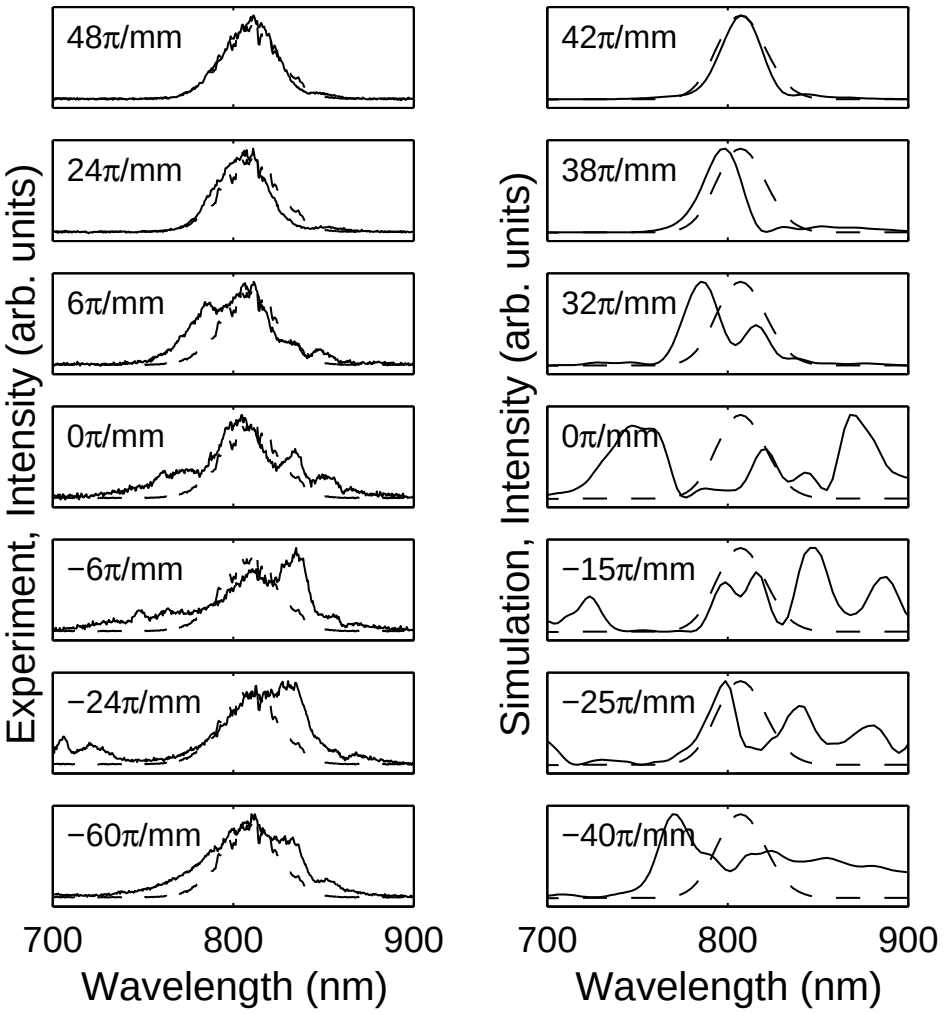

Figure 7.3: Experimental (left) and simulated (right) spectra under conditions similar to experiments in Fig. 7.2. Launched pulse energy is 0.53 mJ ($\sim$1.1 TW/cm^2). Dashes show the input spectrum.

negative and a shift to shorter wavelengths and spectral broadening are observed. On the self-focusing side ($\Delta k > 0$), the Kerr and cascade phases add (yielding spectral broadening), and shifts to longer wavelengths are observed. Finally, for large negative Δk the cascade phase is nearly stationary so no net spectral shift is observed, but self-phase modulation from n_2 broadens the spectrum. The asymmetry in Δk between experiment and simulation could be due to the exact value of n_2 used for BBO, which provides the nonlinear phase offset and is somewhat experimentally uncertain. Unfortunately we were limited to $\sim \pm 50\pi$/mm experimentally (due to beam clipping at large angles), so we could not study far beyond the stationary cascade limit.

7.4 Conclusion

In conclusion, we demonstrate 2 times compression of 30-fs, 0.6-mJ ($\sim$1.3 TW/cm^2) pulses with non-instantaneous, self-defocusing cascade phase shifts under non-stationary conditions. This is the first evidence of quadratic pulse compression of $\sim$30-fs pulses, and provides further experimental verification of the recent report of non-instantaneous phase shifts from non-stationary cascaded processes. This experiment demonstrates Raman soliton-like pulse compression with frequency shifts from cascaded quadratic processes below the stationary boundary. Experimentally, the compression produces a short (15-fs) central spike, and there is good indication that the residual pulse pedestal will be further separated from the compressed pulse (and can potentially be filtered out), with propagation through slightly longer crystal lengths.

BIBLIOGRAPHY

[1] K. Beckwitt, J. A. Moses, F. Ö. Ilday, F. W. Wise, J. Nees, E. Power, K. H. Hong, B. Hou, and G. Mourou, "Cascade-Raman soliton compression with 30-fs, terawatt pulses," presented at the conference on Nonlinear Guided Waves and Their Applications, Toronto, Canada, 28-31 Mar. 2004.

[2] R. DeSalvo, D. J. Hagan, M. Sheik-Bahae, G. Stegeman, E. W. Van Stryland, and H. Vanherzeele, H., Opt. Lett. **17**, 28 (1992).

[3] C. R. Menyuk, R. Schiek, and L. Torner, J. Opt. Soc. Am. B **11**, 2434 (1994).

[4] A.V. Buryak, P. Di Trapani, D.V. Skryabin and S. Trillo, Physics Reports **370**, 63 (2002).

[5] K. Beckwitt, F. W. Wise, L. Qian, L. A. Walker, and E. Canto-Said, Opt. Lett. **26**, 1696 (2001).

[6] X. Liu, L. J. Qian, and F. W. Wise, Opt. Lett. **24**, 1777 (1999).

[7] F. Wise, L. Qian, and X. Liu, J. Nonlinear Opt. Phys. & Mat. **11**, 317 (2002).

[8] S. Ashihara, J. Nishina, T. Shimura, K. Kuroda, J. Opt. Soc. Am. B **19**, 2505 (2002).

[9] F. Ö. Ilday, K. Beckwitt, Y.-F. Chen, H. Lim, and F. W. Wise, J. Opt. Soc. Am. B **21**, 376 (2004).

Chapter 8

Future directions

8.1 Quadratic solitons without pulse tilt: a realistic route to "light-bullets"

To this day, observation of stable, fully confined spatiotemporal solitons or "light-bullets" [1] remains one of the great challenges in soliton physics. Researchers are intrigued by light-bullets both for the opportunities they present for research into highly nonlinear pulse propagation and for their potential applications to terahertz-rate optical logic. Experimentally light-bullets remain unobserved for many reasons: the conditions required for their formation and stable propagation place severe constraints on the properties on the nonlinear media employed experimentally; as dynamical solutions of highly nonlinear systems, they are susceptible to a number of instabilities — the dynamics of which are closely related to soliton formation and consequently occur at similar conditions (namely transverse and longitudinal modulational instabilities); and even in the most highly nonlinear materials available, solitons require short, energetic pulses to form.

Building on recent observations within our group of two-dimensional spatiotemporal solitons, their instabilities, and the realization that the physical system used for their observation precludes light-bullet formation, this thesis presents a new route to temporal soliton formation in quadratic media. In addition to identifying a new class of quadratic temporal solitons (*i.e.*, solitons with near-zero or even normal group-velocity dispersion at the second-harmonic frequency), these soliton solutions appear to be extendible to two- and three-dimensions. This is

arguably the only currently known and experimentally realizable optical system to theoretically support light-bullets.

Realization of these optical systems rely on two key points: recent advances in materials fabrication which has made precise quasi-phase-matching of nonlinear optical materials possible. In this way, a host material (in this case lithium niobate) is identified with the correct (large and anomalous) group-velocity dispersion. Periodic poling then enables phase mismatched propagation through modification of the nonlinear properties of the material with propagation. Also, it was recognized that stable (or quasi-stable as detailed in Chapter 3) soliton formation occurs in quadratic systems for a range of second-harmonic group-velocity dispersion values.

While these solutions have not been observed, the existence of a route to three-dimension soliton formation is of huge importance. The first step along this path is the demonstration of stable temporal solitons in these systems, followed by extension to one and two transverse dimensions. Eventually, these systems should prove an excellent test bed for experiments into soliton formation and interactions across a range of experimental conditions.

8.2 Nonlinear frequency shifts from cascaded processes

The theory and experiments presented here demonstrating generation of useful nonlinear frequency shifts from cascaded quadratic processes are new. Chapters 4, 5, 6, and 7 discuss the underlying properties of these shifts and demonstrate their applicability to a range of physical systems from high energy, extremely short pulse amplified lasers to low energy fiber and solid state oscillators.

Building on these results, Sections 8.3, 8.4 and 8.5 develop several applications of cascaded frequency shifts. However, as controllable analogs of Raman-scattering

processes, we hope that frequency shifts from cascaded interactions will provide applications as far-reaching and varied as those Raman shifts themselves. The majority of these applications remain to be explored.

8.3 Tunable, short-pulse infrared sources with cascaded frequency shifts

Many applications would benefit from a compact and stable means of tunably shifting the wavelength of light output from fixed frequency laser sources, in particular at infrared wavelengths. Common infrared lasers are available near 800 nm (titanium:sapphire based solid-state lasers), near 1 micron (both ytterbium fiber based sources and various neodymium doped glass solid-state lasers), and near 1550nm (erbium doped fiber lasers). A means of shifting the wavelength of these sources is highly desirable, with applications ranging from multi-photon microscopy and optical coherence tomography for medical science to ultrafast spectroscopy and frequency metrology to tunable sources for high bit-rate telecommunications systems. In addition, numerous areas of basic scientific research require tunable output at frequencies outside the range of available sources.

Historically two main techniques dominate wavelength shifting and conversion: frequency shifts from Raman-scattering processes in optical fiber, and optical parametric oscillators and amplifiers. Both of these techniques have disadvantages: Raman shifting is limited to shifting toward *longer* wavelengths, and requires many meters to kilometers of optical fiber to generate appreciable wavelength shifts. In addition, the amount of shift is not easily tunable in an integrated fashion, since it requires changing the length of the material providing the shift (*i.e.*, the

fiber length in the above example) for a given pulse width and energy. Optical parametric oscillators and amplifiers provide highly tunable means of wavelength conversion (over a broad range of output wavelengths using different nonlinear materials), however, they are very complex optical systems. As such they are physically large, and require precise alignment and frequent adjustment. Hence, they are not practical for use in integrated environments and for application where stable performance over long periods of time is required. Given the constraints of these available frequency shifting methods, a more stable and simple method is highly desirable.

As shown in Chapters 4, 5, and 6, cascaded frequency shifts are eminently usable for this application. Coupled with the tendency for the frequency shifted pulses to undergo Raman-like soliton pulse compression, the resulting frequency shifted output can be spectrally and temporally clean with comparable input and output peak powers. Also, depending on the details of the cascaded material used, the magnitude of the frequency shift can be easily tuned in real time: in bulk materials the phase-matching conditions are easily adjusted, and poled structures with varying poling parameters transverse to the direction of propagation [for example"fan-out" PPLN with continuously variable poling period, Fig. 8.1(b)] can provide tunability in quasi-phase-matched systems.

A schematic of such a laser source appears in Fig. 8.1(a) with a diagram of a typical continuously variable PPLN structure in Fig. 8.1(b). Such a simple configuration, with the possible addition of an amplifier stage as necessary, could provide a very compact and robust tunable short pulse source. In principle this type of source, with additional integrated amplification as necessary, provides many of the advantages currently available with solid-state laser sources and optical

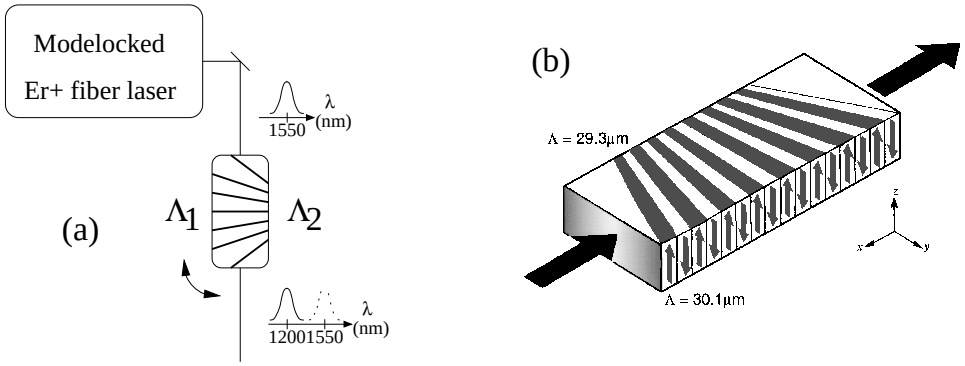

Figure 8.1: (a) Tunable source schematic consisting of a standard modelocked erbium fiber laser and a quadratic material (here variable period PPLN) providing the frequency shift. (b) shows a diagram of a typical "fan-out" PPLN structure [2].

parametric oscillators and amplifiers but in a much simpler, cheaper, and more stable package.

8.4 Compact and robust femtosecond frequency comb sources using nonlinear frequency shifting with cascaded quadratic processes[1]

Recently a new generation of ultra-precise optical clocks have been demonstrated, using femtosecond-duration laser pulses with ultra-broad spectra as frequency comb synthesizers. In analogy to a mechanical clock, these laser synthesizers are the gears connecting the clock's pendulum to its hands, but the pendulum is the frequency of the laser's optical field, and the hands are the pulses it emits. The

[1]Section 8.4 was part of a National Institute of Standards research proposal written by K. Beckwitt with editorial comments from S. A. Diddams and L. Hollberg.

pulses from both solid-state and fiber lasers have been used to generate broadband femtosecond frequency combs, but each has limitations due to the stability and complexity of the physical processes involved. Here a new type of source for optical frequency combs is proposed, utilizing a recently demonstrated frequency shifting process in quadratic nonlinear optical materials. Combined with existing infrared fiber lasers, this process enables compact and stable optical frequency comb sources with clear advantages over existing sources: they are significantly more compact and robust than titanium:sapphire solid-state lasers, and potentially have lower noise levels than a recently demonstrated fiber source based on spectral broadening in highly nonlinear optical fiber. As such, these sources have the potential to further increase the measurement limits of optical clocks, and prove invaluable for frequency metrology and related fields.

8.4.1 Introduction

The last few years have seen a revolution in optical clocks and optical frequency metrology, enabled by the development of phase-stabilized modelocked femtosecond laser sources capable of producing ultra-broadband coherent optical frequency combs. Temporally, these sources are remarkable because their pulse duration is only several times the optical cycle length: each pulse contains just a few cycles of the underlying carrier field. To be useful for frequency metrology, the relative phase of the carrier field and the pulse envelope must be known from one pulse to the next. This means the underlying optical field must not change (or must only change by a fixed amount) with each roundtrip of the laser cavity. With current feedback technology, this is possible for hours at a time, and longer durations are expected [3]. For a 1-GHz pulsed laser, this means the relative carrier-envelope

phase is locked for $\sim 10^{12}$ round trips of the laser cavity!

Spectrally, these frequency combs consist of a series of "teeth" at frequencies $f_n = n \times f_r + f_o$ where f_r is the laser repetition rate, and f_o is the offset of the lowest comb element from zero (which is related to the carrier-envelope-offset (CEO) phase described above). Remarkably, once these two parameters are fixed, the frequency comb provides a coherent relation between the optical frequency of the laser source, and the repetition rate at which it emits pulses. Physically, this means the cavity round trip time is just an integer multiple of the carrier field's cycle duration (of course the integer is quite large).

This relation enables frequency combs from femtosecond modelocked lasers to function as optical synthesizers, relating optical frequencies (hundreds of THz) to laser pulse repetition rates (0.1-1 GHz). This coherent spanning of six orders of magnitude is hugely significant: since electronic detection is limited to tens of GHz, femtosecond optical frequency combs enable clocks based on optical frequency transitions, versus the microwave transitions which have set timing precision standards for the last half-century. Recently, a femtosecond frequency comb based optical clock was demonstrated with an order of magnitude improvement in frequency stability over the best microwave standards, and improvements of several orders of magnitude beyond this are expected [4]. In addition, femtosecond optical combs have significant applications to improving the state of the art in optical frequency metrology, measurements of fundamental physical constants, and for technological applications such as ultra-dense wavelength-division multiplexing and as ultra-high resolution optical synthesizers for coherent-control and time-resolved spectroscopy.

8.4.2 Existing sources (and their limitations)

Use of an optical frequency comb requires precise knowledge of its parameters. The repetition rate of a pulsed laser f_r is easily measured. However, the CEO frequency f_o is much more difficult to determine. One method is to beat one of the comb elements against a known frequency source (such as a continuous-wave laser frequency locked to a reference atomic transition). This has been demonstrated [5], however a means of "self-referencing" f_o which does not require an external frequency standard is highly preferable. Luckily there is a way: if the frequency comb spans an octave (*i.e.*, from f to $2f$), nonlinearly frequency doubling the spectral components at f and beating the output against those at $2f$ produces beat frequencies $f_r \pm f_o$, which are easily seen in the radio-frequency power spectrum. Unfortunately, even lasers with sub-two-cycle pulsewidths (the shortest recorded) do not produce octave-spanning spectra.

To date two solutions have been presented: subsequent broadening of laser pulse spectra to octave widths is possible with supercontinuum generation in microstructured and highly nonlinear optical fibers [6, 7]. These fibers have unique dispersion properties due to their transverse structure which confines the guided light to an extremely small central core, resulting in highly nonlinear propagation and spectral broadening. Octave-width frequency combs based on supercontinuum generation have been demonstrated with titanium:sapphire (Ti:s) solid-state lasers around 800 nm [8, 7], and more recently with an erbium-fiber laser (ErF) at 1550 nm [9].

Unfortunately, spectral broadening in microstructured fiber has problems: these fibers are hard to couple light into, and both the coupling and spectral output are unstable over extended time periods. Furthermore, supercontinuum generation

adds significant spectral noise [10], and theory suggests this noise is fundamental to the supercontinuum process [11]. To avoid supercontinuum generation, researchers have explored alternative methods to generate broader intracavity spectra directly from Ti:s lasers [12] and recent experiments demonstrate such a source [13, 14]. However, this method cannot be applied to fiber lasers.

This presents a quandary: without relying on supercontinuum to broaden the spectrum, a self-referenced frequency comb from a fiber source is highly desirable. Fiber lasers are much more compact and stable than solid-state lasers. If optical frequency combs from femtosecond lasers are to find widespread use, they must be compact and robust. Ultimately, fiber based sources present the most promising (and in all likelihood the only viable) option for femtosecond frequency comb sources to be used out of research laboratories. In addition, sources in the 1000-1600 nm range are desirable for telecommunications applications, and to tie into existing optical frequency standards. To these ends, development of such a source is the subject of this proposal.

8.4.3 Controllable nonlinear frequency shifts with cascaded quadratic processes

Recently, we suggested [15, 16], and demonstrated [15, 18, 17] that useful nonlinear frequency shifts are possible with phase-mismatched processes in quadratic nonlinear optical materials. Due to the second-order nonlinearity in quadratic materials, launching a fundamental frequency (FF) field at f seeds its second-harmonic (SH) at $2f$. The most common application of quadratic materials is *phase-matched* second-harmonic generation (SHG), where the goal is to maximize the energy transfer to the SH: *i.e.*, for frequency conversion.

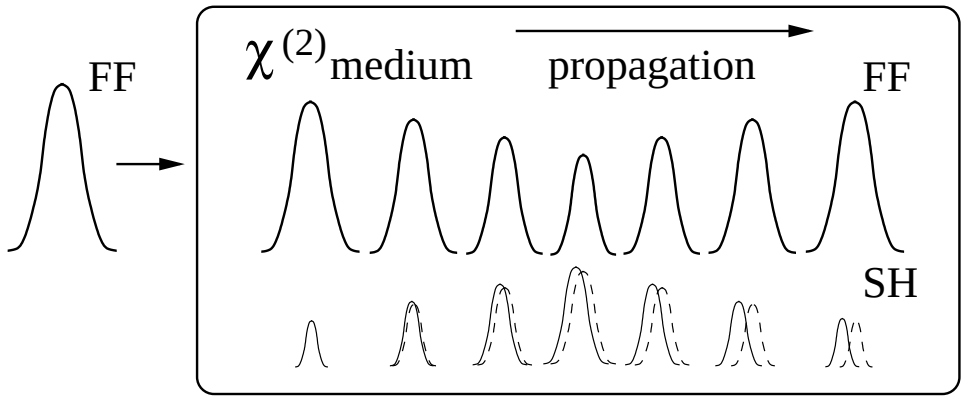

Figure 8.2: Illustration of the phase-mismatched cascaded quadratic process. Snap-shots of the pulse are shown with propagation. The FF is partially converted to its SH and then back-converted. Solid (dashed) lines are for the case of nonzero (zero) group-velocity mismatch, which causes the back-converted SH field to lag/lead the FF.

However, if the process is *phase-mismatched* a part of the FF energy evolves back and forth between the FF and SH fields periodically, but the majority of the energy remains in the FF. This two-frequency interaction is very important: due to the variation of a material's refractive index with frequency, different frequencies experience different phase- and group-velocities, and the energy which undergoes conversion to the SH and subsequent back-conversion to the FF imparts some of the SH properties to the FF. Under appropriate conditions this leads to a *non-instantaneous* nonlinear phase imposed on the FF. Since the SH can either lag or lead the FF, so can the phase. This process is illustrated in Fig. 8.2.

The non-instantaneous nature of the nonlinear phase manifests itself spectrally as a shift in the FF. These cascaded frequency shifts are qualitatively similar to frequency shifts from Raman-scattering processes, but contrary to Raman (which

only produces red-shifts), the sign and magnitude of cascaded frequency shifts are controllable. Since cascaded frequency shifts originate in a conversion-back-conversion process, they depend on the phase-mismatch between the FF and SH fields. This dependence can be leveraged in materials where phase-matching is provided by modulating the local effective nonlinearity (quasi-phase matching [19, 20]) — an extrinsic property of the material which can be engineered to enhance and control the resulting frequency shifts [16].

8.4.4 Frequency shifted fiber source

Our proposal is to combine cascaded frequency shifting with standard fiber lasers to produce frequency comb sources with the size and stability advantages of fiber lasers, and spectral noise characteristics potentially better than the best solid-state comb sources. This could further increase the measurement limits of frequency metrology and related fields. In addition, since the components for cascaded frequency shifting are very compact and robust, the source could be significantly more portable and stable than those currently available.

Note that cascaded frequency shifting is believed to have spectral noise levels significantly below supercontinuum in microstructured fiber, but they have yet to be verified experimentally — this would be a preliminary goal of this project. The frequency-shifted fiber source (FSFS) will consist of a standard infrared fiber laser, followed by engineered quadratic materials to shift its output spectrum and enable self-referencing (Fig. 8.3).

In the example considered here, the output from a standard ErF at 1550 nm is split into two beams. One beam traverses a piece of the quasi-phase matched quadratic material lithium niobate, aperiodically-poled (aPPLN) to shift spectral

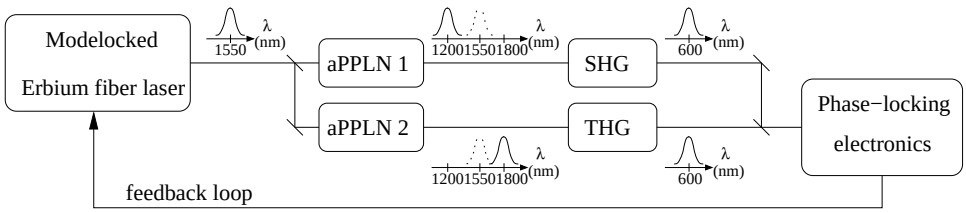

Figure 8.3: Frequency shifted fiber source. Light from an ErF is split in two. Half traverses an aperiodically-poled lithium niobate (aPPLN) crystal optimized for 1200 nm output. A subsequent SHG crystal doubles this to 600 nm. A second aPPLN crystal shifts the other half to 1800 nm, followed by a third-harmonic generation (THG) stage also producing 600 nm light. The beams at 600 nm are combined to determine the carrier envelope offset phase (f_o).

components to 1200 nm [16]. For typical ErF pulse parameters, my simulations indicate that this is possible in a 5-cm long crystal with a linearly ramped poling period from 35 μm to 19 μm. The frequency components at 1200 nm are then doubled in a PPLN chip with period 9.5 μm, producing a spectrum centered at 600 nm. The estimated efficiency of each stage is $\sim$10%, so several nJ from the ErF should yield >10 pJ (50 μW with 50-MHz repetition rate) of 600 nm output, which is more than that produced with supercontinuum generation [9].

The second beam traverses a 5-cm aPPLN crystal poled from 35 μm to 40 μm to shift spectral components to 1800 nm. Since direct frequency tripling is not possible, this 1800 nm light first traverses a PPLN crystal poled at 24.9 μm for SHG (900 nm), and then a subsequent PPLN sample poled at 10.35 μm to generate 600 nm light through sum-frequency mixing of 1800 nm and 900 nm. Though less efficient then the first leg, this should produce 0.1-1 μW of 600 nm light, which is more than sufficient for self-referencing.

These independent 600 nm beams are subsequently combined to determine f_o. Depending on the mode quality, single-mode fiber (SMF) may be used to improve the spatial overlap. The electronics required for this measurement, and for the subsequent feedback loop to stabilize the ErF, are similar to those demonstrated in previous experiments [9, 13, 14]. Once the self-referencing is complete, several options exist for the source: the ErF output can be used directly without shifting. If bandwidths beyond the ErF's 50-100 nm are necessary, some of the frequency shifted components can be used. Alternatively, the output could be broadened *somewhat* in a microstructured fiber (but to significantly less than an octave), to provide a broader spectrum (frequency comb) without introducing the noise levels associated with octave broadening.

Fig. 8.3 depicts seperate frequency shifting and doubling (or tripling) crystals. However, lithium niobate is poled with lithographically produced masks [19, 20] which are highly customizable. Hence, it should be possible to pole a single crystal to perform all of the functions of both legs, making for a very simple experimental setup. This process should also apply to wavelengths other than 1550 nm, in particular the 1030-1060 nm ytterbium band, where high energy [21] and all-fiber [22] oscillators have recently been demonstrated. In addition, the FSFS design should work equally well with nJ energy pulses from an unamplified laser (discussed here), and with higher energy amplified pulses: the amplified case can be carried out in bulk PPLN, whereas nJ level energies require waveguided structures [23] for their high nonlinearity.

Ideally, fiber sources would approach the 1-GHz repetition rates available with Ti:s frequency comb sources. Fiber lasers with 50-100 MHz repetition rates have been demonstrated. Reaching higher repetition rates requires shorter cavities, but

fundamental limits placed on cavity length due to gain and pulse-shaping dynamics makes repetitions rates beyond 400-500 MHz unfeasible. So, while cascaded frequency shifted fiber sources in the several hundred MHz range will hopefully be realized, it is not likely that they will reach (or surpass) solid-state laser repetition rates. However, cascaded-frequency shifting presents another possibility: microchip lasers producing picosecond pulses at up to 2.5 GHz exist [24], but with pulse energies too low for cascaded frequency shifting. However, amplification of low energy pulses in single-mode ytterbium fiber was recently demonstrated with little pulse quality degradation [25]. While beyond the scope of this proposal, such a system utilizing the results developed here might produce integrated fiber frequency comb sources with very high repetition rates.

8.4.5 Summary

In summary, a frequency shifted fiber source is proposed utilizing the recently developed technique of cascaded frequency shifting to produce coherent femtosecond frequency combs for applications ranging from frequency metrology and optical clocks to ultra-dense wavelength division multiplexing and optical frequency synthesis. This source avoids the problems associated with supercontinuum generation in microstructured fiber (which all demonstrated fiber sources rely on for octave-spanning spectra), and would be much more compact than solid-state sources. Femtosecond frequency comb sources must be more compact and stable if they are to find widespread use, particularly outside research laboratories, and the source proposed here is a significant step towards this goal.

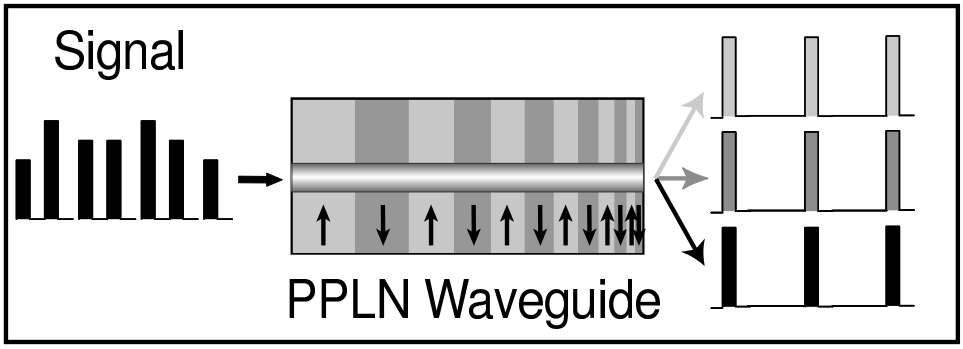

Figure 8.4: Schematic diagram of an intensity dependent wavelength division multiplexing channel switching device.

8.5 Applications for cascaded frequency shifts to devices for optical communications

Controllable nonlinear frequency shifts from non-stationary cascaded processes have a number of direct applications for optical communications and switching devices in materials with large enough nonlinearity that these processes can occur with picojoule to nanojoule pulse energies as demonstrated in Chapters 5 and 6.

While the full range of potential applications is largely unexplored, several simple devices can be envisioned which demonstrate the basic abilities of these processes. For example, a simple intensity to wavelength switching device is depicted in Fig. 8.4. Such a device uses the generation of clean frequency shifts of $\gtrsim$1.5 nm (*c.f.*, Chapter 5) to efficiently switch between wavelength-devision-multiplexing channels. Since the details of these shifts are hugely customizable through engineering of the material used, these shifts are applicable to all common bands used currently for optical communications (*i.e.*, erbium C- and L-bands, etc.) in addition to other wavelengths not yet in use.

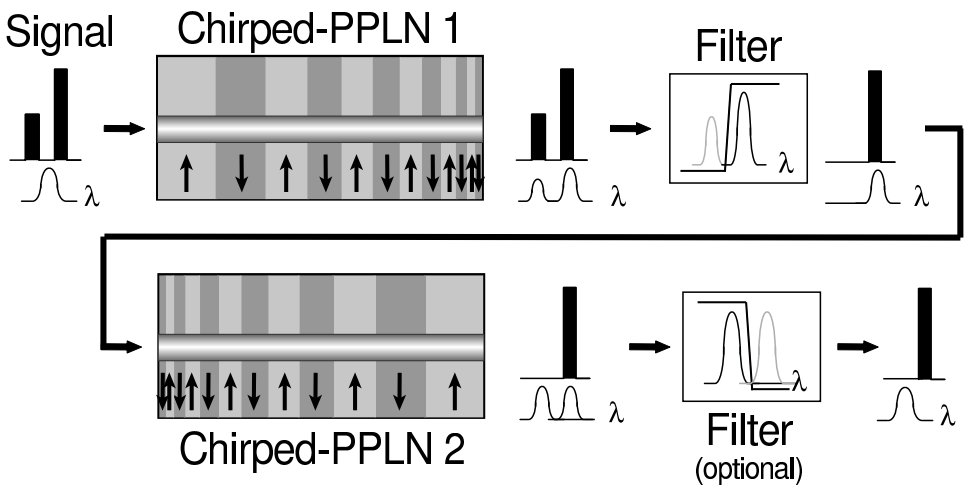

Figure 8.5: Schematic diagram of cascadable (*i.e.*, zero net shift), high extinction ratio discrimination device.

A slightly more complicated scheme (Fig. 8.5) yields a device capable of high extinction ratio discrimination. Here the spectrum of a signal of interest is shifted by a larger amount then that of a lower intensity satellite pulse (or noise). A spectral filter then selectively passes the desired component. Also, a subsequent stage can shift the pulse spectrum back to the initial frequency, providing increased discrimination contrast and the ability to daisy-chain (cascade) such devices. While there is some loss inherent to this scheme, it could easily be integrate with amplification. There is a dearth of high quality, high extinction ratio and ultrafast optical discriminators, so such a device could be of immediate use for various communications systems.

BIBLIOGRAPHY

[1] Y. Silberberg, Opt. Lett. **15**, 1282 (1990).

[2] P. E. Powers, Thomas J. Kulp, and S. E. Bisson, Opt. Lett. **23**, 159 (1998).

[3] S.A. Diddams, A. Bartels, T.M. Ramond, C.W. Oates, S. Bize, E.A. Curtis, J.C. Bergquist, L. Hollberg, IEEE J. Sel. Top. Quantum Electron. **9** 1072 (2003).

[4] S.A. Diddams, Th. Udem, J.C. Bergquist, E.A Curtis, R.E. Drullinger, L. Hollberg, W.M. Itano, W.D. Lee, C.W. Oates, K.R. Vogel, and D.J. Wineland, Science **293**, 825 (2001).

[5] J. Reichert, R. Holzwarth, Th. Udem, and T.W. Hänsch, Opt. Commun. **172**, 59 (1999).

[6] J.K. Ranka, R.S. Windeler, and A.J. Stentz, Opt. Lett. **25**, 25 (2000).

[7] D.J. Jones, S.A. Diddams, J.K. Ranka, A. Stentz, R.S. Windeler, J.L .Hall, and S.T. Cundiff, Science **288**, 635 (2000).

[8] S.A. Diddams, D.J. Jones, J. Ye, S.T. Cundiff, J.L. Hall, J.K. Ranka, R.S. Windeler, R. Holzwarth, T. Udem., and T.W. Hänsch, Phys. Rev. Lett. **84**, 5102 (2000).

[9] B.R. Washburn, S.A. Diddams, N.R. Newbury, J.W. Nicholson, M.F. Yan, and C.G. Jorgensen, Opt. Lett. Opt. Lett. **29**, 250 (2004).

[10] L. Hollberg, C.W. Oates, E.A. Curtis, E.N. Ivanov, S A. Diddams, Th. Udem, H.G. Robinson, J.C. Bergquist, R.J. Rafac, W.M Itano, R.E. Drullinger, and D.J. Wineland, IEEE J. Quantum Electron. **37**, 1502 (2001).

[11] K.L. Corwin, N.R. Newbury, J.M Dudley, S. Coen, S.A. Diddams, K. Weber, and R.S. Windeler, Phys. Rev. Lett. **90**, 113904 (2003).

[12] R. Ell, U. Morgner, F.X. Kärtner, J.G. Fujimoto, E.P. Ippen, V. Scheuer, G. Angelow, and T. Tschudi, Opt. Lett. **26**, 373 (2001).

[13] A. Bartels and H. Kurz, Opt. Lett. **27**, 1839 (2002).

[14] T.M. Ramond, S.A. Diddams, L. Hollberg, and A. Bartels, Opt. Lett. **27**, 1842 (2002).

[15] F. Ö. Ilday, K. Beckwitt, Y.-F. Chen, H. Lim, F. W. Wise, J. Opt. Soc. Am. B **21**, 376 (2004).

[16] K. Beckwitt, F. Ö. Ilday, and F. W. Wise, Opt. Lett. **29**, 763 (2004).

[17] K. Beckwitt, J. A. Moses, F. Ö. Ilday, F. W. Wise, J. Nees, E. Power, K. H. Hong, B. Hou, and G. Mourou, "Cascade-Raman soliton compression with 30-fs, terawatt pulses," presented at the conference on Nonlinear Guided Waves and Their Applications, Toronto, Canada, 28-31 Mar. 2004.

[18] K. Beckwitt, F. Ö. Ilday, F. W. Wise, W. Grundkötter, and W. Sohler, Opt. Lett. (submitted for publication).

[19] M.M. Fejer, G.A. Magel, D.H. Jundt, and R.L. Byer, IEEE J. Quantum Electron. **28**, 2631 (1992).

[20] E.J. Lim, M.M. Fejer, and R.L. Byer, Electron. Lett. **25**, 174 (1989).

[21] F.Ö. Ilday, J.R. Buckley, H. Lim, and F.W. Wise, Opt. Lett. **28**, 365 (2003).

[22] H. Lim, F.Ö. Ilday, and F.W. Wise, Opt. Exp. **10**, 1502 (2002).

[23] E.J. Lim, H.M. Hertz, M.L. Bortz, and M.M. Fejer, Appl. Phys. Lett. **59**, 2207 (1991).

[24] For example the *Lynx* laser from Time-Bandwidth Products, Inc.

[25] F.Ö. Ilday, H. Lim, J. Buckley, and F.W. Wise, Opt. Lett. **28**, 362 (2003).

Chapter 9

Conclusion

This thesis presents original works on the propagation of ultrashort laser pulses in quadratic nonlinear materials. Results are shown in several areas of research: direct compensation of nonlinear phase shifts from Kerr media with negative Kerr-like cascaded phase shifts; progress toward generation of quadratic solitons in systems supporting stable multidimensional soliton formation; and development and demonstration of a new type of cascaded interaction — nonlinear frequency shifts from non-stationary cascaded quadratic process.

Theoretically, we present and analyze a quadratic optical system (poled lithium niobate at wavelengths between 3 and 5 μm) which numerically supports temporal and spatiotemporal soliton formation with the possibility of extension to fully confined solitons. This is currently the only experimentally realizable system to theoretically support light-bullet formation, and opens the door to experiments into the formation, propagation, and interactions of these highly nonlinear phenomena with great potential applications to optical communications and logic.

To date, all applications of cascaded quadratic processes (including those presented above) occur in the limit where the effects of group-velocity mismatch between the coupled fields is small: the limit in which a controllable Kerr-like nonlinear phase-shift is generated. The noninstantaneous, nonlinear frequency shifting processes developed and demonstrated here in some sense opens the door to half of the parameter space of quadratic interactions with significant group-velocity mismatch. We present experiments demonstrating the applicability of these frequency shifting processes to systems ranging from high power (millijoule and higher en-

ergy amplified lasers) to picojoule and nanojoule fiber systems. Fundamentally, these nonlinear frequency shifting processes have a wide variety of applications. Since these processes are possible in materials with self-defocusing nonlinearity and low loss, they enable use with high energy, ultrashort pulses which would otherwise induce material damage with self-focusing nonlinearities. Technologically, they also enable compact and robust short-pulse infrared sources, and low-energy frequency shifting devices. Fundamentally, however, these are new processes and their applications largely remain to be explored.

Appendix A

Coupled equations for phase-mismatched second-harmonic generation with short pulses[1]

The fundamental equations governing the physics described in this thesis are those of phase-mismatched second harmonic generation (SHG) with ultra short pulses. In particular, the effects of group-velocity dispersion (GVD) and group-velocity mismatch (GVM) between the fundamental (FF) and second-harmonic (SH) frequencies in time, diffraction and walk-off in space, and quadratic ($\chi^{(2)}$) and cubic ($\chi^{(3)}$) nonlinearity must be accounted for and understood.

Within the slowly varying envelope and paraxial approximations, the coupled equations governing the evolution of the FF (A_1) and SH (A_2) field envelopes propagating in the z direction and assumed constant in the x direction are [1, 2, 3]

$$\begin{aligned}(\frac{\partial}{\partial z} + \frac{i}{2}\frac{Z_I}{L_{\mathrm{DS},1}}\frac{\partial^2}{\partial t^2} - \frac{i}{2}\frac{Z_I}{L_{\mathrm{DF},1}}\frac{\partial^2}{\partial y^2})A_1 \\ = iA_1^* A_2 e^{i\Delta k(Z_I z)} + i\frac{Z_I}{L_{\mathrm{NL},1}}(\alpha|A_1|^2 + \beta|A_2|^2)A_1,\end{aligned} \tag{A.1}$$

$$\begin{aligned}(\frac{\partial}{\partial z} + \frac{i}{2}\frac{Z_I}{L_{\mathrm{DS},2}}\frac{\partial^2}{\partial t^2} - \frac{1}{L_{\mathrm{GVM}}}\frac{\partial}{\partial t} - \frac{i}{2}\frac{Z_I}{L_{\mathrm{DF},2}}\frac{\partial^2}{\partial y^2})A_2 \\ = i\frac{n(\omega_1)}{n(\omega_2)}A_1 A_1 e^{-i\Delta k(Z_I z)} + i\frac{n(\omega_1)}{n(\omega_2)}\frac{Z_I}{L_{\mathrm{NL},2}}(\beta|A_1|^2 + \alpha|A_2|^2)A_2,\end{aligned} \tag{A.2}$$

[1]These equations are generally known, but were derived in detail *in standard electrostatic units* by K. Beckwitt and J. Harbold. This note exists in the Wise Group literature and appears in K.B.'s notebooks.

where

$$L_{\mathrm{DS},j} = \frac{\tau_0^2}{\mathrm{GVD}(\omega_\mathrm{j})}, \tag{A.3}$$

$$L_{\mathrm{DF},j} = \frac{2\pi y_0^2}{\lambda_j}, \tag{A.4}$$

$$L_{\mathrm{NL},j} = \frac{c}{\omega_j n_2 I_0}, \tag{A.5}$$

$$L_{\mathrm{GVM}} = \frac{\tau_0}{\mathrm{GVM}}, \tag{A.6}$$

$$I_0 = \frac{nc}{8\pi}|A_1(0)|^2, \tag{A.7}$$

$$Z_I = \frac{n\lambda_1}{2\pi d_{\mathrm{eff}} A_1(0)}. \tag{A.8}$$

Here time t is normalized to the initial $1/e$ pulse width τ_0, related to the full-width at half-maximum (FWHM) pulse width by $\tau_0 = 0.6\ \tau_{\mathrm{FWHM}}$. A_1 and A_2 are in units of the initial peak FF field A_0 (related to the initial peak FF intensity by A.7) and n_2 is the Kerr nonlinear index. The cubic nonlinear length characterizing the pulse propagation (A.5) is the length over which the accumulated nonlinear phase shift is 1 for frequency ω_j with $j = 1, 2$. The parameters α and β describe the relative strengths of self- and cross-phase modulation from $\chi^{(3)}$, and depend on the relative field polarizations (for parallel polarizations $\alpha = 1$ and $\beta = 2$ and for orthogonal polarizations $\alpha = 1$ and $\beta = 2/3$). The propaga-

tion coordinate z is normalized to the quadratic nonlinear length Z_I (A.8) which characterizes the strength of the nonlinear coupling in a materials with effective quadratic nonlinear coefficient d_{eff}. Z_I is related to the quadratic nonlinear phase-shift through $\Delta\Phi_{\text{NL}}^{\chi^{(2)}} = (L/Z_I)^2/\Delta kL$ in the limit of large phase-mismatch [4], where $\Delta k = k_{2\omega} - 2k_{\omega}$. In terms of the group refractive indices for the FF and SH ($n_{g,1}$ and $n_{g,2}$, respectively), GVM $= (n_{g,1} - n_{g,2})/c$.

In Eqs. (A.1) and (A.2) the field is assumed to be constant along the x direction. However, these equations could easily be generalized to their full three-dimensional counterparts by addition of the appropriate diffraction term

$$-\frac{i}{2}\frac{Z_I}{L_{\text{DFx},j}}\frac{\partial^2 A_j}{\partial x^2}, \tag{A.9}$$

to each equation, with $L_{\text{DFx},j} = 2\pi x_0^2/\lambda_j$.

In the case of quasi-phase matching, the sign of the second order nonlinear length Z_I switches depending on whether you are in the region of positive ($+d_{\text{eff}}$) or negative ($-d_{\text{eff}}$) effective second order nonlinearity.

BIBLIOGRAPHY

[1] A. A. Kanashov and A. M. Rubenchik, Physica D **4**, 122 (1981).

[2] B. A. Malomed, P. Drummond, H. He, A. Berntson, D. Anderson and M. Lisak, Phys. Rev. E **56**, 4725 (1997).

[3] X. Liu, K. Beckwitt, and F. W. Wise, Phys. Rev. E **22**, 1328 (2000).

[4] R. DeSalvo, D. J. Hagan, M. Sheik-Bahae, G. Stegeman, E. W. Van Stryland, and H. Vanherzeele, Opt. Lett. **17**, 28 (1992).

Appendix B

Pulse propagation simulations

B.0.1 Numerical framework

To solve Eqs. (A.1) and (A.2) numerically we use a symmetric split-step beam propagation method [1, 2, 3] in which the full coupled equations are divided into a linear part

$$(\frac{\partial}{\partial z} + \frac{i}{2}\frac{Z_I}{L_{\mathrm{DS},1}}\frac{\partial^2}{\partial t^2} - \frac{i}{2}\frac{Z_I}{L_{\mathrm{DF},1}}\frac{\partial^2}{\partial y^2})A_1 = 0, \tag{B.1}$$

$$(\frac{\partial}{\partial z} + \frac{i}{2}\frac{Z_I}{L_{\mathrm{DS},2}}\frac{\partial^2}{\partial t^2} - \frac{1}{L_{\mathrm{GVM}}}\frac{\partial}{\partial t} - \frac{i}{2}\frac{Z_I}{L_{\mathrm{DF},2}}\frac{\partial^2}{\partial y^2})A_2 = 0, \tag{B.2}$$

and a nonlinear part

$$\frac{\partial A_1}{\partial z} = iA_1^* A_2 e^{i\Delta k(Z_I z)} + i\frac{Z_I}{L_{\mathrm{NL},1}}(\alpha|A_1|^2 + \beta|A_2|^2)A_1, \tag{B.3}$$

$$\frac{\partial A_2}{\partial z} = i\frac{n(\omega_1)}{n(\omega_2)}A_1 A_1 e^{-i\Delta k(Z_I z)} + i\frac{n(\omega_1)}{n(\omega_2)}\frac{Z_I}{L_{\mathrm{NL},2}}(\beta|A_1|^2 + \alpha|A_2|^2)A_2. \tag{B.4}$$

To obtain a general solution for Eqs. (A.1) and (A.2) each propagation step Δz is divided into three operations (schematic in Fig. B.1): solution of the linear part [Eqs. (B.1) and (B.2)] on the first half of the step (from $z_0 \rightarrow z_0 + \Delta z/2$), solution of the nonlinear part [Eqs. (B.3) and (B.4)] on over the full step ($z_0 \rightarrow z_0 + \Delta z$) using the linearly propagated fields at $(z_0 + \Delta z/2)$, and solution of the linear part

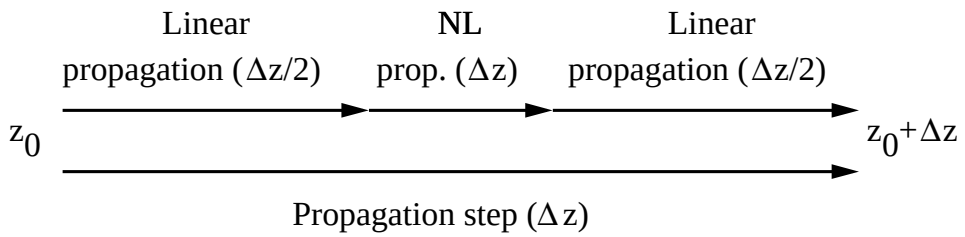

Figure B.1: Schematic of a simulated propagation step from $z_0 \rightarrow z_0 + \Delta z$.

over the second half of the step ($z_0 + \Delta z/2 \rightarrow z_0 + \Delta z$). In this way the nonlinear propagation is solved with the average linear propagation on each step (as opposed to the fields at either step boundary), which effectively increases the accuracy of the numerical solution on that step [3].

The solution to the linear equations is easily obtained analytically in the frequency domain, where

$$\tilde{A}_1(z_0 + \Delta z, f, f_y) = \tilde{A}_1(z_0, f, f_y) \exp\left[i\Delta z(2\pi)^2 \left(\frac{f^2}{2L_{\mathrm{DS},1}} - \frac{f_y^2}{2L_{\mathrm{DF},1}}\right)\right], \tag{B.5}$$

$$\tilde{A}_2(z_0 + \Delta z, f, f_y) = \tilde{A}_2(z_0, f, f_y) \exp\left[i\Delta z(2\pi)^2 \left(\frac{f^2}{2L_{\mathrm{DS},1}} - \frac{1}{2\pi}\frac{f}{L_{\mathrm{GVM}}} - \frac{f_y^2}{2L_{\mathrm{DF},1}}\right)\right]. \tag{B.6}$$

Hence Eqs. (B.1) and (B.2) are solved analytically through a Fourier transform ($\tilde{A}(z, f) = \int \tilde{A}(z, \tau) \exp(2\pi i f \tau) d\tau$) to the frequency domain and application of the solutions in Eqs. (B.5) and (B.6), followed by an inverse transform back to the time domain.

The nonlinear equations, on the on the other hand, can be solved with a stan-

dard fourth-order Runge-Kutta algorithm [3] with interim coefficients

$$k_{11} = i\frac{\Delta z}{Z_I}\exp\left(i\Delta k z_0\right) A_1^*(z_0)A_2(z_0) + i\frac{\Delta z}{L_{\mathrm{NL},1}}\left(\alpha\left|A_1(z_0)\right|^2 + \beta\left|A_2(z_0)\right|^2\right)A_1(z_0), \tag{B.7}$$

$$k_{12} = i\frac{\Delta z}{Z_I}\exp\left(-i\Delta k z_0\right) A_1(z_0)A_1(z_0) + i\frac{\Delta z}{L_{\mathrm{NL},2}}\left(\beta\left|A_1(z_0)\right|^2 + \alpha\left|A_2(z_0)\right|^2\right)A_2(z_0), \tag{B.8}$$

$$k_{21} = i\frac{\Delta z}{Z_I}\exp\left(i\Delta k\left(z_0+\frac{\Delta z}{2}\right)\right)\left(A_1(z_0)+\frac{k_{11}}{2}\right)^*\left(A_2(z_0)+\frac{k_{12}}{2}\right) + i\frac{\Delta z}{L_{\mathrm{NL},1}}\left(\alpha\left|A_1(z_0)+\frac{k_{11}}{2}\right|^2 + \beta\left|A_2(z_0)+\frac{k_{12}}{2}\right|^2\right) \times\left(A_1(z_0)+\frac{k_{11}}{2}\right), \tag{B.9}$$

$$k_{22} = i\frac{\Delta z}{Z_I}\exp\left(-i\Delta k\left(z_0+\frac{\Delta z}{2}\right)\right)\left(A_1(z_0)+\frac{k_{11}}{2}\right)\left(A_1(z_0)+\frac{k_{11}}{2}\right) + i\frac{\Delta z}{L_{\mathrm{NL},2}}\left(\beta\left|A_1(z_0)+\frac{k_{11}}{2}\right|^2 + \alpha\left|A_2(z_0)+\frac{k_{12}}{2}\right|^2\right) \times\left(A_2(z_0)+\frac{k_{12}}{2}\right), \tag{B.10}$$

$$k_{31} = i\frac{\Delta z}{Z_I}\exp\left(i\Delta k\left(z_0+\frac{\Delta z}{2}\right)\right)\left(A_1(z_0)+\frac{k_{21}}{2}\right)^*\left(A_2(z_0)+\frac{k_{22}}{2}\right) + i\frac{\Delta z}{L_{\mathrm{NL},1}}\left(\alpha\left|A_1(z_0)+\frac{k_{21}}{2}\right|^2 + \beta\left|A_2(z_0)+\frac{k_{22}}{2}\right|^2\right) \times\left(A_1(z_0)+\frac{k_{21}}{2}\right), \tag{B.11}$$

$$k_{32} = i\frac{\Delta z}{Z_I}\exp\left(-i\Delta k\left(z_0+\frac{\Delta z}{2}\right)\right)\left(A_1(z_0)+\frac{k_{21}}{2}\right)\left(A_1(z_0)+\frac{k_{21}}{2}\right) + i\frac{\Delta z}{L_{\mathrm{NL},2}}\left(\beta\left|A_1(z_0)+\frac{k_{21}}{2}\right|^2+\alpha\left|A_2(z_0)+\frac{k_{22}}{2}\right|^2\right) \times\left(A_2(z_0)+\frac{k_{22}}{2}\right), \quad \text{(B.12)}$$

$$k_{41} = i\frac{\Delta z}{Z_I}\exp\left(i\Delta k\left(z_0+\Delta z\right)\right)\left(A_1(z_0)+k_{31}\right)^*\left(A_2(z_0)+k_{32}\right) + i\frac{\Delta z}{L_{\mathrm{NL},1}}\left(\alpha\left|A_1(z_0)+k_{31}\right|^2+\beta\left|A_2(z_0)+k_{32}\right|^2\right)\left(A_1(z_0)+k_{31}\right), \quad \text{(B.13)}$$

$$k_{42} = i\frac{\Delta z}{Z_I}\exp\left(-i\Delta k\left(z_0+\Delta z\right)\right)\left(A_1(z_0)+k_{31}\right)\left(A_1(z_0)+k_{31}\right) + i\frac{\Delta z}{L_{\mathrm{NL},2}}\left(\beta\left|A_1(z_0)+k_{31}\right|^2+\alpha\left|A_2(z_0)+k_{32}\right|^2\right)\left(A_2(z_0)+k_{32}\right), \quad \text{(B.14)}$$

and subsequent fields at $z_0+\Delta z$

$$A_1(z_0+\Delta z) = A_1(z_0)+\frac{k_{11}}{6}+\frac{k_{21}}{3}+\frac{k_{31}}{3}+\frac{k_{41}}{6}+O(\frac{\Delta z}{Z_I},\frac{\Delta z}{L_{\mathrm{NL},1}})^5, \quad \text{(B.15)}$$

$$A_2(z_0+\Delta z) = A_2(z_0)+\frac{k_{12}}{6}+\frac{k_{22}}{3}+\frac{k_{32}}{3}+\frac{k_{42}}{6}+O(\frac{\Delta z}{Z_I},\frac{\Delta z}{L_{\mathrm{NL},2}})^5. \quad \text{(B.16)}$$

This process is then repeated over the entire propagation length of interest, resulting in a numerical solution for Eqs. (A.1) and (A.2) that is both efficient and computationally fast. In addition, since the Runge-Kutta algorithm for the nonlinear solution is easily parallelized, and relatively efficient parallel implementations of Fast-Fourier Transform codes exist [4], these methods are directly implementable in parallel architectures both for increased speed and to make solutions of more

complicated structures and longer propagation feasible.

It should be noted that Eqs. (A.1) and (A.2) are written in a frame moving at the group velocity of the FF. This is easily altered by adding a GVM term to Eq. (A.1) for the FF and adjusting the relative velocity mismatch terms between the FF, SH, and the moving frame. In some situations (*i.e.*, where the SH walks away a significant amount during propagation) it is convenient numerically to use a window which moves at the weighted average of the FF and SH group velocities, so as to allow a smaller simulated time window to catch all the relevant dynamics.

B.0.2 Layout

A flowchart of the code organization appears in Fig. B.2. The output intensity, phase, and spectral profiles are calculated and saved for each output page. The full fields are only saved at a single specified propagation step, which can be used to continue propagation in subsequent simulations.

B.0.3 Architecture and dependencies (*i.e.*, running the code)

The code is written in C with two external dependencies: FFTW [4] and Matlab. However, Matlab is only required for its C libraries allowing output to its proprietary data format for subsequent visualization (performed with several plot_*.m Matlab routines included with the code: *i.e.*, plot_trends.m, plot_profiles.m, etc.). As such, it is simple to write the datafile generation procedure write_datafile.c to implement text (or any other format) output, in which case Matlab is not necessary (this is implemented for plain text output in write_datafile_text.c, which is hugely inefficient for data storage and manipulation).

In its current structure, the code is suitable for use in i386 compatible architec-

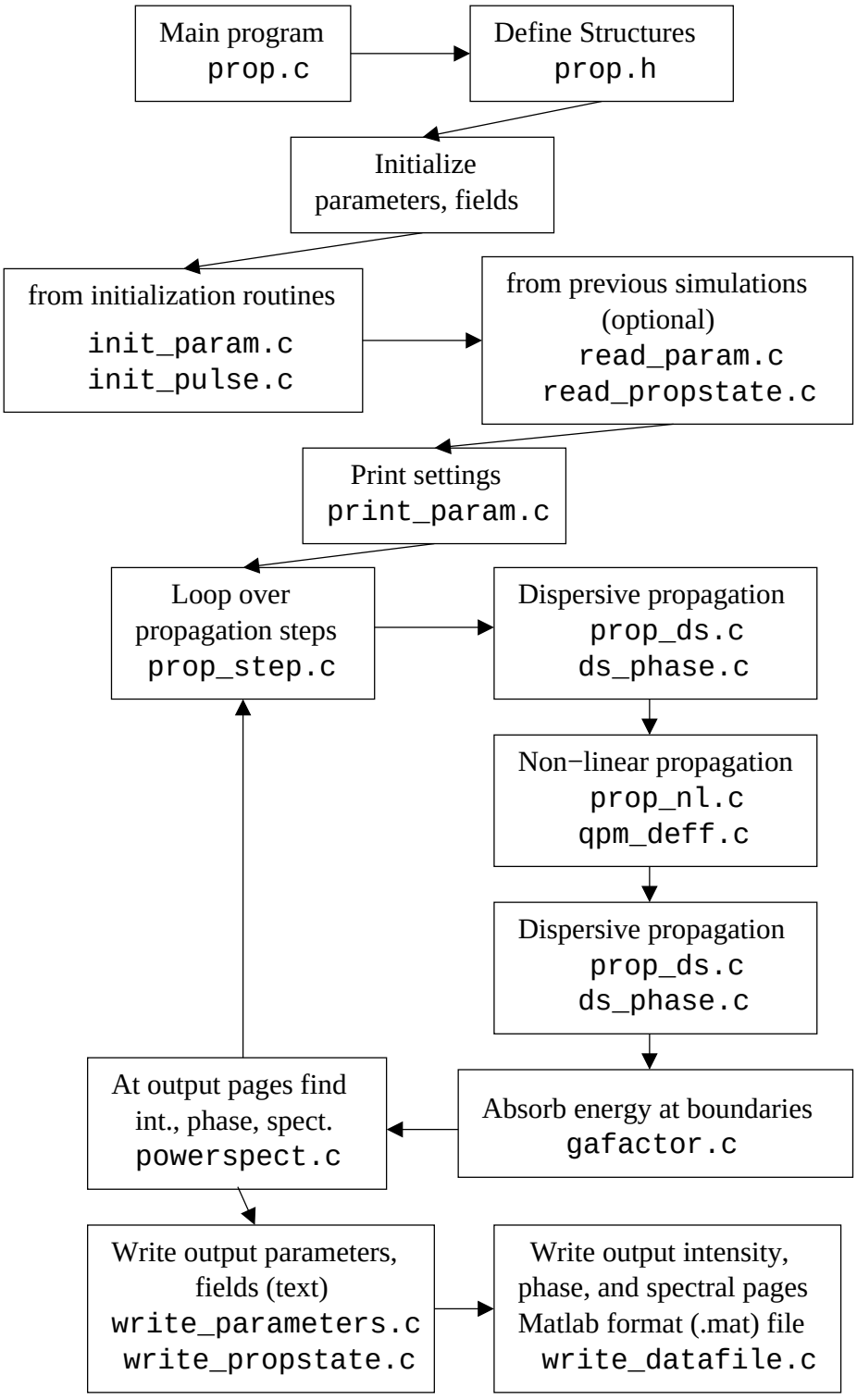

Figure B.2: Simulation flowchart.

tures running any of the standard Linux distributions (development was on Redhat 7.x - 9.x). A standard makefile appears in Section B.0.4. If Matlab and FFTW are installed, and proper paths to their libraries appear in the linker path (stored in /etc/ld.so.conf under Redhat, with ld reinitialized by /sbin/ldconfig) then the only explicit dependence for building the code is that MATLIBDIR point to the default Linux Matlab libraries (*i.e.*, MATLIBDIR = /usr/local/matlab/extern/lib/glnx86/ for a default install under Redhat 7.x-9.x). It is also possible to compile the code without a full installation of Matlab and FFTW: in this case the proper libraries should be placed in a directory pointed to by MATLIBDIR, and the linker parameters should be set to LDFLAGS = -Wl,-rpath,$(MATLIBDIR). In the implementation appearing here, the code assumes FFTW version 2.1.x. Version 3.x of FFTW has recently been released, but its implementation requires modification to these simulations.

When running the code, some care should be taken to assure grid dimensions appropriate to the problem being solved. Generally one wants a number of Δz steps per SH conversion-back-conversion cycle ($\sim 2\pi/\Delta k$). In addition, if the material being simulated has longitudinal structure (*i.e.*, for quasi-phase-matching), then at least $\sim$5 Δz steps are required in the shortest characteristic length of the structure.

In the transverse dimensions (time and any spatial dimensions included), it is not trivial to find the proper combination of grid and pulse dimensions: one needs a large enough window that all the dynamics are captured without boundary effects obscuring the process and a large enough number of grid points across the pulse that fine structure is properly simulated. At the same time, it is necessary to have a small enough number of points in the pulse (compared to the window size) that the spectrum of the pulse is not clipped and small enough window sizes that the

simulation requirements are reasonable computationally.

On a ∼2 GHz Pentium 4 or Athlon XP class machine simulation of bulk 1D problems takes minutes. Simulation of bulk 2D systems takes minutes to hours, and full 3D bulk simulations take $\gtrsim$1 day. Addition of longitudinal structure is typically equivalent to adding another transverse dimension in processing time (*i.e.*, days for an accurate 2D QPM simulation). Finally, 2D simulations with longitudinal structure and bulk 3D simulations typically require 1-2 GB of RAM.

Generally it must be recognized that split-step FFT schemes are very susceptible to false stabilization of the simulated fields (due to a number of factors including FFT filtering and window boundary effects) — and care must be taken to ensure that simulations are accurate: *e.g.*, one must investigate the dependencies on window size in all dimensions and the stability of suspected solutions to perturbations in intensity, among many other numerical and physical parameters.

Both single and multiple processor versions of the pulse propagation code exist. The parallel architecture version of the simulation is not discussed here in detail, but is written under MPI and assumes both a parallel version of FFTW 2.1.x and visual C++ under Microsoft Windows as is implemented at the Cornell Theory Center. Empirically, optimal efficiency occurs with 8-16 nodes for simulations involving $\sim O(10^8)$ grid points, as is reasonable for (2+1) dimensional simulations of QPM structures, or full three-dimensional simulations of bulk materials. Without unnecessary resolution, these types of simulations take ∼24-hours with a reasonable number of nodes.

B.0.4 Linux makefile

```
# Makefile for 3D propagation simulation. KB.
MATLIBDIR = /usr/local/matlab/extern/lib/glnx86/
```

```
TAREXCLUDEFILE = exclude_from_tar.tmp
CC      = gcc
CFLAGS  = -g -O2 # for debugging/profiling add -pg
# LIBS  = -L$(MATLIBDIR) -I$(MATLIBDIR) -lrfftw -lfftw -lmat -lmx -lm
LIBS    = -L$(MATLIBDIR) -lrfftw -lfftw -lmat -lmx -lm
INCLS   =
OBJECTS = gafactor.o init_param.o init_pulse.o powerspect.o \
        prop.o prop_ds.o prop_nl.o prop_step.o c_arith.o \
        row_major.o write_datafile.o ds_phase.o write_propstate.o \
        read_propstate.o read_parameters.o write_parameters.o \
        print_param.o adv_field_page.o date_str.o qpm_deff.o
TARGET = sim.exe
# LDFLAGS = -Wl,-rpath,$(MATLIBDIR)
LDFLAGS =

$(TARGET): $(OBJECTS)
        @echo "Linking executable..."
        $(CC) $(CFLAGS) $(INCLS) -o $(TARGET) $(OBJECTS) $(LDFLAGS) $(LIBS)
        @echo "Complete!"

clean:
        @echo "Cleaning temporary files..."
        @rm -f *.o *.*~ *~ \#* .\#* core *.txt $(TARGET) a.out data.mat \
        gmon.out propstate.dat temp.tif parameters.dat # /tmp/file*

backup:
        @echo "Backing up source code..."
        @tar -c -v -z -f codebackup_current.tgz \
        --exclude codebackup_current.tgz ./*
        @rm -f $(TAREXCLUDEFILE)
```

BIBLIOGRAPHY

[1] J.-Y. Zhang, J. Y. Huang, H. Wang, K. S. Wong, and G. K. Wong, J. Opt. Soc. Am. B **15**, 200 (1998).

[2] X. Liu, K. Beckwitt, and F. W. Wise, Phys. Rev. E **62**, 1328 (2000).

[3] W. H. Press, B. P. Flannery, S. A. Teukolsky, and W. T. Vetterling, *Numerical Recipes in C: The Art of Scientific Computing (2nd edn.)* (Cambridge University Press: Cambridge, 1992).

[4] for example the excellent FFTW, available at www.fftw.org.

Appendix C

Optical parametric amplifiers for 3-5 μm pulse generation

C.1 Soliton stability window

There is only a small window for the potential observation of solitons in quadratic materials without external group-velocity dispersion modification through pulse tilting. The region (schematically depicted in Fig. C.1) is bounded from above by linear (one-photon) absorption present in all optical media in the infrared. In lithium niobate this absorption edge is near 5 μm. From below, the group-velocity dispersion decreases with increasing wavelength with the transition from normal (positive) to anomalous (negative) dispersion typically occurring near 2 μm. So, anomalous dispersion of significant magnitude at the fundamental frequency coupled with anomalous or small and normal group-velocity dispersion at the second-harmonic frequency requires working at longer wavelengths. For lithium niobate the zero-point in group-velocity dispersion occurs near 1.9 μm, which practically requires experiments to be performed at wavelengths $\gtrsim$3.5 μm. Finally, group-velocity mismatch between the fundamental and second-harmonic frequencies increases from negative to positive, with the zero point for lithium niobate occurring near 2.5 μm. Near 4 μm, the magnitude of the group-velocity mismatch becomes large enough that limited soliton acceptance due to excessive group-velocity mismatch becomes an issue.

As shown in Chapter 3, a windows does exist where temporal soliton formation appears possible in periodically poled lithium niobate near 4 μm, and this window

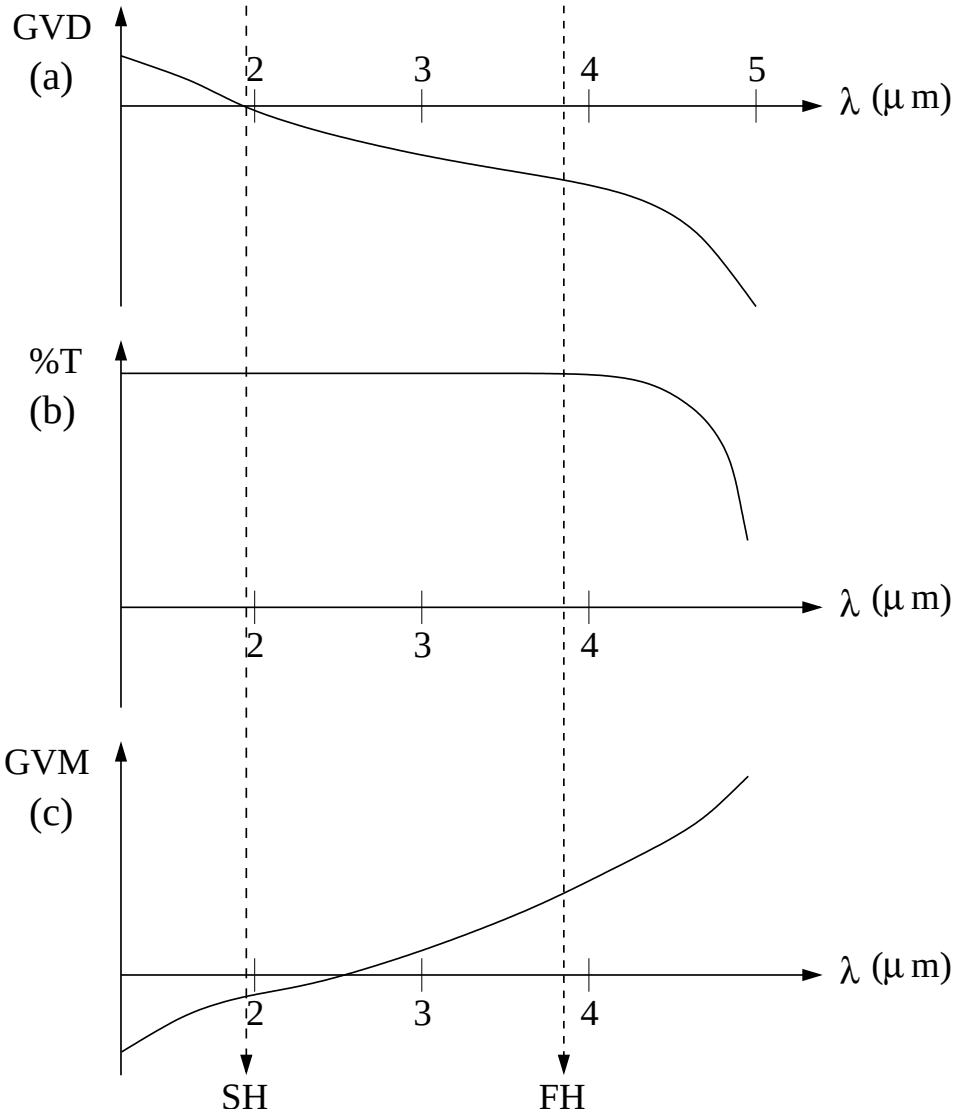

Figure C.1: Schematic of the group-velocity dispersion (a), transmission (b), and group-velocity mismatch (c) of lithium niobate and similar quadratic materials in the infrared.

appears to shrink but remains open for spatiotemporal solitons with two- and three-dimensions of confinement [1, 2].

Furthermore, the pulse parameter requirements are very stringent: currently available periodically poled lithium niobate crystals are limited to ∼5 cm lengths, which necessitates pulses ≲200 fs in duration to observe several characteristic lengths of the soliton evolution; furthermore, both soliton formation, and convincing demonstration of their formation are critically dependent on not having excess spectral bandwidth in the input pulse. Experimentally, this means the source pulses used must be near Fourier-transform limited (in practice ≲20% beyond transform limit is sufficient). Finally, solitons are manifestly dynamical interactions of high peak power pulses and nonlinear media. Consequently, pulse energies of several microjoules are required for temporal (one-dimensional) soliton formation, with somewhat less for two- and three-dimensional solitons.

C.2 Optical parametric amplification

Unfortunately, no laser gain media suitable for short pulse operation exist on the 2-4 μm wavelength region. However, titanium:sapphire amplified lasers are now an established technology that produce millijoule energy, 100 fs, and near transform limited pulses at wavelengths around 800 nm. Building on these systems, wavelengths near 4 μm are accessible through optical parametric amplification: a process by which a high energy photon is converted through a second order nonlinear interaction into two lower energy photons. Since this process must conserve both energy and momentum, the energy ratio of the product photons can be controlled through the details of the phase matching process in the nonlinear crystal used. In these processes the input photon is called the "pump," and the higher

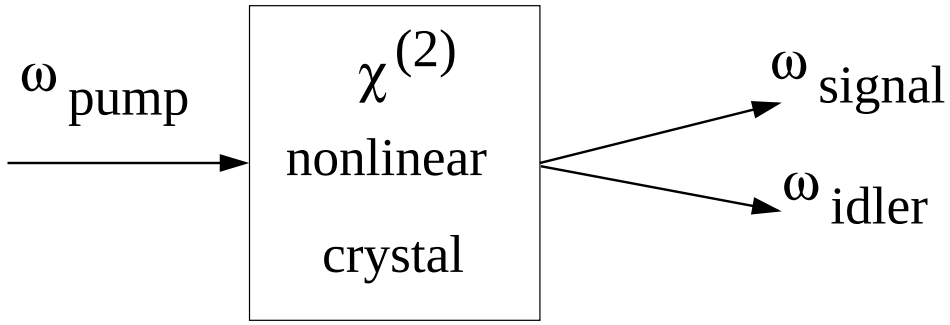

Figure C.2: Schematic of the optical parametric amplification processes.

energy and lower energy product photons are called the "signal" and the "idler," respectively (Fig. C.2).

The relation of the photon energies are

$$\omega_{\text{pump}} = \omega_{\text{signal}} + \omega_{\text{idler}}, \tag{C.1}$$

$$\omega_{\text{pump}} > \omega_{\text{signal}} > \omega_{\text{idler}}, \tag{C.2}$$

and practically the phase matching conditions (and hence the energy splitting ratio and signal and idler wavelengths) are controlled by angle tuning of the nonlinear crystal.

For generation of idler frequencies in the 3-5 μm range, several potential nonlinear crystals for optical parametric amplification exist. The approximate wavelength range and energies of the idler from these materials is depicted in Fig. C.3, where in the case of "BBO + DFG" the wavelength range available with beta-barium borate (BBO) is extended with an additional second order nonlinear process (difference frequency generation, DFG) which subtracts the idler photon from the signal pho-

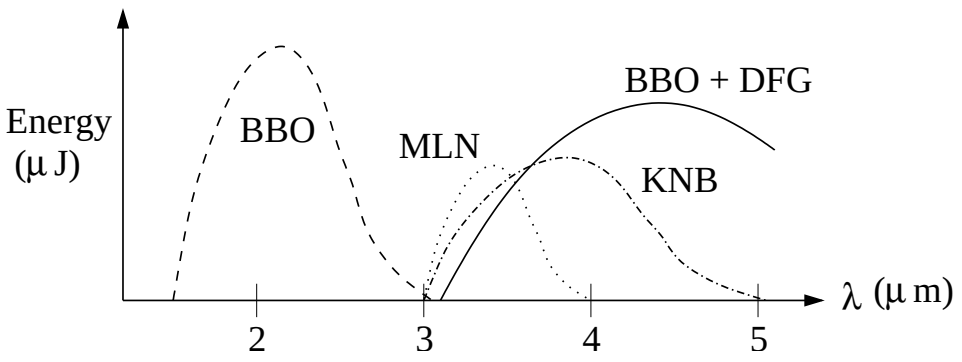

Figure C.3: Schematic wavelength ranges and energies accessible with different optical parametric amplification materials, and associated subsequent nonlinear processes. BBO (dashes, beta-barium borate: β-BaB_2O_4), MLN (dots, magnesium oxide doped lithium niobate, $MgO : LiNbO_3$), and KNB (dash-dots, potassium niobate, $KNbO_3$) indicate the idler wavelength ranges with these materials, and BBO + DFG (solid curve) indicates the tuning range made available by adding a subsequent difference frequency generation (DFG) crystal to the signal and idler output from BBO.

ton, generating their difference which is tunable near 4 μm. The relative merits and performance of these processes are discussed for many different wavelengths and materials in a number of references including: KTA ($KTiOPO_4$) and RTA ($RbTiOAsO_4$) [3, 4, 5], KNB ($KNbO_3$) [6, 7, 8], MLN ($MgO : LiNbO_3$) [9, 10], and through other more complex schemes like difference frequency generation of optical parametric amplifier output [11, 12, 13, 14] based mostly on signal and idler output from BBO [15, 16]. For a review of some of these materials, see Ref. [17].

It should be noted that there are many additional constraints [17] to the processes and materials which will not be covered in detail here. These include: phase matching constraints which limit the available wavelengths and energies from these

materials; signal-pump and idler-pump group-velocity mismatch which limits the bandwidth and pulse width of the generated pulses, and technical issues such as collinear versus non-collinear geometries and type-I versus type-II phase matching conditions (associate with the relative polarizations of the pump and product photons).

C.3 Potassium niobate and its limitations

With all these issues accounted for, two main candidates for the production of $\sim$4 μm pulses emerge: direct idler generation in potassium niobate (KNB), and signal (near 1.3 μm) and idler (near 2.0 μm) generation in BBO followed by difference frequency generation between these wavelengths to generate $\sim$4 μm pulses in $AgGaS_2$.

Due to the apparent simplicity of the processes, we first tried direct generation in KNB. Fig. C.4 shows a sample output idler spectrum and temporal cross-correlation trace between the pump and generated idler for operation near 3 μm.

However, these results are not typical. Experimentally we found KNB to be plagued with numerous problems which prevent experiments with the output pulses. These problems include: poor shot-to-shot noise fluctuations and long-time drift. In addition, while the results shown in Fig. C.4 correspond to a time-bandwidth product of only $\sim$1.5 times transform-limit, typical results were 2-4 times beyond transform-limit. We attribute this mostly to pump pulse spectral broadening due to self-phase modulation from larger than expected n_2 of KNB. We were able to ameliorate this spectral broadening somewhat by reducing the pump intensity, but at the cost of reduced idler energy. In retrospect, it is clear that KNB is still an experimental material, and that several of the published results for

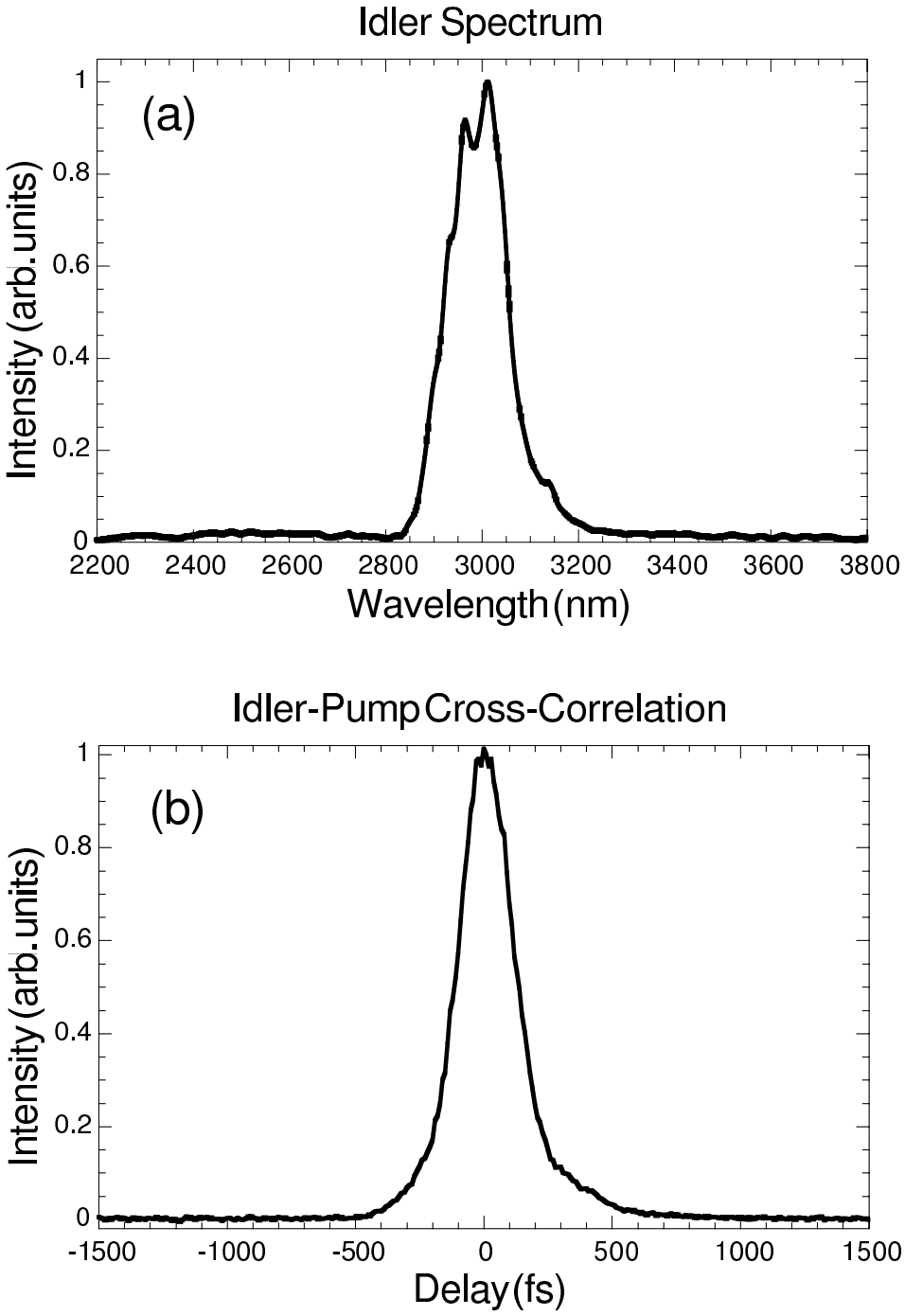

Figure C.4: Sample KNB idler spectrum (a) and temporal cross-correlation trace (b) with the pump which deconvolves to an idler pulse width of ∼180 fs.

pulse energy and quality are "best-case" output and do not reflect daily operating performance (at least in our experience).

C.4 Difference frequency generation

With these issues in mind, we have recently switched to an alternate 4 μm generation scheme based on difference frequency generation in the quadratic nonlinear material $AgGaS_2$ of the signal and idler from a standard BBO optical parametric amplifier. A schematic of this setup appears in Fig. C.5. While more technically complex, this process is well established and has been demonstrated to provide sufficient energy, pulse quality, and stability for highly sensitive nonlinear optics experiments [13].

Fig. C.5 shows the layout of the parametric amplification in BBO and subsequent difference frequency in $AgGaS_2$. Experiments to characterize and eventually observe solitons with this source are currently underway, with initial results indicating several microjoules of difference frequency output tunable between $\sim$3.5 and 4.5 μm.

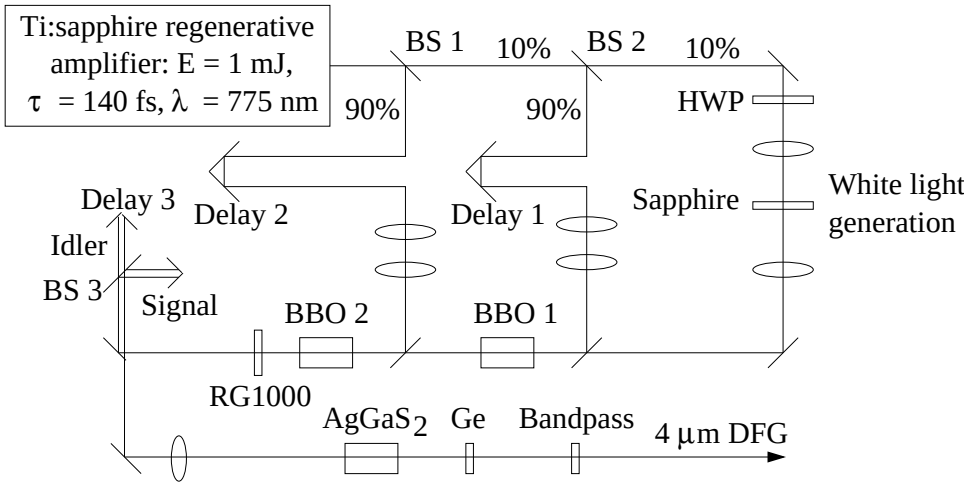

Figure C.5: Layout of the BBO optical parametric amplifier with an additional difference frequency generation stage in $AgGaS_2$. Beamsplitters BS 1 and 2 split off successive fractions of the input energy for preamplification and power amplification stages in BBO. The half-wave plate (HWP), telescope, and sapphire window serve as a white light source to seed the BBO amplification stages. Filter RG1000 passes the amplified signal and idler while blocking the residual unconverted pump light. Delay stages 1 and 2 are used to achieve temporal overlap between the pump paths and the white light seed. After amplification, the signal and idler are separated by BS 3, their temporal overlap is optimized with Delay 3, and they are subsequently recombined and focused down into the DFG crystal. A combination of a germanium (Ge) window and 3-5 μm bandpass filter block the residual signal and idler while passing the converted DFG.

BIBLIOGRAPHY

[1] I. N. Towers, B. A. Malomed, and F. W. Wise, Phys. Rev. Lett. **90** 123902 (2003).

[2] K. Beckwitt, Y.-F. Chen, and F. W. Wise, unpublished results.

[3] D. T. Reid, M. Ebrahimzadeh, and W. Sibbett, J. Opt. Soc. Am. B **12**, 2168 (1995).

[4] J.-C. Wang and J.-K. Wang, "Femtosecond optical parametric amplifiers with collinear phase matching: experiments and full simulation," in Nonlinear Frequency Generation and Conversion: Materials, Devices, and Applications II, K. L. Schepler, D. D. Lowenthal, J. W. Pierce, eds., Proc. SPIE **4972**, 190 (2003).

[5] J.-K. Wang and J. Franken, "Generation of 1-GW, 1-kHz femtosecond mid-infrared laser pulses," presented at the Conference on Lasers and Electro-Optics, San Francisco, USA, 7-12 May, 2000.

[6] J. D. Kafka and M. L Watts, "A potassium niobate OPA pumped by an amplified Ti:sapphire laser," in *Springer Series in Chem. Phys. **62**: Ultrafast Phenom. X*, P. F. Barbara, J. G. Fujimoto, W. H. Knox, and W. Zinth, eds, (Springer-Verlag, Heidelberg, Germany, 1996), pp. 38-39.

[7] V. Petrov and F. Noack, Opt. Lett. **21**, 1576 (1996).

[8] J. A. Gruetzmacher and N. F. Scherer, Rev. of Sci. Instr. **73**, 2227 (2002).

[9] F. Rotermund, V. Petrov, F. Noack, M. Wittmann, and G. Korn, J. Opt. Soc. Am. B **16**, 1539 (1999).

[10] V. Petrov, F. Rotermund, and F. Noack, Appl. Opt. **37**, 8504 (1998).

[11] G. M. Gale, G. Gallot, F. Hache, and R. Sander, Opt. Lett. **22**, 1253 (1997).

[12] F. Seifert, V. Petrov, and M. Woerner, Opt. Lett. **19**, 2009 (1994).

[13] N. Demirdöven, M. Khalil, O. Golonzka, and A. Tokmakoff, Opt. Lett. **27**, 433 (2002).

[14] R. A. Kaindl, M. Wurm, K. Reimann, P. Hamm, A. M. Weiner, and M. Woerner, J. Opt. Soc. Am. B **17**, 2086 (2000).

[15] N. Nisoli, S. De. Silvestri, V. Magni, O. Svelto, R. Danielius, A. Piskarskas, G. Valiulis, and A. Varanavicious, Opt. Lett. **19**, 1973 (1994).

[16] V. V. Yakovlev, B. Kohler, and K. R. Wilson, Opt. Lett. **19**, 2000 (1994).

[17] V. Petrov, F. Rotermund, and F. Noack, J. Opt. A **3**, R1 (2001).